Pseudocapacitance: From Fundamental Understanding to High Power Energy Storage Materials

Simon Fleischmann,[1] James B. Mitchell,[1] Ruocun Wang,[1]
Cheng Zhan,[2] De-en Jiang,[3] Volker Presser,[4,5] & Veronica Augustyn[1,*]

[1] Department of Materials Science & Engineering, North Carolina State University, Raleigh, North Carolina, 27606, United States of America

[2] Quantum Simulation Group, Lawrence Livermore National Laboratory, Livermore, California, 94550, United States of America

[3] Department of Chemistry, University of California, Riverside, California, 92521, United States of America

[4] INM - Leibniz Institute for New Materials, Campus D2 2, 66123 Saarbrücken, Germany

[5] Saarland University, Campus D2 2, 66123 Saarbrücken, Germany

* Corresponding author's email: vaugust@ncsu.edu

Abstract

There is an urgent global need for electrochemical energy storage that includes materials that can provide simultaneous high power and high energy density. One strategy to achieve this goal is with pseudocapacitive materials that take advantage of reversible surface or near-surface Faradaic reactions to store charge, surpassing the capacity limitations of electrical double-layer capacitors and mass transfer limitations of batteries. The past decade has seen tremendous growth in the understanding of pseudocapacitance as well as materials that exhibit this phenomenon. The purpose of this Review is to examine the fundamental development of the concept of pseudocapacitance and how it came to prominence in electrochemical energy storage as well as to describe new classes of materials whose electrochemical energy storage behavior can be described as pseudocapacitive.

Table of Contents

1. Introduction

The need to power a growing variety of portable electronics and electric vehicles is increasing demand for energy distribution and storage in our daily lives. At the same time, the large-scale implementation of intermittent, renewable energy conversion devices like wind turbines and photovoltaics requires energy storage technologies to balance temporal fluctuations that range from seconds to hours. Of the many ways by which to store energy, electrochemical energy storage (EES) has been highly successful due to the high theoretical efficiency of converting chemical to electrical energy and the high energy densities and power densities afforded by solid-state electrodes. However, further technological innovation requires improvements to all relevant performance metrics and drives the global search for new materials and mechanisms. For example, the 2017 U.S. Department of Energy's Basic Research Needs report prioritizes, among several other directions, the need to attain simultaneous high power and high energy. This has been called the holy grail for EES.[1] Similar priorities have been outlined in the European Union Strategic Energy Technology Plan[2] and by China's Ministry of Science and Technology.[3]

There are several processes by which EES occurs at solid-state electrodes: (i) via the formation of an electrical double-layer (EDL), (ii) via surface redox reactions, (iii) via insertion of ions as in electrochemical intercalation, and (iv) via alloying, decomposition, or conversion reactions. The latter three processes are Faradaic in origin, that is, they obey Faraday's law and involve charge transfer reactions across the electrochemical interface.[4] Of these, surface redox and some ion-insertion reactions have been termed pseudocapacitive because their thermodynamic and kinetic behavior can be described with the same mathematical models as those for surface adsorption/desorption.

The focus of this review is on this electrochemical mechanism of pseudocapacitance: its historical development since the early 1960s, initial theory from both kinetic and thermodynamic arguments, and the current focus of gaining an atomistic understanding to guide the development of entirely new materials. The prefix pseudo originates from the Greek "ψευδής/pseudes" and translates to "false" or "lying." Therefore, pseudo-capacitive describes an electrochemical mechanism that appears to be capacitive, but in fact originates from charge transfer processes across the electrode/electrolyte interface. The past decade has brought tremendous interest into this mechanism due to the significant increase in synthesis routes that yield nanostructured or highly disordered redox-active materials, many of which can exhibit a pseudocapacitive response, as well as the potential technological importance of pseudocapacitance in achieving the possibility of energy storage with simultaneous high power and high energy density. This review will give special attention to mechanistic studies of pseudocapacitive behavior.

To date, the predominant EES technology for high-end mobile applications is the lithium-ion battery (LIB).[5,6] It was conceptualized in the 1970s[5] and 1980s[6] and commercially introduced by the Sony Corporation in 1991. Three of its inventors (Goodenough, Whittingham, and Yoshino) were honored with the 2019 Nobel Prize in Chemistry. In a LIB cell,[7,8] energy storage is accomplished by electrochemical intercalation reactions occurring at host anode and cathode electrodes composed of, typically, crystalline and micron-sized particles of the electrochemically active materials. The achievable charge/discharge rates in conventional LIBs consisting of graphite anodes and lithium metal oxide-based cathodes are limited by the diffusion of lithium ions within the host lattices and/or phase transformations.[9] This leads to the relatively low specific power of LIBs (around 500-2000 W/kg)[10,11] and prohibits a complete uptake or release of their charge in a

timeframe below tens of minutes, which would be desirable for many applications. The volume changes associated with electrode phase transformations during ion insertion further induce stresses to the crystalline lattices and limit the cycle life of batteries.[12]

The technological motivation for the search for pseudocapacitive electrode materials is to overcome the kinetic limitations plaguing LIBs while achieving higher energy density than electrical double-layer capacitors (EDLCs). Pseudocapacitance is not limited to a particular type of anion or cation, and is thus perfectly aligned with the search for beyond Li^+ materials and mechanisms for energy storage. The concept of pseudocapacitance emerged in the early 1960s to describe surface Faradaic processes such as underpotential deposition and hydrogen adsorption. It was extended to energy storage in the early 1970s with the observation that thin films of hydrous RuO_2 cycled in an acidic electrolyte exhibited cyclic voltammograms that resembled those of capacitors, while single-crystal RuO_2 did not.[13] Subsequent work, especially by Conway,[14] attempted to connect the observed capacitive electrochemical response with the electrochemical mechanism. Materials whose energy storage processes can be described by pseudocapacitance (termed pseudocapacitive materials here) undergo reversible electrochemical reactions within significantly shorter timeframes, even comparable to electrical double-layer capacitors in some cases,[15] while still exhibiting a high charge storage capacity comparable to that displayed by batteries. The exact atomistic mechanism is often unknown but is typically ascribed to highly reversible surface or intercalation charge transfer reactions that are not limited by solid-state diffusion (**Fig. 1**). In these cases, as will be described subsequently, the electrochemical behavior can be considered pseudocapacitive.

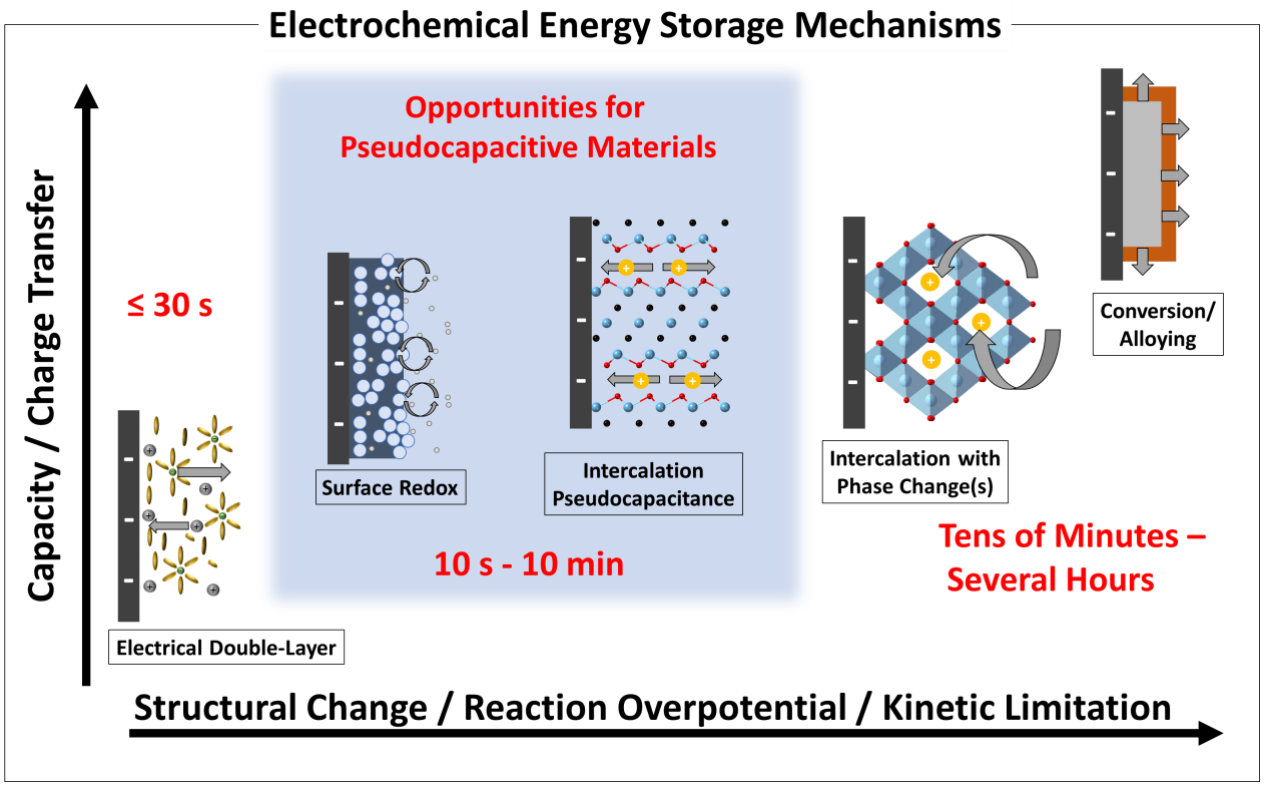

Figure 1: Classification of electrochemical energy storage mechanisms as a function of their characteristic capacity and the associated degree of structural changes of the electrodes, reaction overpotential, and kinetic limitations. We identify the main opportunities for pseudocapacitive materials for short cycling times of about 10 s to 10 min while exhibiting capacities associated with intercalation mechanisms.

Materials that exhibit pseudocapacitive behavior bridge the gap between materials used in EDLCs and those used in batteries (**Fig. 2**). Increasingly, the distinction between these three types of materials is blurred, particularly with the use of nanostructured materials whose particle sizes are much smaller than the diffusion length, or carbons with redox-active functional groups. **In general, a material that exhibits pseudocapacitive electrochemical features is one that is not limited by solid-state diffusion at timescales of minutes and whose electrochemical response is highly reversible, leading to high efficiency at high current densities**. Further development of pseudocapacitive materials requires an atomistic understanding of the thermodynamic and kinetic mechanisms responsible for the specific electrochemical behavior.

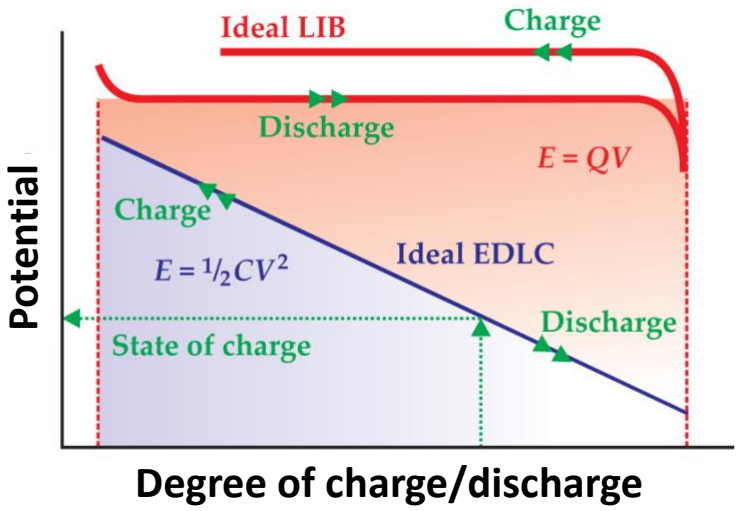

Figure 2: Characteristic electrochemical signature of the potential-charge curve for capacitor-like processes (ideal EDLC) and battery-like processes (ideal LIB). The potential hysteresis between the charge and discharge potential plateaus of battery-like processes upon application of a sufficient current density is called the overpotential and results in significantly reduced energy efficiency at short timescales of minutes to seconds. Adapted from Ref. [16], with the permission of the American Institute of Physics.

The past decade has seen a dramatic increase in synthetic capability to yield nanostructured, highly defective, and metastable materials, and we will describe how these structural features give rise to pseudocapacitive behavior. We will also discuss new structural features that lead to a pseudocapacitive response in materials, such as the presence of confined interlayer fluids in two-dimensional materials. The purpose of this review is to provide a comprehensive report and analysis of the historical development, proposed mechanisms, and discovery of new pseudocapacitive materials from the past decade. A particular focus will be to discuss those studies that probe the electrochemical behavior with in situ or operando methods to develop a fundamental understanding of the mechanisms. We will also discuss recent efforts to develop fundamental theories of pseudocapacitance, particularly ab initio efforts.

2. Historical Development of Pseudocapacitance

The word pseudocapacitance originates from pseudo-capacity, a term used by David C. Grahame in 1941 to describe excess capacity that was not associated with the formation of the electrical double-layer.[17] Pseudocapacitance was then used in the work of Conway and Gileadi in the early 1960s to understand electrochemical charge transfer reactions associated with surface adsorption.[18,19] Pseudocapacitance was initially defined in terms of the fractional surface coverage (θ) of adsorbed species following the Langmuir adsorption model.[19] Since the capacitance arose from Faradaic reactions that involved monolayers of electrochemically active species, it was distinguished from both double-layer capacitance, which was strictly electrostatic, as well as the typical behavior of battery materials, which (at that time, before the emergence of lithium-ion chemistries) involved significant phase and structural transformations of the

reactants. Theoretically, Langmuir-type adsorption would lead to a charge transfer peak that corresponds to a capacitance maximum when θ = 0.5 over a narrow potential range. Peak broadening was attributed to increased lateral interaction between the surface adsorbates, modeled as a lateral interaction energy.

The theoretical framework for pseudocapacitance proposed by Conway and Gileadi occurred around the same time that experimental observations revealed the signatures of rapid electrochemical charge transfer processes of surface-bound species, such as in underpotential deposition (UPD), adsorbed intermediates to electrolysis, and modified (thin-film) electrodes.[20] UPD is the electrodeposition of metal monolayers onto a different metal substrate at potentials that are less negative than for the electrodeposition of the same metal as the substrate.[21] In this process, there is partial charge transfer between the electrodeposited metal monolayers and the underlying metal substrate. The cyclic voltammograms exhibit pronounced and highly reversible peaks associated with the formation of different structures of the electrodeposited monolayers. Up to intermediate cycling rates (ca. 5 mV/s), this process tends to exhibit a linear dependence of the peak current with the sweep rate. These fundamental studies led to the development of the concept of pseudocapacitance, but it was not until the discovery of highly reversible charge transfer reactions in thin films of metal oxides that the mechanism was considered of use for EES. This is because, in the above-described cases, charge transfer linked to UPD occurs within a limited potential range and exhibits low overall charge.[14] In this review, we report mostly capacity (unit: mAh) values instead of capacitance (unit: F) of materials because numerous pseudocapacitive materials do not exhibit an ideally constant capacitance over the selected

potential range, and capacity provides a more compatible metric to compare with other materials.[22]

The discovery of pseudocapacitance in transition metal oxides dates back to 1971 when the charge storage behavior of a ruthenium oxide thin film in sulfuric acid was first reported by Trasatti and co-workers.[13] Unlike a single crystal RuO_2 electrode, the thin film electrode exhibited a highly symmetric and reversible cyclic voltammogram, which was later attributed to reversible redox reactions at the surface of the RuO_2 electrode.[23] Subsequent studies found that hydrated or nanostructured forms of RuO_2 exhibit significantly higher specific capacitance.[24] It was hypothesized that the structural water in hydrated RuO_2 ($RuO_2 \cdot 0.5H_2O$) facilitates proton transport. Nanostructuring increased the interfacial area between RuO_2 and the electrolyte and made more reactive sites accessible for charge transfer reactions.[23,25] The specific capacitance can reach about 720 F/g in a voltage window of 1 V (equivalent to a specific capacity of 200 mAh/g) at a scan rate of 2 mV/s (t = ~8 min),[24] much higher than what has been attained with carbon materials that exhibit only EDL capacitance. This electrode was kinetically limited by the increase in ionic resistance of the electrolyte due to ion starvation in the porous electrode in the fully charged state. However, the authors noted that the reaction rate could be improved to decrease the charging/discharging times to about 10 s by absorbing a higher volume of electrolyte into the porous electrode.[24] The attractive performance relied on the metallic conductivity and high charge transfer activity of hydrated RuO_2 in acidic electrolytes. However, the high cost of ruthenium (about 8000 USD/kg in 2020) prohibits widespread commercialization of RuO_2 as an electrode material in electrochemical energy storage devices.

The high capacitance, wide voltage range, and fast kinetics of hydrous RuO_2 sparked interest in the search for low-cost and abundant metal oxides that could exhibit similar pseudocapacitive behavior. In 1999, the Goodenough group reported that an amorphous, hydrated $MnO_2{\cdot}xH_2O$ showed capacitor-like behavior in pH-neutral aqueous electrolytes.[26] The material was prepared by dissolution of potassium permanganate and manganese acetate in water, yielding manganese oxide as a brown precipitate. The specific capacitance reached about 200 F/g in a potential window of 1.2 V in aqueous KCl electrolyte (ca. 67 mAh/g), and reportedly originated from surface redox reactions of MnO_2 with potassium cations. Despite the poor electrical conductivity of MnO_2, the material showed promise due to its economic and ecological viability and is to date one of the most studied pseudocapacitive materials.

The pseudocapacitive charge storage properties of conducting polymers, a class of materials established by Shirakawa et al.,[27] were studied since the late 1980s.[28–31] Conductive polymers store charge via the mechanism of reversible electrochemical doping, which is characterized by a somewhat rectangular cyclic voltammogram that may exhibit a set of highly reversible redox peaks. This process involves either the oxidation of the conductive polymer backbone with the concurrent insertion of an anion from the electrolyte (*p*-doping) or the reduction of the conductive polymer with concurrent cation insertion (*n*-doping), yielding delocalized charge carriers along the polymer chains.[32] Many conductive polymers exhibit alternating single- and double-bonds between the carbon atoms in the polymer chain, and the most commonly used conductive polymers are polyaniline (PANI), polypyrrole (PPY), and derivatives of polythiophenes like poly(3,4-ethylenedioxythiophene) (PEDOT).[30,33] Theoretical capacities of conductive polymers are mainly governed by their reversibly accessible doping level (γ), that is, the number

of dopants per monomer unit. γ is typically 0.3-0.5, determined by the closest proximity of charge carriers that can be accommodated along the polymer chain.[30] This leads to theoretical capacities of 146 mAh/g for PANI (γ = 0.5), 132 mAh/g for PPY (γ = 0.33), and 62 mAh/g for PEDOT (γ = 0.33). The power of conductive polymer electrodes is mainly limited by the diffusion of counter-ions to the doping sites in the bulk polymer.[30] Carbonaceous supports are often used to increase the accessibility of the bulk polymer to the electrolyte, improve the charge transfer rate at low doping levels, and limit volumetric changes during cycling, all of which can lead to better electrochemical rate handling and cycling stability.[34–38] The mechanical flexibility of conducting polymers makes them of interest as electrodes for wearable energy storage.[29,39] However, further research is necessary to improve their relatively poor cycling stability, high dependence on carbonaceous supports for electrical conductivity, and low volumetric capacities.

The 1980s saw the emergence of pseudocapacitive charge storage in Li^+ intercalation materials using organic electrolytes. The characterization of such processes in terms of pseudocapacitance was proposed by Conway in the early 1990s who considered Li^+ intercalation as a 2D ion sorption process in between layers of transition metal oxides and sulfides.[40,41] A similar treatment was proposed by Levi and Aurbach, who modeled Li^+ intercalation in terms of a Frumkin intercalation isotherm.[42] In certain transition metal oxide materials, there are crystallographic directions along which Li^+ can diffuse very rapidly, leading to no solid-state diffusion limitations over a wide range of timescales and no first-order phase transformations. Zukalová et al. reported that Li^+ storage in the monoclinic bronze-structure of titanium oxide TiO_2(B) is not limited by solid-state diffusion at rates up to 2 mV/s (t = ~10 min), and labeled the charge storage mechanism as pseudocapacitive.[43] The authors speculated that the rate-limiting

step was either Li^+ transport through the electrode/electrolyte interface or trapping of Li^+ in the channels. Similarly, Augustyn et al. found that Li^+ intercalation in T-Nb_2O_5 exhibits capacitor-like kinetics with charging times as low as 1 min.[44] This was attributed to rapid transport along two-dimensional planes and no intercalation-induced phase changes over a wide extent of Li^+ storage. The discovery of two-dimensional transition metal carbides, nitrides, and carbonitrides (MXenes)[45] added a new class of materials to the family of pseudocapacitive materials, with $Ti_3C_2T_x$ MXene showing pseudocapacitive H^+ intercalation in acidic electrolytes at rates up to 10 V/s (t = ~0.1 sec),[15] rivaling the kinetics of EDLCs. These results ushered in a new era for intercalation pseudocapacitance materials, where the strategy shifted from increasing the material surface area to designing structural features that led to rapid ion transport in the bulk of a material, such as the presence of interlayer-confined fluids.

Figure 3: Timeline of major developments in the field of pseudocapacitance: New pseudocapacitive materials, mechanisms, and theoretical concepts.

The past decade has also seen the tremendous rise of nanostructured and defect-rich materials for EES, many of which exhibit pseudocapacitive features. When the pseudocapacitive behavior emerges due to nanostructuring, this has been termed *extrinsic pseudocapacitance*[46] and is in contrast to those materials that appear to exhibit capacitive behavior over a wide range of particle size and dimensions (called *intrinsic pseudocapacitance*). Nanostructuring increases the specific surface area and, in turn, the interfacial contact area between electrode and electrolyte. A significant portion of the reactive sites is near the fluid/solid interface, which drastically reduces the solid-state diffusion distances for ions from the electrolyte and can lead to dispersion in the redox site energy.[25] Nanostructured materials also increase the effects of surface defects such as anion or cation vacancies that can have a critical influence on the electrochemical energy storage mechanism.[47–49]

In concert with these materials developments, there have been significant efforts to understand the fundamental physicochemical mechanisms that give rise to pseudocapacitance. A timeline of major developments in the field of pseudocapacitance is given in **Fig. 3**. The new materials and fundamental understanding of pseudocapacitance have led to the development of a variety of energy storage devices, most prominently hybrid electrochemical capacitors, which have been the topics of recent reviews.[50,51] Taken together, these developments have enabled significant strides for the development of EES with simultaneous high power, energy density, and reliability.

3. Fundamental Understanding

3.1 Definition and Types of Pseudocapacitance

The concept of pseudocapacitance was first used by Conway and Gileadi in 1962 to describe the capacitance associated with the electrochemical adsorption of species on electrode surfaces (e.g., O or OH on nickel oxide and H on Pt).[19] The proposed kinetic theory assumed a linear dependence of the heat of adsorption on the surface coverage of the electrodeposited species and led to a capacitance defined in terms of the surface coverage. Conway later extended the concept of pseudocapacitance to monolayer adsorption (adsorption pseudocapacitance, **Fig. 4A,D**),[52] Faradaic reactions of hydrous RuO_2 in H_2SO_4 (redox pseudocapacitance, **Fig. 4B,E**),[53,54] and solid-solution electrochemical intercalation (intercalation pseudocapacitance, **Fig. 4C,F**).[41] In each of these, the extent of reaction (based on the surface coverage, surface redox, or intercalation; ξ) depends linearly or almost linearly on the potential (V), leading to the thermodynamic definition of pseudocapacitance as simply $\Delta\xi/\Delta V$. It should be noted that for the hydrous RuO_2 in Fig. 4E, and certain other materials, the electrochemical response lacks obvious features of surface Faradaic reactions. The nature of capacitive storage in such materials has long been a topic of discussion, as will be noted below.

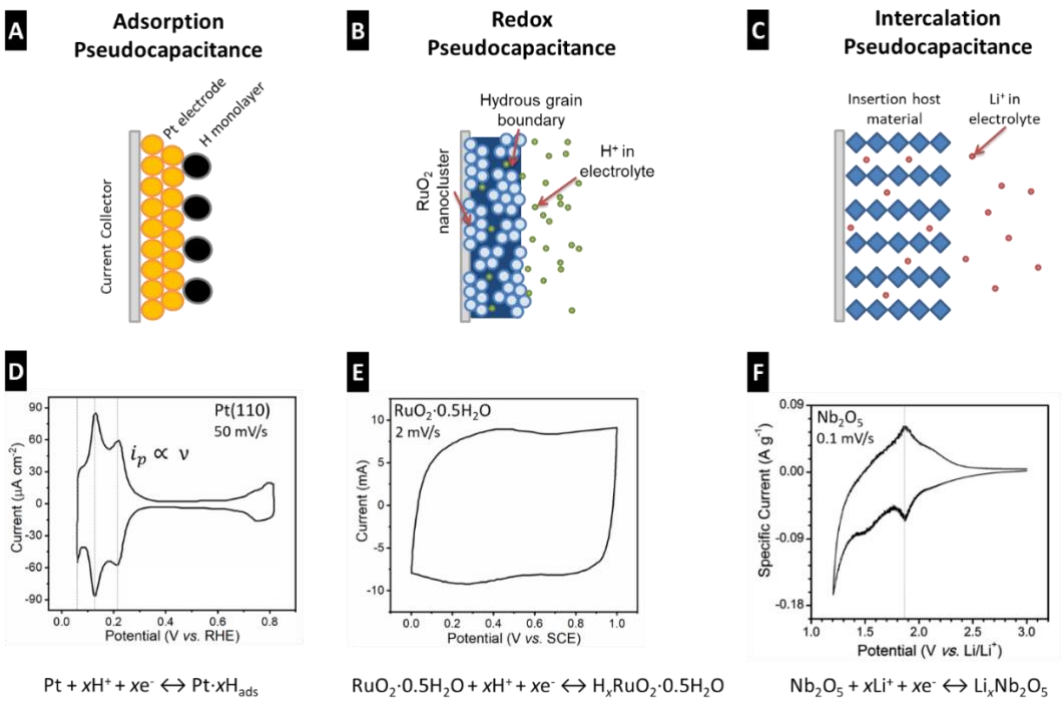

Figure 4: (A-C) Illustration of the three types of mechanisms that give rise to pseudocapacitance as defined by Conway and (D-F) their corresponding cyclic voltammograms. (A) Adsorption pseudocapacitance, (B) redox pseudocapacitance, and (C) intercalation pseudocapacitance. Adapted from Ref. [25] with permission from The Royal Society of Chemistry. (D) Cyclic voltammogram of a Pt (110) surface in aqueous 0.1 M $HClO_4$ solution cycled at 50 mV/s. RHE stands for the reversible hydrogen electrode, i_p for peak current, and v for sweep rate. The dotted lines indicate the high reversibility of the Faradaic adsorption processes. Adapted from Ref. [55]. Copyright 2004 American Chemical Society. (E) Cyclic voltammogram of a $RuO_2 \cdot 0.5H_2O$ electrode in aqueous 0.5 M H_2SO_4 solution cycled at 2 mV/s. SCE stands for the standard calomel electrode. Adapted with permission from Ref. [24]. Copyright 1995 IOP Publishing. (F) Cyclic voltammogram of T-Nb_2O_5 nanocrystalline film in a non-aqueous Li^+ electrolyte cycled at 0.1 mV/s. The dashed line indicates the high reversibility of the Faradaic intercalation process. Adapted from Ref. [25] with permission from The Royal Society of Chemistry.

It is useful to revisit the theory developed by Conway for the first type of pseudocapacitance ("adsorption pseudocapacitance"), illustrated here for the electrosorption of cation A^+ onto the surface of a conductive substrate M:[52]

$$A^+ + M + \mathrm{e}^- \leftrightarrow MA_{\mathrm{ads}} \quad (1)$$

It is assumed that the adsorbing species follow a Langmuir-type electrosorption isotherm:

$$\frac{\theta}{1-\theta} = KC_A e^{\frac{VF}{RT}} \quad (2)$$

where the concentration of the cation in solution is C_A, the surface coverage of MA_{ads} is θ, the surface coverage of M is 1-θ, the ratio of the forward and reverse reaction rate constant is K, F is the Faraday constant, R is the ideal gas constant, V is the electrode potential, and T is the temperature. Rearrangement of **Equation 2** leads to the following, which has the form of the Nernst equation except now the ratio of the reduced to oxidized species has been replaced by the extent of adsorbate surface coverage, θ:

$$E = E^0 + \frac{RT}{F} ln\left[\frac{1}{KC_A}\frac{\theta}{1-\theta}\right] \quad (3)$$

where, E is the equilibrium potential of the redox couple and E^0 is the standard potential of the redox couple. Assuming the charge required to complete a monolayer coverage of A_{ads} is q, the pseudocapacitance C_Φ can be defined as:[52]

$$C_\Phi = q\frac{d\theta}{dV} = \frac{qF}{RT} \cdot \frac{KC_A e^{\frac{VF}{RT}}}{\left(1+KC_A e^{\frac{VF}{RT}}\right)^2} = \frac{qF}{RT}\theta(1-\theta) \quad (4)$$

Equation 4 indicates that the maximum pseudocapacitance is reached when θ = 0.5. As a result, for a purely Langmuir-type electrosorption process, the pseudocapacitance will be a function of the applied potential and surface coverage, as shown in the solid curves of **Fig. 5A**. Two factors can substantially reduce the steepness of the isotherm, leading to a broadly distributed

dependence of C_Φ on potential: (i) deposition of adsorbates at distinguishable successive states of electrochemical adsorption with increasing coverage, giving rise to multiple peaks as illustrated in **Fig. 5B**;[56,57] and/or (ii) a lateral repulsive interaction between adsorbates as θ increases, increasing the dependence of C_Φ on potential. The latter can be described by introducing a lateral interaction parameter (g) as a function of θ (Frumkin-type isotherm):

$$\frac{\theta}{1-\theta} = KC_A e^{(\frac{VF}{RT} - g\theta)} \quad (5)$$

$$C_\Phi = \frac{qF}{RT}\frac{\theta(1-\theta)}{1+g\theta(1-\theta)} \quad (6)$$

The lateral interaction parameter g represents either attractive ($g > 0$) or repulsive ($g < 0$) interactions between the adsorbed species.[58] When g is > 0 (the dashed curves in **Fig. 5A**), the resultant pseudocapacitance has a broader peak shape and a lower maximum as compared to the Langmuir case.

It should be highlighted again that the formalism developed by Conway leads to a potential-dependent pseudocapacitance, even when accounting for the presence of successive Faradaic reactions and the interactions between species. However, the electrochemical response of certain pseudocapacitive materials lacks obvious Faradaic peaks. To explain this, Costentin and Savéant[59] proposed the combination of double-layer and Faradaic processes (**Fig. 5C**). In this case, the double-layer charging current is equal to, or greater than, the faradaic current contribution. In order to account for such a large double-layer capacitance, the electrochemically active surface area of the material must be much larger than what is typically measured using electrochemical or physical adsorption methods. The interplay between Faradaic and double-layer processes in pseudocapacitive materials, particularly those that confine fluids such as hydrous ruthenium oxide, deserves further attention.

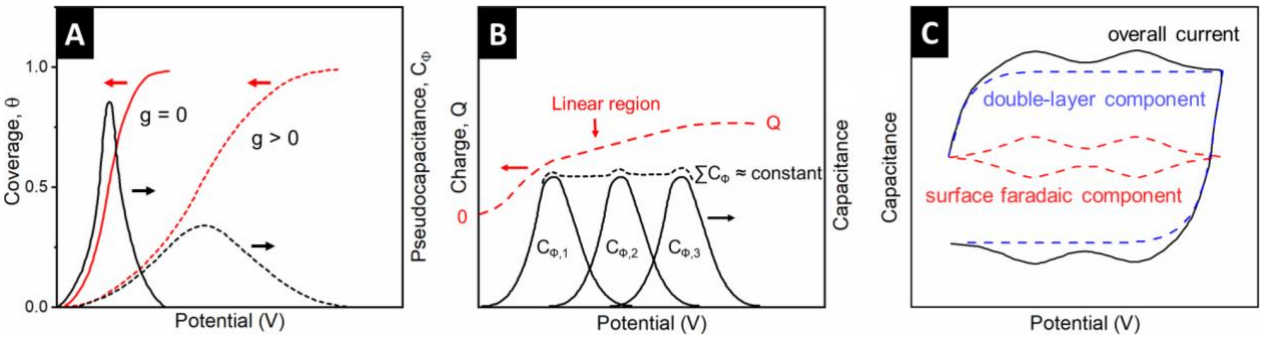

Figure 5: (A) The variation of pseudocapacitance, C_Φ, and surface coverage, θ, for ideal Langmuir electrosorption (g = 0, solid curves) and Frumkin-type electrosorption that involves lateral interactions between surface adsorbates (g > 0, dashed curves). The outcome of this is that pseudocapacitance, as originally defined, is strongly potential dependent. The addition of the lateral interaction parameter broadens the peak but does not eliminate the potential dependence. Adapted with permission from Ref. [40]. Copyright 1991 IOP Publishing. (B) Illustration of how three redox processes ($C_{\Phi,1}$, $C_{\Phi,2}$, and $C_{\Phi,3}$) could overlap to form an almost-constant overall capacitance over an appreciable potential range in electrochemically formed RuO_2 thin films. Q (dashed curve) is the charge accumulated over the potential range and $\sum C_\Phi$ (short dashed curve) are the summed capacitance of the three redox processes. Adapted with permission from Ref. [57]. Copyright 1999, Springer Science Business Media New York. (C) Calculated CV of the linear combination of double layer charging and surface faradaic reactions that could give rise to an almost-constant overall capacitance. Adapted from Ref. [59]. Copyright 2017 American Chemical Society.

Conway generalized his approach to two other redox mechanisms by replacing the surface coverage, θ , with the lattice occupancy, *X*, for intercalation pseudocapacitance, and concentration of the oxidant, [Ox]/[Red], for surface redox pseudocapacitance.[14] This thermodynamic approach to pseudocapacitance only focuses on its relationship to the applied potential. However, as argued by Conway in his seminal 1991 paper in the *Journal of the Electrochemical Society*,[40] the critical feature of pseudocapacitive redox processes as compared to batteries (in this argument, battery processes were those charge storage processes that involve significant phase transformations like conversion and alloying) was that pseudocapacitive processes were highly electrochemically reversible over an extended time domain. In this way, Conway established that pseudocapacitive mechanisms exhibit kinetic electrochemical signatures indicative of high reversibility, which include a mirror image cyclic voltammogram (**Fig. 6A**) and little-to-no hysteresis during galvanostatic cycling (**Fig. 6B**). Such behavior is desirable for technological applications because it will result in efficient energy storage at high power densities.[60]

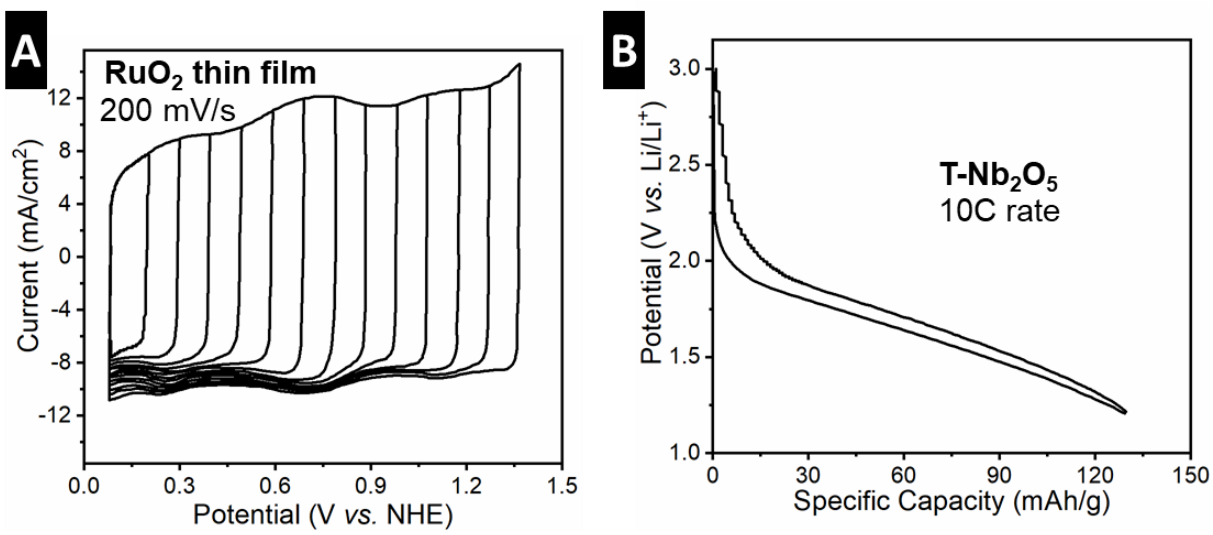

Figure 6: Examples of high electrochemical reversibility in materials that exhibit pseudocapacitive charge storage: (A) "Mirror image" cyclic voltammograms of a RuO_2 thin film electrode cycled in an acidic electrolyte at 200 mV/s and with various potential windows. Adapted with permission from Ref. [53]. Copyright 1978 IOP Publishing. (B) Reversible and almost linear galvanostatic charge-discharge curve of orthorhombic *T*-Nb_2O_5 at a 10C rate in a non-aqueous Li^+ electrolyte. Adapted with permission from Ref. [44]. Copyright 2013 Springer Nature.

3.2 Current Interpretations of Pseudocapacitance

The kinetic and thermodynamic description for pseudocapacitance developed by Conway occurred approximately a decade before the discovery of the highly capacitor-like electrochemical response of hydrous RuO_2 thin films by Trasatti and Buzzanca in 1971. Since then, there has been significant growth in the number of materials exhibiting pseudocapacitive behavior. As a result, it is natural for the understanding of pseudocapacitance to evolve, particularly since Conway's formalism was not based on an atomistic description and thus could not anticipate the variety of materials and processes. For example, Brousse, Bélanger, and Long

proposed a stricter definition of pseudocapacitance as applying only to those materials whose capacitance was nearly constant over a broad potential range.[22] One purpose of this definition was to discourage the growing trend of reporting very high gravimetric capacitance values for materials that did not exhibit the electrochemical features indicative of pseudocapacitive materials, such as the redox of $Ni(OH)_2$ in alkaline electrolytes. Also, to account for the growing number of reports of nanostructured materials exhibiting the electrochemical features of pseudocapacitance defined by Conway, Simon, and others proposed the concept of extrinsic pseudocapacitance as presented in **Fig. 7**. The argument for this nomenclature was that in nanostructured materials that undergo, for example, intercalation reactions which do not require a significant mass transfer, the diffusion length, *l*, is much smaller than the square root of the product of diffusion time (t_d) and diffusion coefficient (D):

$$l \ll \sqrt{D t_d} \tag{7}$$

Also important is that in nanostructured materials, a large fraction of the redox sites lie at the interface between the electrode and electrolyte. Near the interface, the geometry of these sites is expected to be more dispersed than in the bulk. This leads to an increasingly capacitor-like electrochemical response.[61,62]

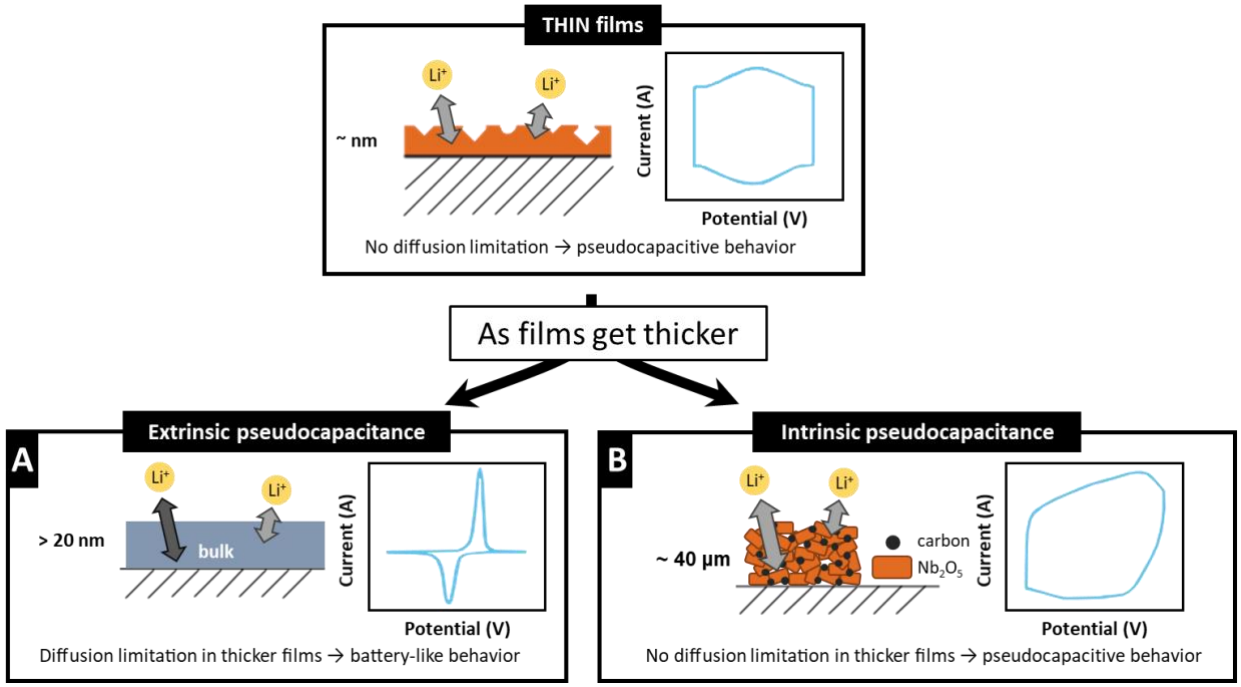

Figure 7: Schematic representation and corresponding cyclic voltammograms of extrinsic and intrinsic pseudocapacitive materials. Electrochemical responses that appear to be pseudocapacitive in a thin film or with nanostructuring but become diffusion-controlled in bulk particle electrodes are classified as (A) extrinsic pseudocapacitance. On the other hand, (B) intrinsic pseudocapacitance shows no diffusion limitation in both thin-film and bulk particle electrodes due to fast ion diffusion. Adapted with permission from Ref. [46]. Copyright 2014 IOP Publishing.

Costentin and Savéant used an electrochemical approach to understand the atomistic origin for the nearly rectangular cyclic voltammogram behavior of certain pseudocapacitive materials such as MnO_2 and hydrous RuO_2.[59,63] As noted above, they argue that such an electrochemical response could not arise from a series of overlapping redox reactions proposed by Conway and others (**Fig. 5B**). Instead, it is proposed that in such materials, the electrochemical response is due

to EDL formation at metallically conductive electrodes, or that it is a combination of surface Faradaic and EDL processes (Fig. 5C). In the case of MnO_2 and hydrous RuO_2, a large number of in situ and operando studies show structural and chemical changes occurring in the materials during electrochemical cycling.[64–66] This behavior cannot be explained entirely by EDL formation and is more in-line with the concept that both double layer and Faradaic processes contribute to the overall pseudocapacitance of the materials.

The formalism developed by Conway and used prominently in electrochemistry has similarities, and in some cases, is the same, as concepts and nomenclature developed in related research areas. For example, "intercalation capacitance"[42,67] is analogous to "intercalation pseudocapacitance." It is possible that both of these terms came into use in the scientific literature because ion intercalation materials for EES were discovered nearly a decade after the development of the pseudocapacitance concept by Conway.[5] The distinction between pseudocapacitive and "battery-type" processes becomes blurred when discussing intercalation-type EES, particularly for nanostructured materials and those that exhibit solid-solution intercalation (i.e., intercalation that does not cause a phase transition of the host). This is because intercalation continues to be a unique mechanism where the host lattice undergoes very minimal structural transformations (as compared to other common rechargeable battery chemistries that utilize electrode conversion or alloying). Levi and Aurbach recognized the mechanistic similarity between surface adsorption and ion intercalation (or "sorption") into a host material. They utilized the Frumkin adsorption isotherm to model Li^+ intercalation into a host material,[42] essentially analogous to Conway's definition of pseudocapacitance applied to intercalation.[41] The concept of shallow vs. deep "adsorption" sites was later used to explain the capacitive response

of certain ion inserting materials.[68] Shallow sites were those that could be easily accessed by electrolyte cations, and resided near the surface, whereas deep adsorption sites were those that had higher activation barriers in the interior of materials. Several recent studies have also challenged the distinctions between double-layer capacitance and pseudocapacitance.[63,69,70] For example, in one density functional theory (DFT) study, the difference between double-layer capacitance and pseudocapacitance was whether the cation was inserting with or without a hydration shell into an already-hydrated interlayer.[71] The need to understand pseudocapacitance from a mechanistic standpoint, and the interplay between faradaic and non-faradaic processes, is indeed at the frontiers of understanding the nature of electrochemical charge transfer at surfaces.

3.3 Electrochemical Features of Pseudocapacitance

Electrochemical characterization continues to be a critical tool even as fundamental understanding of pseudocapacitance evolves. In today's context, the hallmarks of the electrochemical signature of pseudocapacitance are (i) a linear or pseudo-linear relationship between the applied potential and state of charge (which allows for the calculation of a capacitance, dQ/dV), (ii) nearly ideal electrochemical reversibility, and (iii) surface-controlled kinetics. Such electrochemical features are indicative of mechanisms that involve no significant structural transformations, for example, mass transfer of heavy atoms and/or phase transformations, including between two solid phases. Usually, the mechanisms that give rise to pseudocapacitive features are due to reversible charge transfer reactions occurring at or near the surface, as often observed in nanoscale materials. The electrochemical process should be associated with a charge transfer mechanism via a growing number of operando characterization

techniques. The electrochemical behavior should also be probed at timescales of < 10 min, the regime where pseudocapacitive materials exhibit higher capacities and efficiencies than typical battery materials.

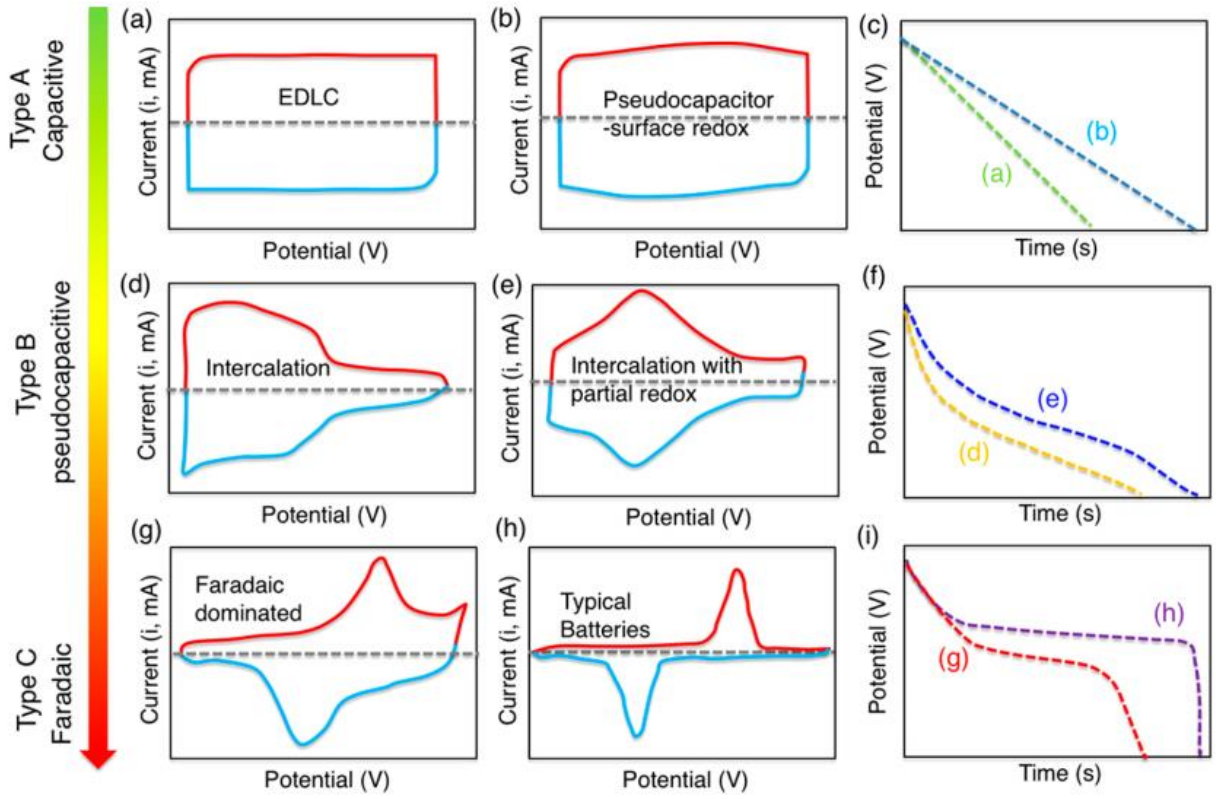

Figure 8: Examples of how electrochemical characterization can be utilized to identify charge storage mechanisms. Schematic cyclic voltammograms (A, B, D, E, G, H) and corresponding galvanostatic profiles (C, F, I) representing various types of charge storage. The pseudocapacitive types presented here include (B) surface redox pseudocapacitance (e.g., hydrated RuO_2 in acidic aqueous electrolytes), (D) intercalation pseudocapacitance (e.g., *T*-Nb_2O_5 in a Li^+ non-aqueous electrolyte), and (E) combination of intercalation and surface redox pseudocapacitance (e.g., $Ti_3C_2T_x$ MXene in an acidic aqueous electrolyte). Reprinted from Ref. [72]. Copyright 2018 American Chemical Society.

The electrochemical features of pseudocapacitive materials are usually examined by cyclic voltammetry, galvanostatic charge/discharge tests, or electrochemical impedance spectroscopy (EIS). Cyclic voltammograms and galvanostatic discharge curves of various representative materials are presented in **Fig. 8**. In this categorization, Type B pseudocapacitive is Faradaic in nature, while Type C Faradaic is not capacitive in nature. Cyclic voltammetry is a common characterization technique for the study of pseudocapacitive materials because of the ease in identifying the "mirror image" criterion and relationship between current and sweep rate. The pseudo-linearity and hysteresis of galvanostatic discharge curves can also be used to assess pseudocapacitance. EIS can be used to evaluate pseudocapacitive behavior by analyzing the real/imaginary impedance, real/imaginary capacitance, and phase angle. More detailed discussions of techniques based on cyclic voltammetry and EIS are presented next.

In a cyclic voltammogram, a pseudocapacitive material would be characterized by very broad/distributed charge transfer peaks that are mirror images of each other during the cathodic and anodic scans with a rapid turnover from the cathodic to anodic current. The mirror image criterion is particularly important and can be used to separate a pseudocapacitive material from nearly all battery-type materials. One way to quantify this is to track the peak potential as a function of sweep rate:[40] pseudocapacitive materials will have a region where there is almost no change of the peak position with a variation of the sweep rate. The energy storage efficiency of such materials will be high even at short charge/discharge times (less than a few minutes). It should be emphasized that Ohmic losses at high rates can lead to peak separation in pseudocapacitive materials.[40]

Lindström et al. proposed a simple relationship between the applied sweep rate and observed electrochemical current, and used it to study Li^+ insertion into nanoporous anatase TiO_2 films. This relationship can be used as a first-line tool (referred to as *b*-value analysis) to determine the presence of surface-controlled/capacitive (vs. semi-infinite diffusion-controlled) kinetics:

$$i(V) = a\nu^b \tag{8}$$

where *i*(*V*) is the current at a specific potential, *a* and *b* are adjustable parameters, and *b* can be determined as the slope of log(*i*) vs. log(*v*) for various sweep rates, *v*. Kinetic limitations can be estimated from the limiting cases of the *b*-value, *b* = 1 and 0.5. When the current is directly proportional to the sweep rate, *b* = 1, the process is surface-controlled. There are two possibilities for the mechanism behind such a response: the current is due to the formation of the electrical double-layer:

$$i = C_{DL}A\nu \tag{9}$$

where C_{DL} is the double-layer capacitance per surface area, and *A* is the electrochemically active surface area of the electrode. The other option is that the current is due to redox processes not limited by diffusion, what some electrochemical literature terms "modified [thin film] electrodes":[73]

$$i = \frac{nF^2}{4RT}A\Gamma^*\nu \tag{10}$$

where *n* is the number of transferred electrons, and Γ^* is the amount of redox-active adsorbed species at the surface (mol/cm^2). Whether the mechanism is ascribed to double-layer capacitance or redox processes not limited by diffusion, the relationship between current and sweep rate is the same, with *b* = 1. Therefore, to distinguish between those two processes, other techniques need to be utilized. One of the most common approaches has been to determine the

electrochemically active surface area and then calculate the double-layer capacitance assuming a constant value of 10-40 μF/cm^2.[74,75] While this approach may provide a good estimate, determining the electrochemical surface area is often challenging, and the double-layer capacitance of most materials is not clearly established.[76] This is particularly problematic for pseudocapacitive materials, such as hydrous RuO_2, that exhibit hydrated grain boundaries or interlayers. The electrochemically active surface area of such materials may be much larger than what is typically measured with, for example, physical adsorption of gas molecules. Therefore, distinguishing between Faradaic and non-Faradaic processes often requires the combination of electrochemical characterization with techniques that can detect a charge transfer event, such as changes in the optical and electronic properties or bond length, ideally in an operando setting.

When b = 0.5, the reaction is semi-infinite diffusion-controlled, and the current follows the Randles-Ševčík equation:

$$i = 0.4958n \cdot FAC^* \cdot D^{1/2} \left(\frac{\alpha nF}{RT}\right)^{\frac{1}{2}} \nu^{1/2} \quad (11)$$

where C^* is the maximum concentration of the reduced species in the structure, and α is the transfer coefficient. The Randles-Ševčík equation was developed to determine the diffusion coefficient of a redox-active species in the electrolyte and adapted for the case of redox-active electrodes for semi-infinite diffusion control, for example, when the diffusion distance is much larger than $\sqrt{Dt_d}$.

When the b-value falls between 0.5 and 1, the mechanism is attributed to either mixed control (a linear combination of diffusion and capacitive contributions)[77] or finite-length diffusion (where the diffusion distance is smaller than $\sqrt{Dt_d}$).[78,79] Under the mixed control assumption, Liu et al. proposed the following linear combination of surface- and diffusion-controlled currents:[77]

$$i(V,v) = k_1(V)v + k_2(V)v^{1/2} \quad (12)$$

Dunn et al. utilized this concept to deconvolute capacitive vs. diffusive contributions to the total current for many types of nanostructured transition metal oxides.[80–82] To do this, **Equation 12** is rearranged to obtain:

$$i(V,v)/v^{1/2} = k_1(V)v^{1/2} + k_2(V) \quad (13)$$

Solving for k_1 and k_2 at specific potentials across multiple sweep rates gives the quantitative fraction of the current due to surface- and diffusion-controlled processes. The method allows for the separation of the cyclic voltammograms into surface-controlled and diffusion-controlled regions, as shown in **Fig. 9A**. The charge stored due to surface- and diffusion-controlled current contributions can then be quantified at different sweep rates, such as in **Fig. 9B**. One major limitation of this approach is that it does not account for the shift of potential with higher sweep rates due to increased Ohmic losses.[83,84] While **Equation 12** is simplistic, it has provided a critical and quantifiable understanding of how nanoscale materials develop pseudocapacitive features.

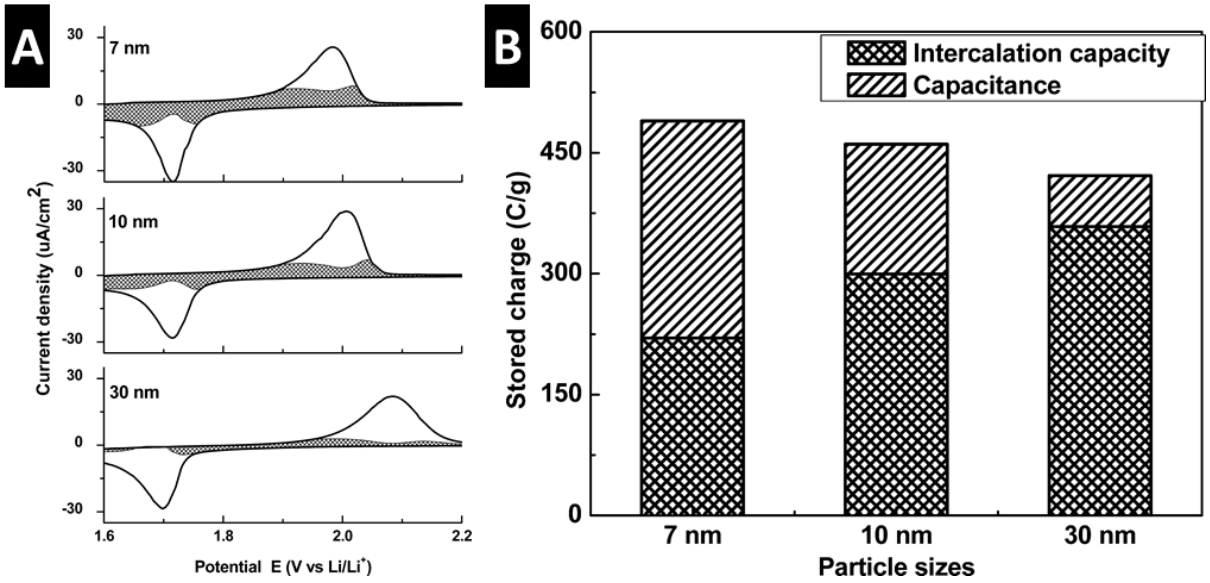

Figure 9: (A) Cyclic voltammograms of nanostructured anatase TiO_2 films at 0.5 mV/s in a non-aqueous Li^+ electrolyte. The surface-controlled currents (shaded regions) are determined with the k_1, k_2 analysis using Equation 12. (B) Charge storage of the same three TiO_2 thin films at 0.5 mV/s contributed from surface-controlled ("capacitance") and diffusion-controlled current ("intercalation capacity"). Adapted from Ref. [85]. Copyright 2007 American Chemical Society.

The k_1, k_2 analyses described above do not account for redox peak potential shifts due to polarization processes, which become significant at fast sweep rates (typically, > 10 mV/s). To mitigate the impact of the Ohmic drop, multiple-step chronoamperometry (MUSCA) was developed by Shao et al. based on the potentiostatic intermittent titration technique (PITT).[83] In cyclic voltammetry, a short residence time is held at each potential, and the recorded current is averaged over a portion of the step duration. In PITT, each potential step is held until equilibrium, and the current is recorded at short time steps resembling chronoamperometry. A typical potential waveform and its current response are shown in **Fig. 10A**. PITT minimizes Ohmic contributions as the steady-state current is reached at each step. Dupont and Donne found that

by averaging current over a selected period of time for each potential step, current vs. potential profiles can be reconstructed at various sweep rates.[86] As an example, the voltammograms reconstructed by MUSCA for $Ti_3C_2T_x$ MXene in aqueous 3 M H_2SO_4 showed less significant peak shifts as compared to those obtained from cyclic voltammetry (**Fig. 10B-C**). Using the reconstructed voltammograms, the k_1, k_2 analysis can be used to separate surface and diffusion-controlled contributions to the current at different potentials.

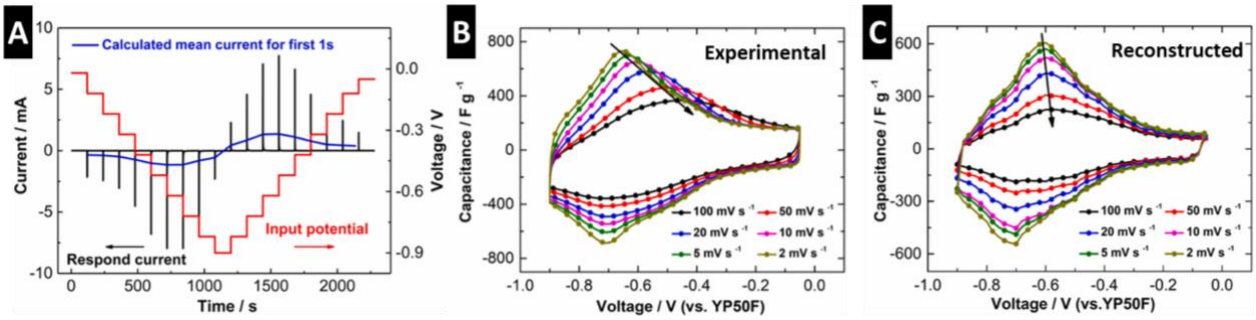

Figure 10: Demonstration of the multiple-step chronoamperometry (MUSCA) technique: (A) The potential waveform and current response of a $Ti_3C_2T_x$ MXene electrode in aqueous 3 M H_2SO_4. (B) Experimental cyclic voltammograms and (C) reconstructed cyclic voltammograms at sweep rates from 2-100 mV/s. Adapted from Ref. [83], Copyright 2019, with permission from Elsevier.

Donne et al. developed the voltammogram reconstruction method as part of step potential electrochemical spectroscopy (SPECS),[86–89] which aims to deconvolute electrochemical mechanisms by fitting the current response ($i_{overall}$) with linear combinations of capacitive (i_C), diffusion-controlled (i_D), and residual (i_R) currents:

$$i_{overall} = i_C + i_D + i_R \quad (14)$$

The Donne group used SPECS to study the relative contributions of different charge storage processes in electrodeposited MnO_2.[87,89,90] **Fig. 11A** shows an example of the linear combination of the capacitive current, diffusion-controlled current, residual current, and the fitted overall current for a selected potential step. Reconstructing all the current contributions over a selected Δt at each potential step lead to the voltammograms as shown in **Fig. 11B**.

It is important to carefully choose appropriate assumptions and the sets of equations to describe the current response based on the electrochemical system as well as using knowledge of the system to ensure that the model makes physical sense. Forghani and Donne compared the deconvolution of capacitive and diffusion-controlled current via SPECS to Conway's k_1, k_2 analysis, and "Trasatti's method" (to be introduced next), and found that SPECS can provide analysis over the full range of sweep rates as well as information on the residual current and electrode stability.[89] Both SPECS and MUSCA techniques were recently validated theoretically by the Pilon group using the continuum modified Poisson-Nernst-Planck model coupled with the Frumkin-Butler-Volmer theory for pseudocapacitive electrodes.[91]

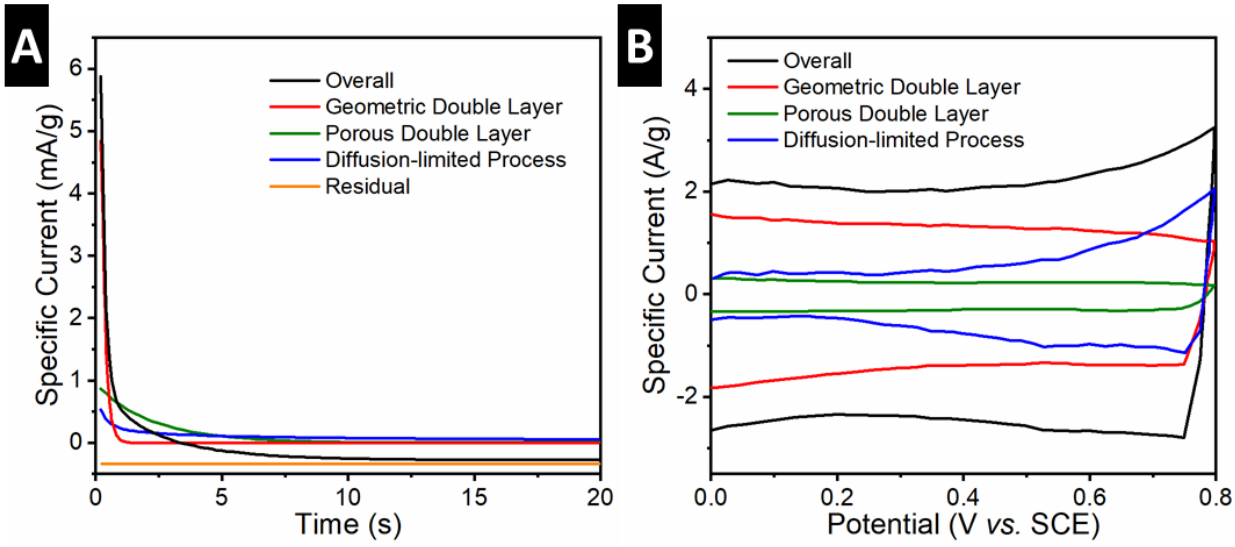

Figure 11: Demonstration of step potential electrochemical spectroscopy (SPECS): (A) Fitting of current vs. time data of a single potential step with the SPECS technique showing the contributions from diffusion-controlled current, capacitive currents, and residual current. The dataset was collected on anodically electrodeposited thin films of MnO_2 in aqueous 0.5 M K_2SO_4. Adapted from Ref. [87], Copyright 2017, with permission from Elsevier. (B) Reconstructed voltammograms of electrolytic manganese dioxide in aqueous 0.5 M K_2SO_4 at 125 mV/s with the SPECS technique. SCE stands for the saturated calomel electrode. Adapted with permission from Ref. [89]. Copyright 2018 IOP Publishing.

The *b*-value analysis, k_1, k_2 analysis, MUSCA, and SPECS discussed above are methods to interpret current responses measured directly from electrochemical characterization techniques. Trasatti et al. developed a method based on voltammetric charge to deconvolute the "inner" (less accessible) and "outer" (more accessible) surface contributions.[23] In this method, it is assumed that the voltammetric charge (Q) can be divided into surface-controlled and diffusion-controlled contributions so that:

$$Q = Q_s + Q_d \tag{15}$$

where Q_s and Q_d are the surface-controlled and diffusion-controlled contributions to charge, respectively. Then, the surface-controlled component can be further divided into the "inner" surface contribution, $Q_{s,in}$, and "outer" surface contribution, $Q_{s,out}$:

$$Q_s = Q_{s,in} + Q_{s,out} \tag{16}$$

It is assumed that the "inner" surface contribution is sweep rate dependent (due to lower accessibility of redox sites) and that the "outer" surface contribution is invariant of sweep rate, which yields:

$$Q_s = \begin{cases} Q_{s,out} & \text{when } \nu = \infty \\ Q_{s,in} + Q_{s,out} & \text{when } \nu = 0 \end{cases} \tag{17}$$

With these boundary conditions, the values of $Q_{s,out}$ and $Q_{s,in}$ can be extrapolated by plotting the charge as a function of sweep rate. Assuming semi-infinite linear diffusion and a linear relationship between Q_d and $\nu^{-1/2}$, **Equation 15** can be rearranged to determine $Q_{s,out}$ when $\nu = \infty$,

$$Q = Q_{s,out} + A_1 \nu^{-1/2} \tag{18}$$

where A_1 is a constant. In a plot of Q vs. $\nu^{-1/2}$, the y-intercept ($\nu^{-1/2} = 0$; or $\nu = \infty$) determines $Q_{s,out}$, as shown in **Fig. 12A**. On the other hand, $Q_{s,in}$ is determined when $\nu = 0$. Assuming Q^{-1} decreases linearly with $\nu^{1/2}$, **Equation 15** is rewritten as

$$Q^{-1} = Q_s^{-1} + A_2 \nu^{1/2} \quad (19)$$

where A_2 is another constant. As shown in **Fig. 12B**, Q_s^{-1} can be obtained from the *y*-intercept ($\nu^{1/2} = 0$) in a plot of Q^{-1} vs. $\nu^{1/2}$. $Q_{s,in}$ is then obtained with **Equation 17**.

This technique has drawn criticism[92] due to its inability to represent the entire range of Q vs. ν behavior. Similarly to k_1, k_2 analysis, the "Trasatti" method does not account for Ohmic losses or irreversible side reactions but is assumed to be valid in a certain reliability range, which minimizes the contribution of such factors.[93]

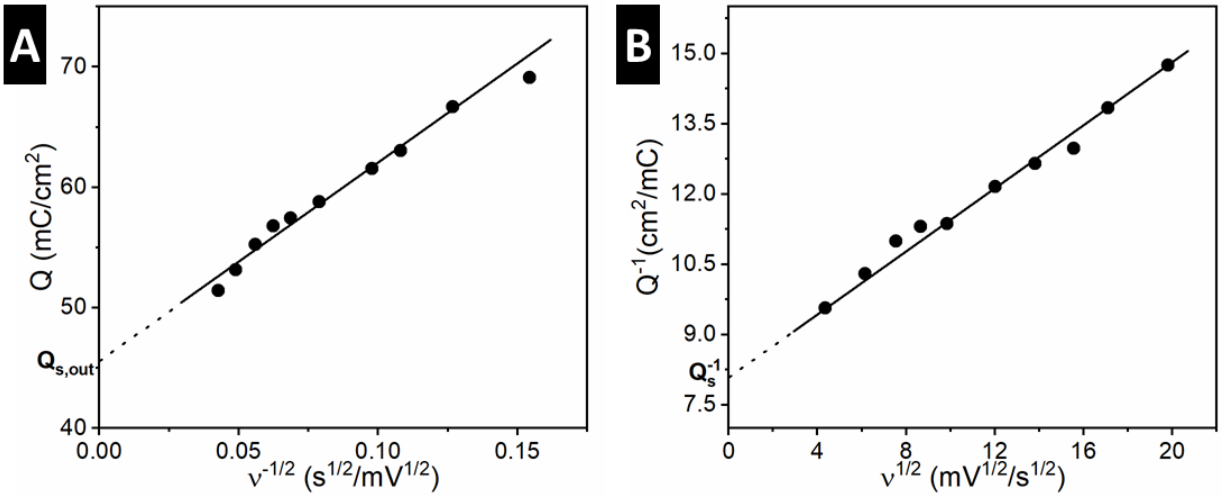

Figure 12: Demonstration of the Trasatti method: (A) A typical voltammetric charge Q vs. $\nu^{-1/2}$ plot for $RuO_2 \cdot nH_2O$ in aqueous 1 M $HClO_4$. The *y*-axis intercept gives the capacity due to the "outer" surface-controlled process. (B) A typical inverse voltammetric charge Q^{-1} vs. $\nu^{1/2}$ plot for $RuO_2 \cdot nH_2O$ in aqueous 1 M $HClO_4$. The *y*-axis intercept gives the inverse capacity due to both "inner" and "outer" surface-controlled processes. Adapted from Ref. [23], Copyright 1990, with permission from Elsevier.

Another method to discriminate charge storage mechanisms is via electrochemical impedance spectroscopy coupled with PITT. Modeling of impedance data is a common method to interpret the electrochemical behavior of materials, and the use of equivalent circuit models aims to distinguish pseudocapacitance from double-layer capacitance.[81] Brezesinski et al. carried out EIS on polymer-templated CeO_2 in a non-aqueous Li^+ electrolyte at various potentials and interpreted the data with the model in **Fig. 13A**, where R_{el}, R_F, CPE_{dl}, and CPE_{pseudo} are the resistance of the electrolyte, the Faradaic charge transfer resistance, a constant phase element for double-layer capacitance, and a constant phase element for pseudocapacitance, respectively. The impedance (Z) of porous pseudocapacitive electrodes is frequently expressed as a constant phase element (CPE) to model a distribution of capacitance values:[94–97]

$$Z_{CPE} = [B(j\omega)^p]^{-1} \quad (20)$$

where j is the imaginary unit, ω is the angular frequency, and B and p are frequency-independent adjustable constants. When p = 1.0, ideal capacitor behavior is observed, and B is the capacitance of the electrode; when p = 0.5, Z_{CPE} describes the Warburg diffusion impedance of a semi-infinite medium.[97] Fitting the impedance data with this model can give an estimate of double-layer capacitance and pseudocapacitance contributions at various potentials, as shown in **Fig. 13B**. **Fig. 13C** shows an example of the measured impedance data and model fit data presented as a Nyquist plot (negative imaginary impedance, $-Z''$, as a function of real impedance, Z').

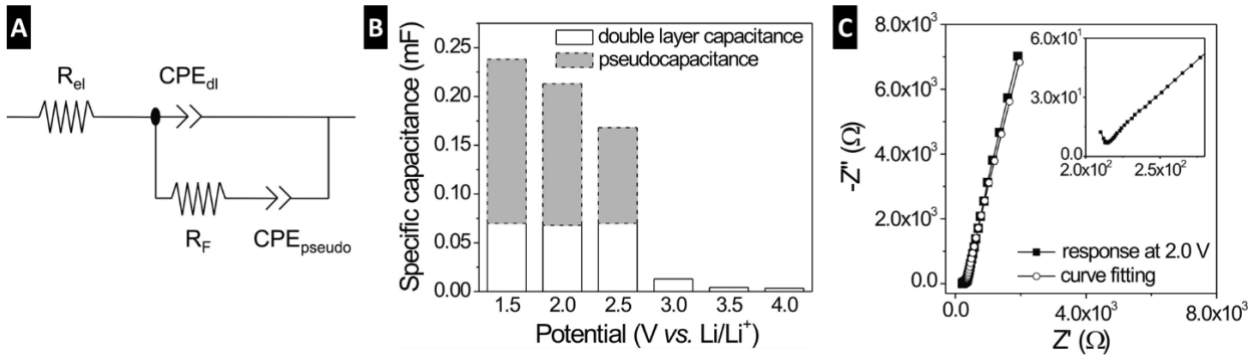

Figure 13: Demonstration of impedance data modeling to determine capacitive contributions: (A) An equivalent circuit model to describe the impedance behavior of polymer-templated CeO_2 in a non-aqueous Li^+ electrolyte. (B) Contributions from double-layer capacitance and pseudocapacitance at various potentials. The specific capacitance was distinguished from diffusion-controlled contributions using k_1, k_2 analysis of cyclic voltammetry data. (C) Nyquist plot of the impedance data collected at 2.0 V vs. Li/Li^+, comparing the measured and model fit data. The inset shows an expanded view of the low Z' region. Adapted from Ref. [81]. Copyright 2010 American Chemical Society.

Bode plot analysis is an alternative to equivalent circuit modeling of EIS data that can also be useful for understanding pseudocapacitance. Typically, in 2D Bode plots, the dependent variables are capacitance, C, and phase angle, φ, as a function of angular frequency, ω, and 3D Bode diagrams are plots of the capacitance (both real and imaginary) and phase angle as a function of potential (obtained from PITT) and frequency (obtained from EIS).[78,98–101] The term "capacitance" here describes the response of an electrode to the applied perturbation, assuming that its impedance can be modeled as a frequency-dependent resistor and capacitor in series.

Using such an equivalent circuit, the capacitance can be separated into real, *C*', and imaginary, *C*'', components:[102]

$$C'(\omega) = \frac{-Z''}{\omega|Z|^2} \quad (21)$$

$$C''(\omega) = \frac{-Z'}{\omega|Z|^2} \quad (22)$$

C' measures the charge reversibly stored at a given frequency, and at a low frequency, it corresponds to the capacitance of the electrode calculated from cyclic voltammograms. *C*'' correlates with energy dissipation by kinetically irreversible processes or diffusion limitations. The maximum of *C*'' vs. frequency defines a dielectric relaxation time constant, τ,[103] as the reciprocal of the characteristic frequency, where the circuit transits from purely resistive to purely capacitive behavior. The phase angle φ contains information on the relative contributions of capacitive and resistive elements with φ = -90° for ideal capacitors, φ = 45° for diffusion-controlled processes, and φ = 0° for resistors.[73] Shown in **Fig. 14A-C** are the 3D Bode plot representations of the area-normalized real capacitance vs. frequency vs. the potential for capacitive, pseudocapacitive, and battery-like electrodes. The capacitive and pseudocapacitive plots feature nearly constant *C*' values across a wide range of potentials at low frequencies in contrast to the battery-like one. Comparison of the capacitive and pseudocapacitive plots indicate a stronger frequency dependence in the latter, and a longer τ (1 s vs. 10 s).

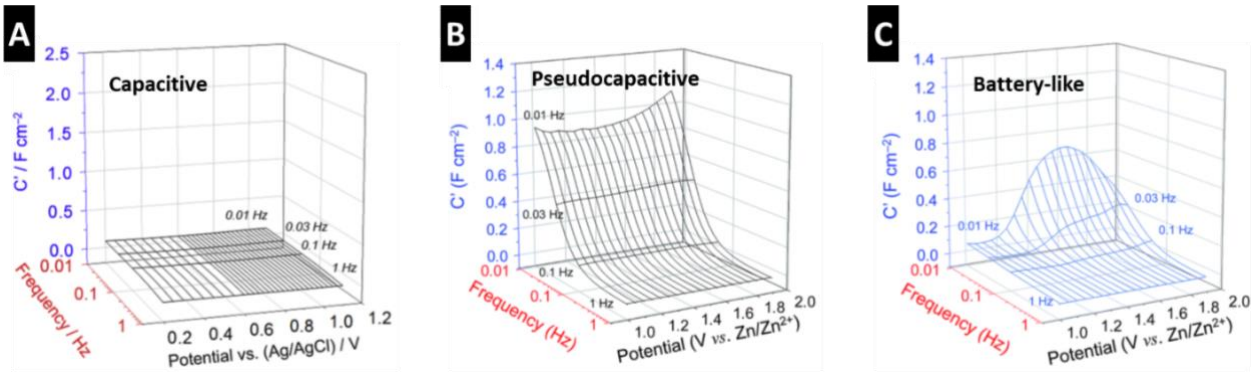

Figure 14: Demonstration of 3D Bode plots for three types of electrodes cycled in aqueous electrolytes: *C'* vs. frequency vs. potential for (A) capacitive carbon nanofoam (CNF) paper, (B) pseudocapacitive MnO_x on CNF, and (C) battery-like MnO_x on CNF. Panel A is adapted from Ref. [78], Copyright 2018, with permission from Elsevier. Panels B and C are adapted from Ref. [100] with permission of The Royal Society of Chemistry; permission conveyed through Copyright Clearance Center, Inc.

3.4 Fundamental Understanding of Pseudocapacitance in Hydrous Transition Metal Oxides

Hydrous RuO_2 ($RuO_2{\cdot}nH_2O$), iridium oxide (IrO_x), and MnO_2 (typically birnessite δ-MnO_2, of the type $K_xMnO_2{\cdot}nH_2O$) are among the best-studied materials exhibiting pseudocapacitive properties and continue to serve as model materials for the fundamental understanding of pseudocapacitance. The surface area-normalized capacitance for hydrous RuO_2 ranges from 150 – 1200 μF/cm^2, depending on the preparation method, with an almost ideally capacitive CV response for the optimum water content of 0.5 H_2O per RuO_2.[24,104] This capacitance is at least an order of magnitude greater than what is typically measured for carbon materials including graphene (~ 4 - 16 μF/cm^2).[75] One of the most comprehensive mechanistic studies of hydrous RuO_2 was performed by Dmowski et al., who combined electrochemical analysis with structural

characterization via X-ray diffraction (XRD) and pair distribution function (PDF).[64] In line with other reports,[24] they found that the magnitude of the capacitance in acidic electrolytes varied with the water content of $RuO_2 \cdot nH_2O$, with a maximum at n = 0.58. This led to a gravimetric capacitance of 850 F/g over a 0.6 V window (142 mAh/g, corresponding to 0.76 e^- transferred per Ru) while exhibiting an ideally capacitive voltammetric response (**Fig. 15A**). Moreover, the PDF results indicated no amorphous features or mixtures of crystalline and amorphous grains. The proposed structural model (**Fig. 15B**) of the hydrous RuO_2 consisted of nanocrystalline, anhydrous RuO_2 grains exhibiting metallic conductivity separated by chemisorbed or physisorbed water and/or protons. In this way, the material exhibited high electronic conductivity (from the anhydrous RuO_2) and proton conductivity (from the hydrous grain boundaries).

Yoshida et al. utilized small-angle X-ray scattering (SAXS) to investigate the effects of water content on charge storage in $RuO_2 \cdot nH_2O$.[65] These measurements revealed that the observed capacitance values were directly correlated with the accessible surface area of RuO_2 aggregates (related to the annealing temperature and water content (**Fig. 15C**)), indicating that the charge storage mechanism occurred directly on the surface of the aggregates and not in the bulk of the nanocrystalline grains. Assuming an oxidation state change of Ru from +4 to +3 upon electrochemical reduction (experimentally confirmed via shifts in the Ru L-edge using in situ X-ray absorption near-edge structure, XANES (**Fig. 15D**)),[105,106] the SAXS results estimate the reactive layer to be on the order of one unit cell, suggesting that the outermost layer of RuO_2 aggregates is responsible for the pseudocapacitive charge storage. A recent first-principles DFT study supported this structural model.[107] However, DFT results also suggested that due to the metallic conductivity of hydrous RuO_2, the electronic charge associated with the reaction of one

proton is distributed between the newly formed O-H bonds and Ru 4d states, with only a partial electron transfer (0.3) to the ruthenium metal centers, leading to charge delocalization. Overall, these fundamental studies reveal that the pseudocapacitive charge storage observed in hydrous ruthenium oxide electrodes is afforded by the excellent electronic and ionic transport through combined metallic conductivity and facile ion transport pathways between grain boundaries. The reduction of Ru upon negative polarization is indicative of a Faradaic process that cannot be explained solely by non-Faradaic double-layer formation.

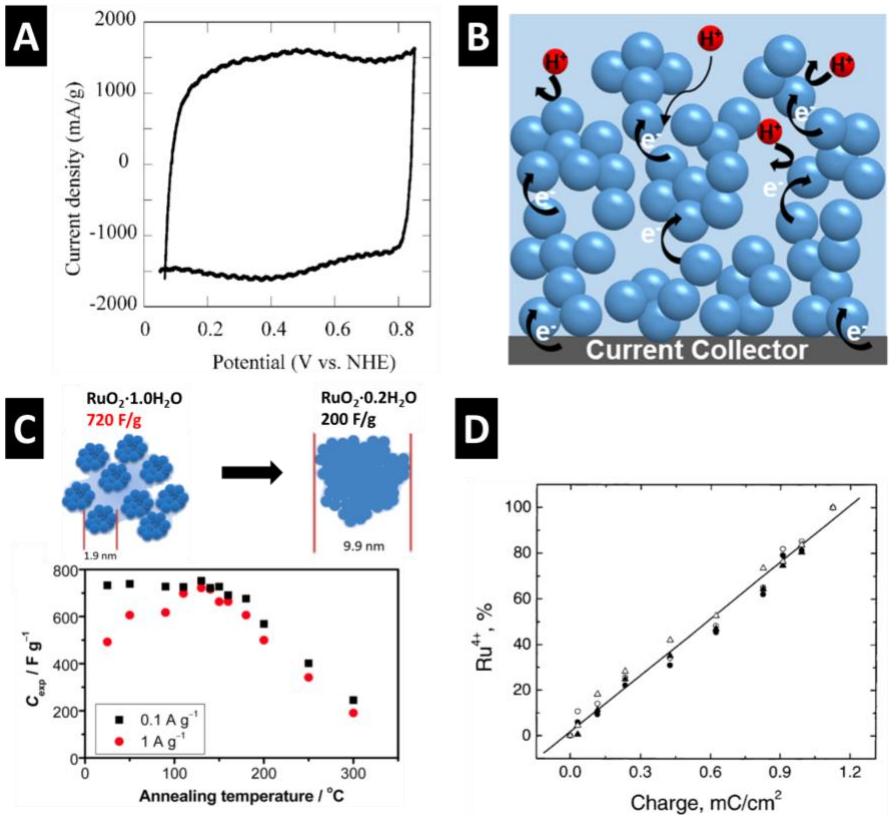

Figure 15: (A) Representative cyclic voltammogram of $RuO_2{\cdot}0.58H_2O$ measured in an acidic electrolyte at a sweep rate of 2 mV/s. Adapted from Ref. [64]. Copyright 2002 American Chemical Society. (B) Structural model of $RuO_2{\cdot}nH_2O$, depicting clusters of rutile RuO_2 formed into loose aggregates separated by hydrous grain boundaries. (C) Specific capacitance as a function of annealing temperature for $RuO_2{\cdot}nH_2O$ electrodes. As the annealing temperature increases, the average water content decreases, and the aggregate size increases, leading to a decrease in ionic conduction pathways and lowered specific capacitance. Adapted from Ref. [65]. Copyright 2013 American Chemical Society. (D) Linear correlation between the amount of Ru^{4+} (determined via deconvolution of the Ru L_{II} and L_{III} edges via in situ XANES) and anodic charge. Adapted from Ref. [106]. Copyright 2002 American Chemical Society.

IrO_x is another hydrous noble metal oxide that exhibits pseudocapacitive behavior. The CV typically exhibits two sets of broad, reversible peaks in the same potential regime as hydrous RuO_2 (~ 0 – 1.2 V vs. SCE).[108] Operando energy dispersive X-ray absorption spectroscopy (EDXAS) revealed that these peaks are due to the reversible oxidation of Ir^{3+} to Ir^{4+}, and Ir^{4+} to Ir^{5+}.[109,110] Since IrO_x is an electrochromic oxide, Chen et al. utilized an optical technique, operando differential reflectance spectroscopy, to track the dynamics of the charge storage process.[108] The normalized change in optical reflectance was found to be proportional to the charge. Further analysis revealed differences between the rate of electrochemical charge injection/release and the rate of optical change. This was explained on the basis of two types of energy storage processes: fast EDL charging due to the intrinsic electronic conductivity of IrO_x, and slower pseudocapacitive charging associated with the redox of Ir that gave rise to the optical change. This study is important because it highlights the coupling between non-Faradaic and Faradaic charging in metallically conductive materials with redox activity. It also delineated pseudocapacitive processes as those that would give rise to electrochemically-induced optical changes as well as changes in the local environment (e.g. bonding distances) of the redox site.

Manganese oxides are more abundant and less expensive than hydrous noble metal oxides, and exhibit highly symmetric, capacitive cyclic voltammograms in neutral aqueous electrolytes (**Fig. 16A**). They exhibit rich polymorphism, which leads to tunable electrochemical behavior,[111] but have an intrinsically low electronic conductivity compared to the metallically conductive hydrous ruthenium and iridium oxides.[112] Increasing the surface area of various allotropes of crystalline MnO_2 electrodes up to 200 m^2/g led to a maximum in specific capacitance, but the further increase did not enhance the charge storage.[113] This has been attributed to the

strong dependence of the ionic conductivity on the microstructure rather than the specific surface area.[111] While many polymorphs of manganese oxide contain structural water, they lack the hydrous grain boundaries found in $RuO_2 \cdot nH_2O$. Electrodes which utilize large particles or thick films of manganese oxides (above few hundred nm) obtain only a fraction (~ 20 %) of the theoretical capacitance for a one-electron redox.[111,114–116] It is hypothesized that the limited electronic conduction and inter-granular ionic transport in manganese oxides limit bulk intercalation and hence the specific capacity, as indicated by results that suggest Mn surface atoms are responsible for the majority of the pseudocapacitive charge storage.[115,116] A comparison between LiCl, NaCl, and KCl as electrolyte salts showed that K^+ provided the most attractive rate performance, evidenced by the rapid current response at the vertex potential.[26] It was hypothesized that the kinetics of the surface redox process were limited by cation (de-)solvation. The hydrous solvation shell is larger for smaller cations ($Li^+ > Na^+ > K^+$), which was hypothesized to increase the time for (de-)solvation process at the electrochemical interface.[26]

In a further study, manganese oxide was prepared by a sol-gel process with subsequent dip-coating and calcination.[117] The obtained thin film electrodes exhibited a capacitance of up to 700 F/g (175 mAh/g) in aqueous Na_2SO_4. The authors claimed that the intercalation of protons from the aqueous electrolyte contributed to the increased capacitance.[117] Toupin et al. conducted *ex situ* XPS to compare the change of manganese oxidation state in thin film and thick composite electrodes of hydrated MnO_2.[116] They concluded that only a thin layer of MnO_2 participates in the pseudocapacitive reaction because no change in manganese oxidation state was observed in composite MnO_2 electrodes. In the case of thin film electrodes, the Mn oxidation state changed from +3.6/3.7 in the as-prepared sample, to +4 during oxidation to 0.9 V, to +2.9 during reduction

to 0 V (vs. Ag/AgCl). Further, the amount of chemisorbed Na^+ measured by XPS was not enough to account for the complete reduction of Mn^{4+} to Mn^{3+}, which implied the involvement of protons in the charge storage mechanism.

In situ and operando characterization continue to advance the understanding of pseudocapacitive charge storage mechanisms in manganese oxides. In situ XANES results revealed a direct correlation between the applied potential and electronic structure of Mn in birnessite ($K_{0.15}MnO_2 \cdot nH_2O$)[118] and amorphous electrodeposited manganese oxide electrodes.[66] Both studies observed an increase in the Mn K-edge binding energy as a function of increasing electrode potential, indicating increased oxidation of the Mn metal center, as shown in **Fig. 16B**.[66] Raman spectroscopy of birnessite MnO_2[119–121] and spinel Mn_3O_4[122] also revealed changes in the spectral features as a function of applied potential. Chen et al. observed reversible spectroscopic changes in the Raman spectrum upon charge / discharge in pH-neutral aqueous electrolytes, with the evolution of both inter- and intra-layer Mn-O stretching bands during electrochemical cycling (**Fig. 16C**).[119] Additionally, XRD techniques indicate a solid-solution intercalation pseudocapacitance mechanism in various MnO_2 allotropes due to changes in the interplanar distances as a function of state-of-charge in pH-neutral aqueous electrolytes (**Fig. 16D**).[112,123] These findings indicate two major insights into the charge storage mechanisms of manganese oxides in pH-neutral aqueous electrolytes: (i) the interior of manganese oxides can accommodate cations, and (ii) the Mn metal centers are undergoing Faradaic charge transfer, leading to changes in the electronic structure and binding environments of the Mn metal centers. However, the limited capacity of thick manganese oxide electrodes caused by the low electronic and ionic conductivity remains a practical issue for energy storage applications.

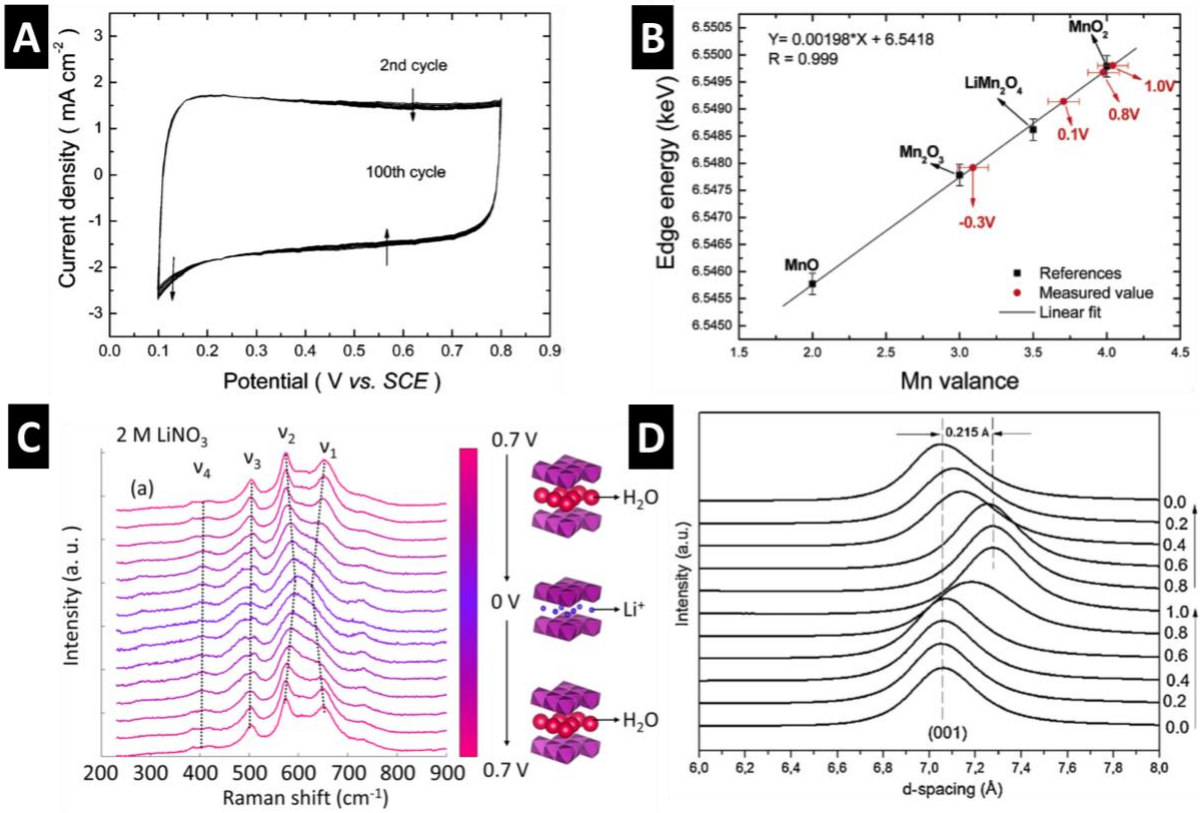

Figure 16: (A) Cyclic voltammograms of an electrodeposited amorphous manganese oxide at 10 mV/s in aqueous 2 M KCl depicting the ideally capacitive response, which is commonly observed in various allotropes. (B) In situ XANES of the manganese oxide electrodes cycled in (A), correlating the Mn K-edge binding energy to its valence by calibration with several Mn_xO_y reference standards. Panels A & B adapted from Ref. [66]. Copyright 2007 American Chemical Society. (C) Evolution of the Raman spectra of δ-MnO_2 during electrochemical charge / discharge in 2 M $LiNO_3$. Panel adapted from Ref. [119]. Copyright 2015 American Chemical Society. (D) Evolution of the (001)-diffraction peak of a β-MnO_2 electrode during reversible electrochemical cycling in 1 M LiCl. Panel adapted from Ref. [123], Copyright 2012, with permission from Elsevier.

Hydrous transition metal oxides are model oxide materials for understanding the fundamental nature of pseudocapacitance. The changes observed by in situ and operando studies cited above strongly suggest that Faradaic reactions contribute to the nearly ideal capacitive voltammetric response common to the materials in aqueous electrolytes. It is likely that in these high surface area and hydrated materials, the distinction between double-layer and pseudocapacitive mechanisms becomes blurred, and further understanding, particularly at the atomistic level, is necessary. Nevertheless, most experimental studies indicate that the materials undergo measurable changes in their physicochemical properties upon electrochemical cycling. This is a strong indication that the charge storage process is at least in part Faradaic in origin.

3.5 Understanding of Pseudocapacitive Mechanisms from Theory and Computation

Modeling of pseudocapacitive materials is particularly challenging because of the intricacy of their electrochemical interface, where a multitude of physical and chemical processes have to be considered, including ion diffusion, double-layer formation, charge transfer, and intercalation reactions.[124] Depending on the length and time scales of interest, different computational methods are required (**Fig. 17**). The continuum model is usually applied to simulate realistic devices by solving electro-kinetics equations, such as the Butler-Volmer equation and the Poisson-Nernst-Planck equation, to understand the electrochemical behavior governed by the electrode potential, scan rate, and ion diffusion. First-principles simulation captures the effects of the electronic structure of the electrode materials, such as dopants, defects, and functional groups, but is limited by the accessible length and time scales due to the high cost of quantum mechanical computations. In recent years, several newly developed tools,[125–128] such as machine learning,

have exhibited promising capability in solving the complexity of the electrochemical interface. Here, we review several theoretical and computational studies on the mechanistic understanding of pseudocapacitance, from continuum to first principles.

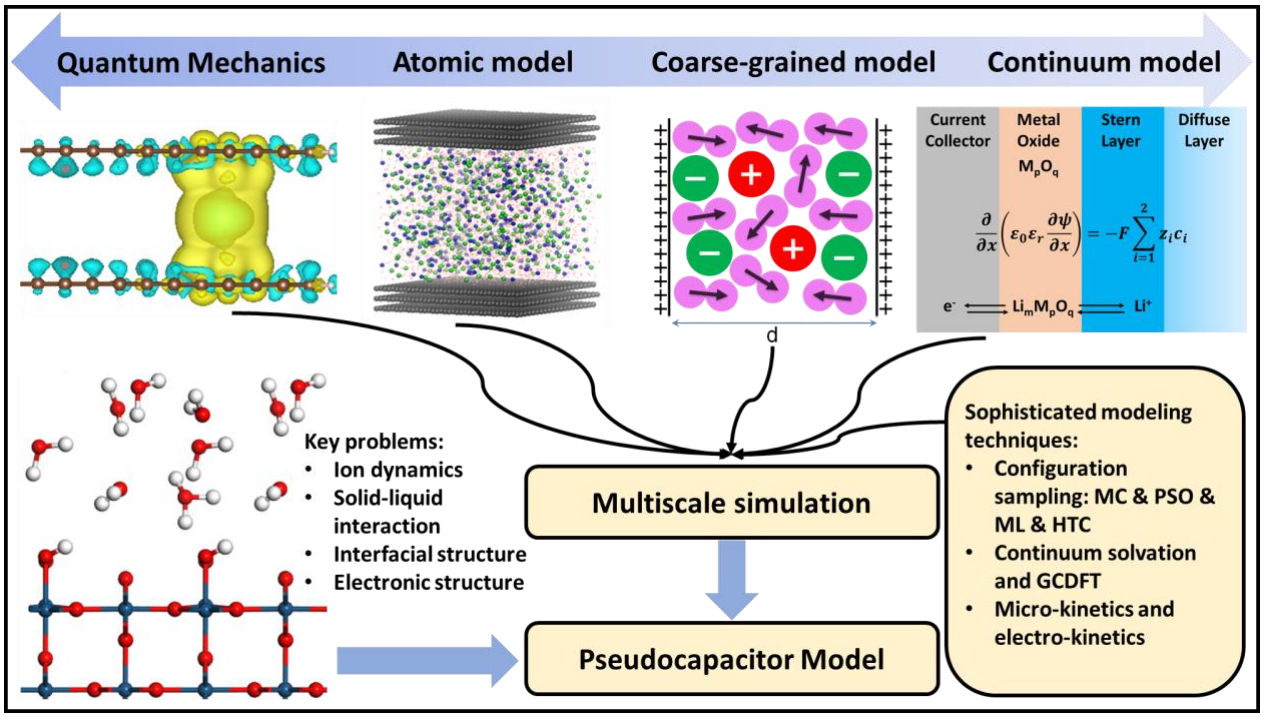

Figure 17: Classification of simulation methods in the field of electrochemical energy storage. MC: Monte-Carlo; PSO: Particle swarm optimization; ML: Machine learning; HTC: High-throughput computation; GCDFT: Grand-canonical density functional theory.

Girard et al. used a generalized modified Poisson-Nernst-Planck model to simulate the charge storage mechanism of T-Nb_2O_5 in a non-aqueous Li^+ electrolyte.[129,130] Based on a simple cell structure (**Fig. 18A**), numerically generated cyclic voltammograms matched the experimental ones. The simulated cyclic voltammograms were divided into two regimes (**Fig. 18B**): a capacitive regime, dominated by electrical double-layer formation at higher potentials, and a Faradaic

regime, dominated by Li^+ intercalation at lower potentials. Their simulation revealed that Li^+ ions are electrostatically repelled from the electrochemical interface in the capacitive regime, causing a reduced Faradaic current due to Li^+ starvation.[130] The experimentally observed dip in the b-value that signifies a kinetically slow process was proposed to be due to a transition from the capacitive to the Faradaic regime.[129,130] In order to improve the device performance, the effect of electrode thickness, Li^+ diffusion coefficient, and reaction rate were systematically explored via the continuum model,[131] which offers possible strategies to enhance the capacitive performance in further experimental work (**Fig. 18C-D**).

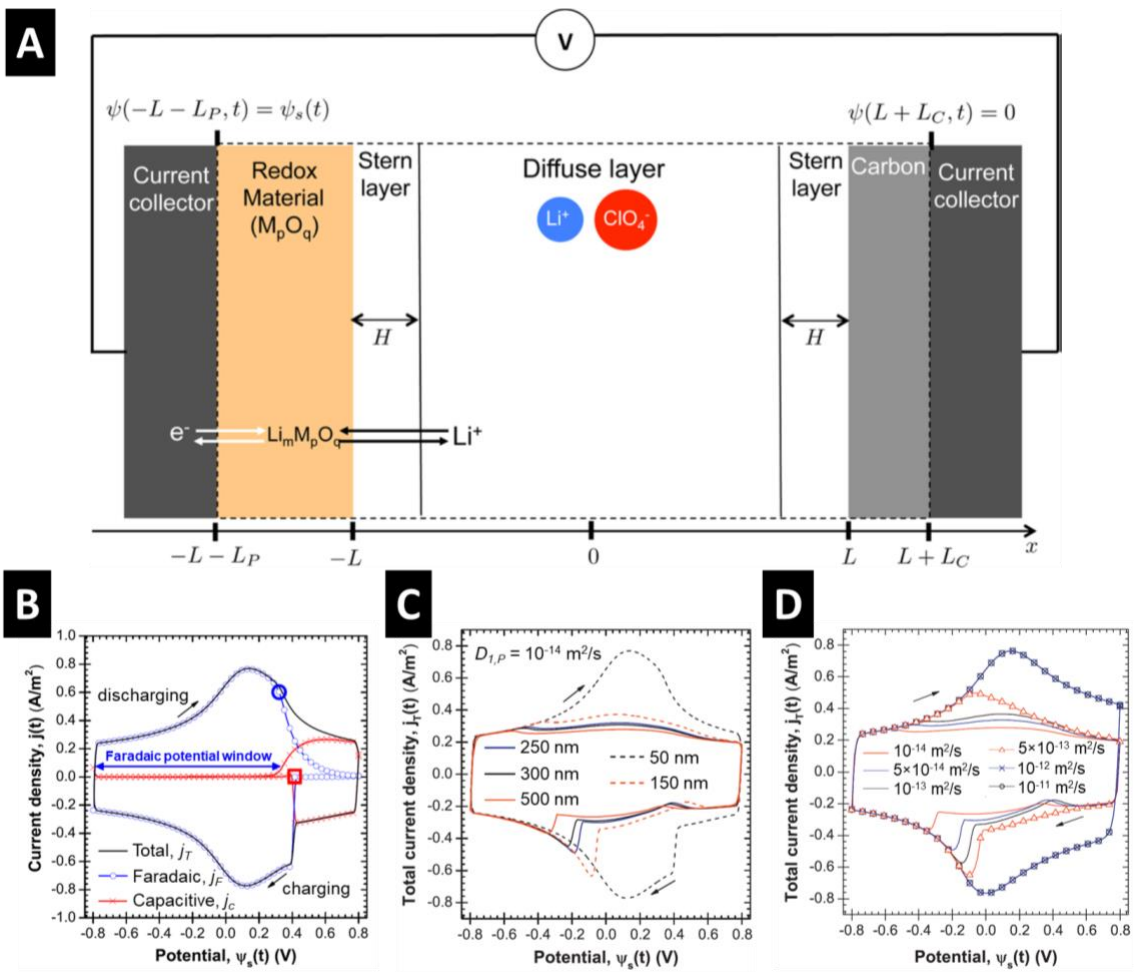

Figure 18: (A) Schematic of a 1D model for a hybrid cell consisting of a pseudocapacitive electrode and a carbon electrode in a non-aqueous Li^+ electrolyte. The dashed line encloses the simulation domain. Reprinted from Ref. [129]. Copyright 2015 American Chemical Society. (B) Simulated capacitive $j_C(t)$, Faradaic $j_F(t)$, and total $j_T(t)$ current densities at the electrode/electrolyte interface at a scan rate v = 1 V/s, electrode thickness L_P = 50 nm, and Li^+ diffusion coefficient in the electrode $D_{1,P} = 10^{-14}$ m^2/s. Simulated total current density at different (C) electrode thickness, (D) Li^+ diffusion coefficient. Adapted from Ref. [131], Copyright 2015, with permission from Elsevier.

First-principles simulation can directly capture the thermodynamic potentials as well as the electronic structure of the electrochemical interface in contrast to the continuum model, which requires the reaction free energy and transport barrier as input parameters. For instance, Kang et al. employed first-principles DFT calculations to reveal a similar capacitive-to-Faradaic transition for anatase TiO_2 nanosheets (1.7 nm thickness along the [101] direction).[132] Their results show an energetic favorability for EDL formation of solvated Li^+ at the TiO_2 surface at potentials above 2.2 V vs. Li/Li^+.[132] Only at more negative potentials, subsurface lithiation is predicted to be energetically more favorable.[132] The authors hypothesized that this behavior is transferrable to other electrochemical systems.[132] Tompsett et al. used DFT to analyze the energy barriers associated with Li^+ intercalation in β-MnO_2 to explain the large differences in capacity between mesoporous and bulk electrodes via the generalized gradient approximation with Hubbard U correction (DFT+U).[133] They found a very small Li^+ migration barrier of 0.17 eV in bulk β-MnO_2. However, a high energy barrier of more than 0.6 eV is identified for surface to bulk migration for Li^+ at the (101) surface, which dominates the bulk equilibrium morphology of β-MnO_2.[133] The authors proposed that the increased Li^+ migration barrier from surface to bulk is the reason for the effectiveness of nanostructuring in enhancing rate capability because different facets are exposed at the surface.[133] Similar effects may apply to other electrode materials, and the authors proposed the screening of new energy storage materials for such a surface migration barrier.[133]

First-principles approaches were employed to simulate the RuO_2/water interface to understand the mechanism of the pseudocapacitance of RuO_2 in an acidic electrolyte. Watanabe et al. introduced explicit water layers on the RuO_2(110) surface to include the effect of solvation

in their DFT modeling and found that the orientation of interfacial water molecules has a significant impact on the Fermi energy of RuO_2 (**Fig. 19A**).[134,135] Conversely, the interfacial structure changes with the applied potential (**Fig. 19B**). The calculated Pourbaix diagram (**Fig. 19C**) and Bader charges (**Fig. 19D**) showed that the oxidation state of Ru changes with pH and electrode potential, shedding light on the charge storage mechanism at the RuO_2/water interface.

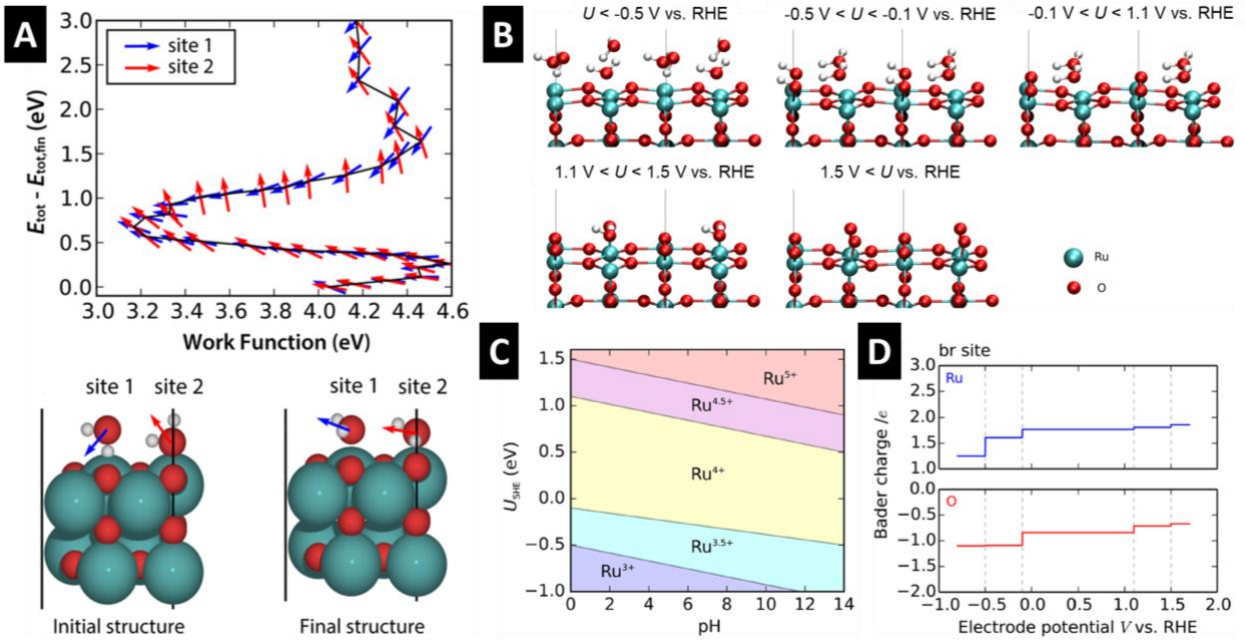

Figure 19: DFT studies of the RuO_2(110)/water interface. (A) Top, change in total energy (relative to the final state), work function, and water orientation (surface dipole) during geometry optimization (from top to bottom); bottom, initial and final structures. Adapted from Ref. [134]. Copyright 2016 American Chemical Society. (B) Potential-dependent RuO_2(110)/water interfacial structures. (C) Pourbaix diagram of RuO_2(110)/water. (D) Bader charges of surface Ru and O atoms as a function of electrode potential. Reprinted from Ref. [135]. Copyright 2017 American Chemical Society.

To go beyond the ideal termination from the bulk structure, Zakaryan et al. applied a global minimization algorithm with DFT to study the surface reconstruction of RuO_2(110) under ambient conditions.[136] They found two stable reconstructions, RuO_4-(2 × 1) and RuO_2-(1 × 1), and further studied the adsorption of hydrogen atoms on the reconstructed surfaces. Their potential profiles with increasing hydrogen coverage are quite different from that of the ideal RuO_2(110) surface, indicating the need for incorporating different surface structures in simulating proton redox on RuO_2(110).

To predict the capacitance of proton reduction at the RuO_2/water interface, Zhan et al. used an implicit solvation model with DFT to directly simulate the proton adsorption on the RuO_2(110) surface.[137] The calculated pseudocapacitance based on the Fermi-level shifts (voltage change) for different hydrogen coverages (charge change) showed good agreement with the experimental values. Keilbart et al. devised a more advanced approach by combining constant-potential Monte-Carlo optimization and first-principles DFT with a self-consistent implicit (continuum) solvation model.[138] The voltage vs. charge profile (**Fig. 20A**) was obtained by optimizing the surface configuration and hydrogen coverage (**Fig. 20B**) and net charge (EDL formation) at a specified electrode potential via a Monte-Carlo algorithm. The comparison between simulation and experiment (**Fig. 20A**) revealed the importance of including the EDL contribution in modeling a pseudocapacitor: the optimal model (including EDL contribution) shows a much better agreement with the experiment than the neutral model (without the EDL contribution). The insertion of protons into the sublayer of RuO_2(110) was found to have a significant impact on the charge-voltage relation.[139] They further simulated and compared the

charging process of different RuO_2 facets, including (110), (101), and (100).[139] This model can be extended to other transition metal oxides.

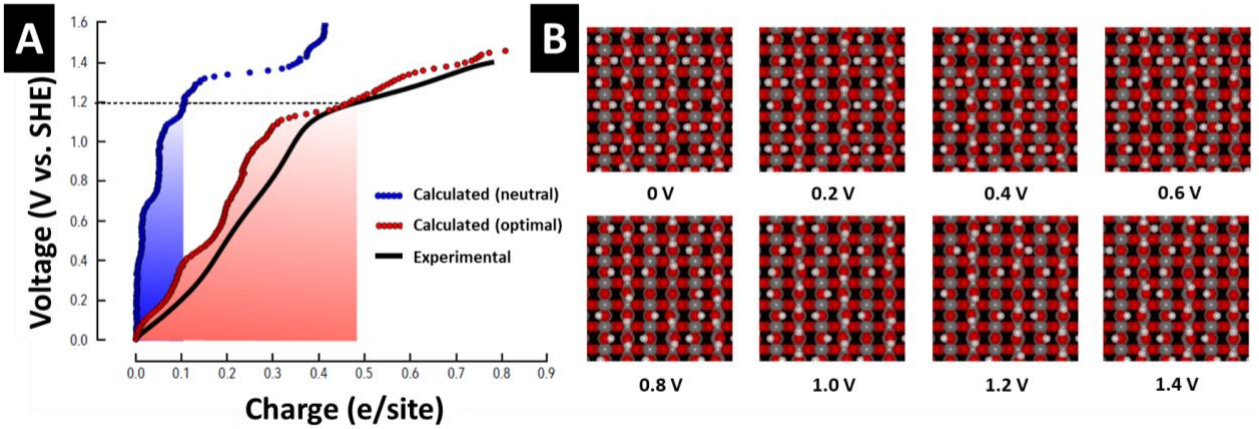

Figure 20: Simulation of the charging of a RuO_2 electrode in an acidic electrolyte. (A) Simulated charge-voltage response of RuO_2(110) in comparison with the experiment: including the computationally determined double-layer capacitance (9.5 μF/cm^2) maximizes the overall pseudocapacitance of the electrode (Optimal: red curve) as compared to the charge without surface electrification (Neutral: blue curve, corresponding to a double-layer capacitance of 0 μF/cm^2). The shaded area determines the energy of the electrode. (B) Voltage-dependent evolution of the surface structure under the predicted optimal capacitance. Adapted with permission from Ref. [138]. Copyright 2017 by the American Physical Society.

4. Emerging Pseudocapacitive Materials and Design Strategies

Progress in emerging pseudocapacitive materials can be divided into three categories: (i) the search for new materials and mechanisms with structural moieties and compositions that enable intrinsic pseudocapacitance, (ii) the design of nanoscale materials to increase surface-controlled contributions, primarily of intercalation-based energy storage materials to enable extrinsic pseudocapacitance, and (iii) the addition of pseudocapacitive functionalities to carbon materials. While transition metal oxides (TMOs) are the most well-known pseudocapacitive materials,[25] there is rapid development in perovskite oxides, chalcogenides, MXenes, and metal-organic frameworks (MOFs) that exhibit pseudocapacitive behavior. Finally, carbon materials constitute most electrodes for commercialized electrochemical capacitors, and one strategy to boost the energy density of these devices is to introduce pseudocapacitance.

4.1 Pseudocapacitive Intercalation in Transition Metal Oxides

The electrochemical intercalation of small cations such as Li^+ into transition metal oxides is typically a diffusion-controlled process at timescales of just a few minutes.[140] There is a significant interest in finding classes of materials with high diffusion coefficients and minimum structural change such that the intercalation is surface-controlled, and thus (intrinsically) pseudocapacitive, at these timescales. Furthermore, new mechanisms such as anion intercalation are currently explored in the search for new, high power energy storage materials.

4.1.1 TiO_2(B)

Monoclinic bronze titanium dioxide (TiO_2(B)), first described by Marchand et al. in 1980,[141] is a metastable polymorph of titanium dioxide, which can be synthesized by hydrolysis and subsequent dehydration of alkali titanates.[142,143] The TiO_2(B) phase has the highest theoretical Li^+ intercalation capacity of all titania polymorphs (Li_xTiO_2(B), with x<1.25, which has a theoretical capacity of 419 mAh/g).[144] However, a maximum of one Li^+ (335 mAh/g) can be intercalated in a desirable potential range above 1 V vs. Li/Li^+, which mostly avoids the formation of the solid-electrolyte interphase (SEI) in non-aqueous electrolytes.[144] Experimentally, maximum lithiation capacities of up to 338 mAh/g ($Li_{1.01}TiO_2$(B)) were reported in nanowires at low galvanostatic rates of 10 mA/g.[145,146] An irreversible capacity loss after the first lithiation was mainly attributed to side reactions of the electrolyte on TiO_2(B) surfaces, which typically exhibit a large amount of -OH groups and surface water, leading to low first cycle Coulombic efficiencies even above 1 V vs. Li/Li^+.[147,148] Zukalóva et al. found that electrochemical intercalation of Li^+ into TiO_2(B) nanofibers was a pseudocapacitive, surface-controlled process with a pair of reversible redox peaks at 1.5-1.6 V vs. Li/Li^+, and a maximum intercalation capacity of 228 mAh/g ($Li_{0.68}TiO_2$(B)).[43] Kinetic analysis showed a linear sweep rate dependence of the cyclic voltammetry peak current at scan rates from 0.1 mV/s to 2 mV/s, whereas diffusion-controlled kinetics were found for anatase TiO_2 under comparable conditions (**Fig. 21A-B**).[43] The pseudocapacitive behavior of TiO_2(B) was attributed to its open structure with ion intercalation channels parallel to the b-axis.[43]

Morphology has a large impact on the electrochemical properties of TiO_2(B). There are three different Li^+ sites in TiO_2(B), namely, C, A2, and A1 (**Fig. 21C**) which exhibit different site energies and diffusion barriers.[149–151] Okumura et al. found that the Li^+ insertion sites in

submicron Li_xTiO_2(B) are dependent upon the Li^+ content, x. X-ray absorption fine structure spectroscopy (XAFS) showed that C- and/or A2-sites are initially filled up to a Li^+ content of x = 0.5, and A1 sites are filled when $x > 0.5$.[152] Dylla et al. combined experiments with modeling and found that the lithiation behavior of TiO_2(B) nanoparticles and nanosheets is different, with a more pseudocapacitive response in nanosheets (**Fig. 21D**).[153] First-principles DFT showed that nanosheets with an elongated geometry along the a-axis had a preferential filling of C-sites due to reduced repulsions between Li^+ in A2-sites and C-sites.[153] It was hypothesized that this repulsion prevents the lithiation of the C-site in nanoparticles, which have a decreased a-axis unit cell parameter.[153]

Hua et al. performed a comprehensive experimental study on the lithiation mechanism of TiO_2(B) nanoparticles by combining in situ X-ray PDF and galvanostatic intermittent titration technique (GITT).[154] The nanoparticles exhibited up to six different lithiation regions (a-f), each with distinct kinetic behavior (**Fig. 21E-F**).[154] At low Li^+ content up to $Li_{0.25}TiO_2$(B), the mechanism involves mostly pseudocapacitive lithiation of the surface sites and the A2-sites via a solid-solution reaction, with fast diffusion along the b-axis channels. Intercalation up to $Li_{0.5}TiO_2$(B) was diffusion-controlled, attributed to Li^+ transport along the c-axis, which is associated with a slower, two-step A2-site filling process.[154] The change in diffusion path at intermediate Li^+ content may be attributed to increasing repulsion from Li^+ sitting in A2-sites.[151,154] Subsequent lithiation up to $Li_{0.75}TiO_2$(B) was via the C'-sites, which are located in the b-axis channel.[144,154] This two-phase reaction was a kinetically rapid process with large pseudocapacitive currents. The final lithiation step inside A1-sites via a solid-solution reaction was diffusion-controlled.[154] These results indicate that the C'-sites and about half of the A2-sites could be accessible for fast charging with surface-

controlled kinetics even in bulk TiO_2(B), while filling of the remaining A2 sites and A1 sites would require nanostructured morphologies and/or low charging currents. It underlines the necessity of advanced characterization tools to reveal the relation between materials structure and electrochemical properties in order to develop high power energy storage materials.

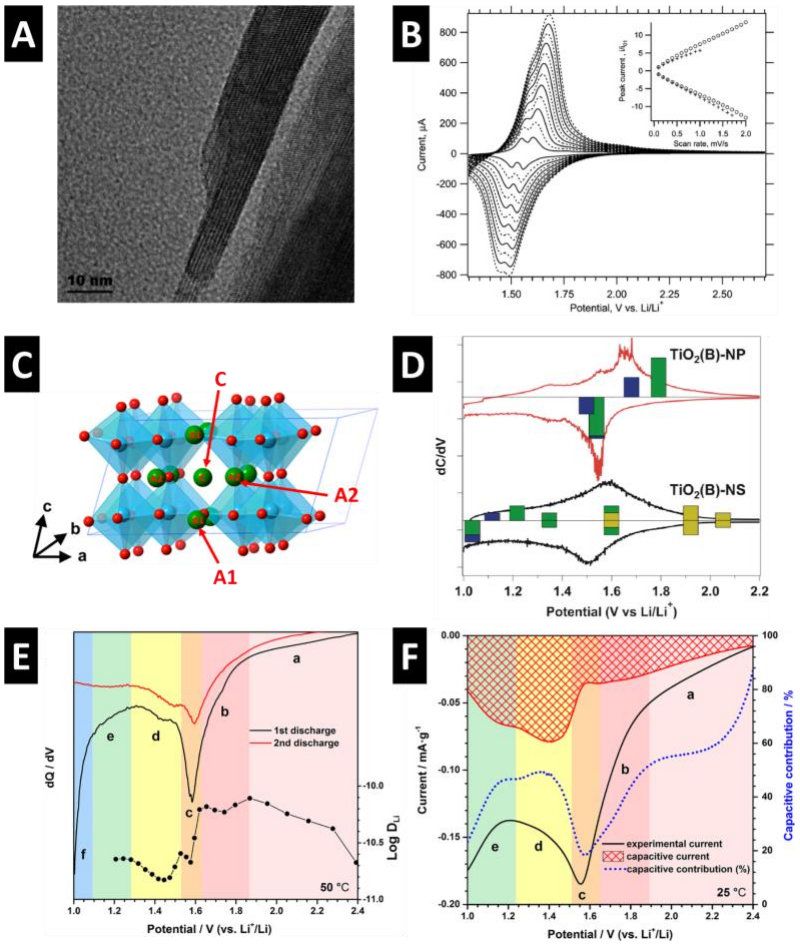

Figure 21: (A) Transmission electron micrograph and (B) cyclic voltammograms of TiO_2(B) at rates of 0.1-1.2 mV/s in a non-aqueous Li^+ electrolyte (inset: normalized peak current versus scan rate). Adapted from Ref. [43]. Copyright 2005 American Chemical Society. (C-D) DFT+U calculated Li^+ insertion sites in TiO_2(B) nanoparticles (NP) and nanosheets (NS) at different potentials, and corresponding cyclic voltammograms indicating Li^+ insertion potentials and relative Li^+ site filling. Adapted from Ref. [153]. Copyright 2012 American Chemical Society. (E) First two galvanostatic discharge cycles of TiO_2(B) with calculated lithium diffusion coefficient D_{Li} from GITT. (F) Voltammetric response indicating surface-controlled (capacitive) contributions. The six distinct intercalation regions are labelled a-f. Reproduced from Ref. [154]. Copyright 2017 American Chemical Society.

4.1.2 T-Nb_2O_5

Niobium pentoxide (Nb_2O_5) has been investigated as a Li^+ intercalation host since the 1980s.[155–158] It can exist as several polymorphs, forming a pseudo-hexagonal structure around 500 °C (TT-Nb_2O_5), an orthorhombic structure around 800 °C (T-Nb_2O_5), a tetragonal structure around 1000 °C (B-Nb_2O_5), and a monoclinic structure above 1100 °C (H-Nb_2O_5).[159] Kumagai et al. discovered that lithiation of T-Nb_2O_5 occurs via a solid-solution process below 2 V vs. Li/Li^+, forming $Li_xNb_2O_5$ up to $x \leq 2$,[156] with a theoretical capacity of 202 mAh/g. Kodama et al. used in situ synchrotron XRD to demonstrate that the original crystal structure of both orthorhombic and tetragonal Nb_2O_5 is maintained during Li^+ intercalation with small changes in unit cell volume and no phase transformations.[159] Using in situ XAFS, the authors further showed that lithiation up to $Li_2Nb_2O_5$ leads to a continuous reduction of Nb^{5+} to Nb^{4+}.[159] In 2010, Brezesinski et al. first reported on the pseudocapacitive Li^+ intercalation kinetics of high surface area, mesoporous, and iso-oriented films of T-Nb_2O_5, but it was hypothesized that the largely surface-controlled kinetics were due to nanostructuring of the material.[82] In a subsequent study, Kim et al. found that Li^+ intercalation in nanoparticle thin-films of orthorhombic and pseudo-hexagonal Nb_2O_5 features pseudocapacitive characteristics that are an intrinsic property of Nb_2O_5.[160] It was hypothesized that lithium diffusion along preferred crystallographic pathways was responsible for the surface-controlled kinetics.[160]

An analysis of the lithiation kinetics and the associated structural response of T-Nb_2O_5 was carried out by Augustyn et al.[44] Cyclic voltammograms of T-Nb_2O_5 in 1 M $LiClO_4$ in propylene carbonate electrolyte at rates between 0.1-500 mV/s, and logarithmic plotting of the peak current versus sweep rate revealed the presence of two kinetic regimes (**Fig. 22A-B**): (i) fully surface-

controlled kinetics up to 20 mV/s (b = 1) with no solid-state diffusion limitations, reaching a specific capacity of about 130 mAh/g within 60 s of charging; and (ii) mainly diffusion-controlled kinetics above 50 mV/s ($0.7 < b < 0.8$).[44] In situ X-ray absorption spectroscopy (XAS) confirmed the continuous change in oxidation state from Nb^{5+} to Nb^{4+} (**Fig. 22C**), and Fourier-transformed extended X-ray absorption fine structure (EXAFS) showed a two-stage intercalation process (**Fig. 22D**): first, various Nb-O bond lengths (1.40-1.80 Å) merged to an intermediate bond length (1.75 Å), followed by an increase of Nb-O distances to 1.85 Å because of increased Li-O interaction with increasing lithiation of the structure.[44] This behavior underlined the need for an intercalation host with an open yet interconnected layered crystal structure to enable fast lithium diffusion with no phase transformation.[44]

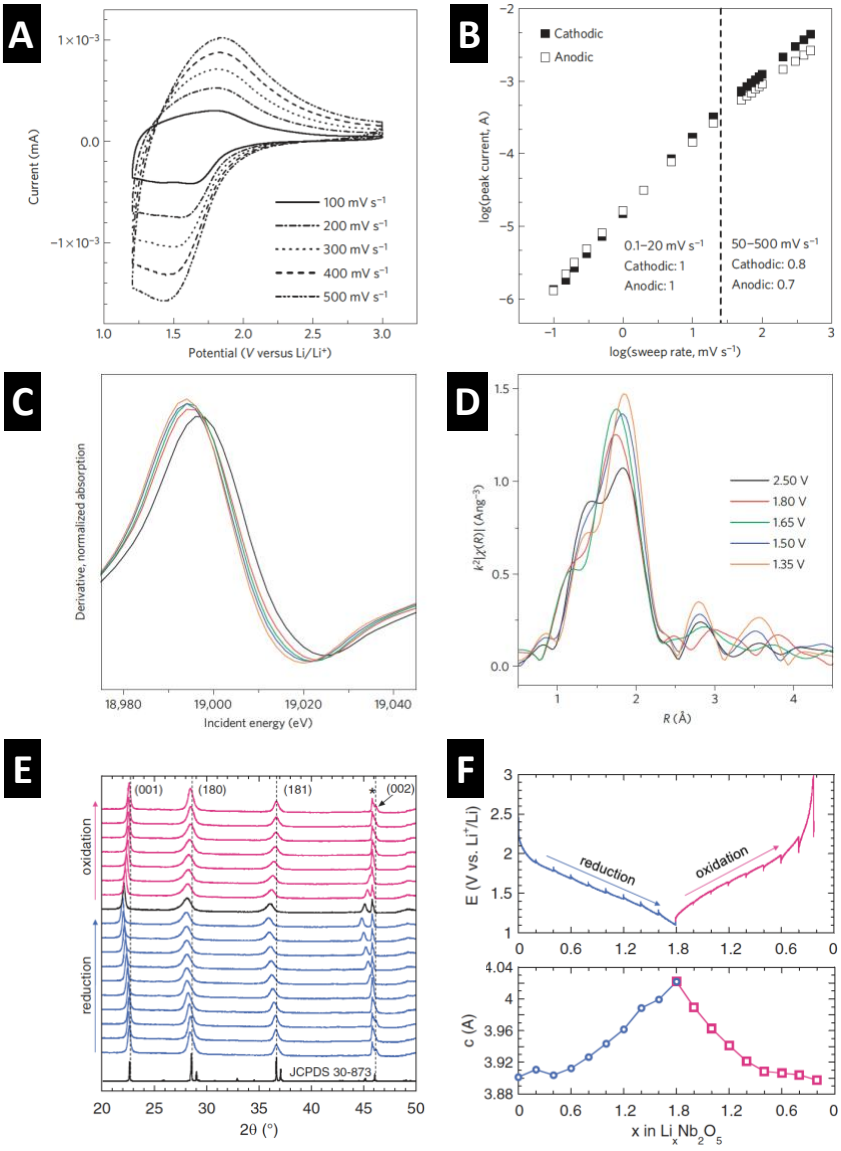

Figure 22: (A) Cyclic voltammograms and (B) *b*-value determination of T-Nb_2O_5 in a non-aqueous Li^+ electrolyte. (C) Derivative of Nb K-edge from electrochemical in situ XAS and (D) k^2-weighted Fourier-transformed K-edge from EXAFS at specific potentials vs. Li/Li^+. Reprinted with permission from Ref. [44]. Copyright 2013 Springer Nature. (E) Electrochemical in situ XRD patterns and (F) corresponding galvanostatic profile and c-lattice parameter change of $Li_xNb_2O_5$ at different lithiation stages. Reprinted with permission from Ref. [46]. Copyright 2014 IOP Publishing.

Griffith et al. confirmed the high lithium mobility in T-Nb_2O_5 via variable-temperature nuclear magnetic resonance (NMR) to reveal very low activation energies of ca. 60-100 meV for Li^+ diffusion, which explained the high rate capability of the material even in micron-sized particles.[161] A study by Come et al. used in situ XRD measurements to confirm the solid-solution lithiation process of $Li_xNb_2O_5$, first demonstrated by Kumagai, up to a Li^+ content of x = 1.8, with an increase of the *c*-axis parameter from 3.91 Å to 4.02 Å (**Fig. 22E-F**).[46] These results, in combination with theoretical work from Liu et al. and Lubimtsev et al., suggested energetically favorable Li^+ diffusion pathways along the (001) planes.[46,162,163] These loosely packed (001) planes, termed 4*g* layers, contain only bridging oxygen atoms, and are arranged alternatingly between densely packed 4*h* layers (**Fig. 23A**).[164]

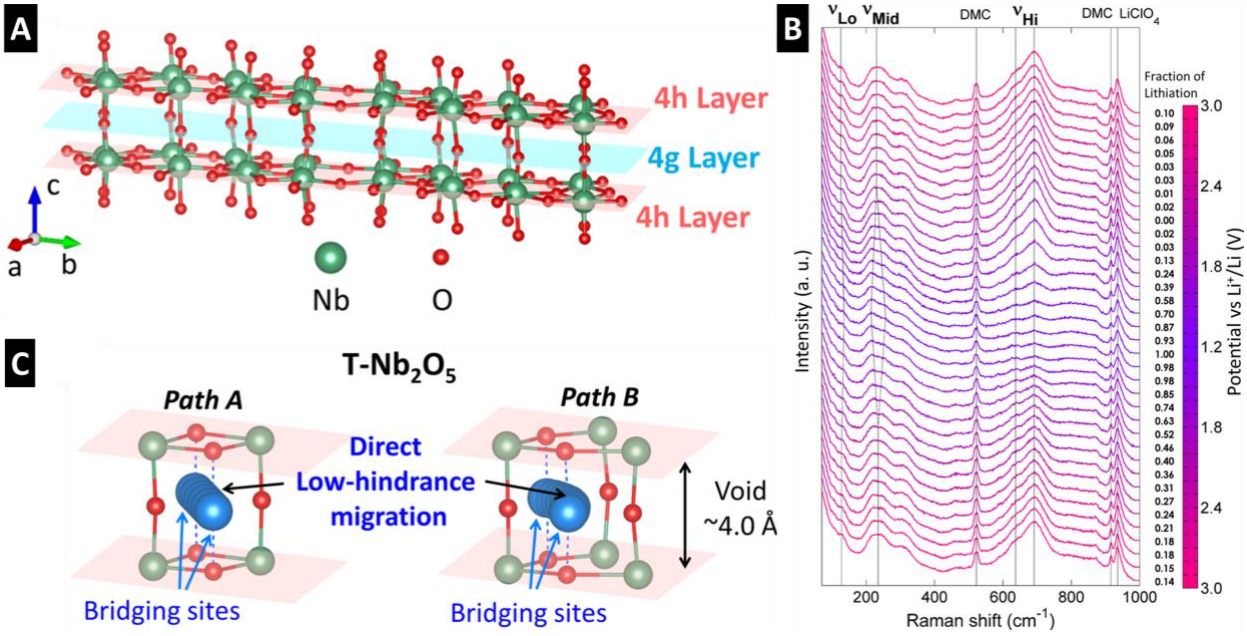

Figure 23: (A) Structural model of T-Nb_2O_5, highlighting densely packed 4*h* layers and loosely packed 4*g* layers. (B) Electrochemical operando Raman spectroscopy of a T-Nb_2O_5 thin film electrode between 3 V and 1.2 V vs. Li/Li^+, with Raman spectra in potential intervals of 0.1 V. (C) Proposed low-hindrance Li^+ diffusion paths between bridging sites. Panels adapted and reprinted from Ref. [164]. Copyright 2016 American Chemical Society.

Chen et al. employed electrochemical operando Raman spectroscopy and computed vibrational density of states (VDOS) for the proposed Li^+ transport path in T-Nb_2O_5 (**Fig. 23B**).[164] First, it was found that the intercalated Li^+ ions are located in bridging sites in between oxygens of the two neighboring 4h layers (O_{4h}) (**Fig. 23C**).[164] Depending on whether the O_{4h} is six- or sevenfold coordinated, Li^+ diffusion paths are categorized as path A or path B, respectively. The authors identified the structural features of the diffusion paths that led to the kinetically rapid, pseudocapacitive response of T-Nb_2O_5: both diffusion paths offer (i) direct, low-hindrance

diffusion between the bridging sites, (ii) show a large void size of 4 Å providing ample space for Li^+ transport, and (iii) exhibit no steric hindrance for Li^+ migration.[164]

These intrinsic structural features of T-Nb_2O_5 give rise to pseudocapacitive Li^+ storage at charging times up to about 60 seconds. The main kinetic limitation of T-Nb_2O_5 based electrodes is posed by its low electrical conductivity in the non-lithiated state. Strategies to provide sufficient electron transport at high rates include nanostructuring, integration into a conductive carbon network,[165–167] or the introduction of oxygen vacancies.[168]

4.1.3 Perovskite Oxides

Perovskites are mixed metal oxides with the structural formula ABO_3, where A is usually a lanthanide or an alkali earth metal and B is a transition metal (**Fig. 24A**). They have been primarily employed in energy conversion applications such as electrocatalysis[169] and solid oxide fuel cells.[170] The electrochemical energy storage properties of perovskites were first explored by Kudo et al. who reported the reduction of $Nd_{1-x}Sr_xCoO_3$ to the oxygen-deficient $Nd_{1-x}Sr_xCoO_{3-\delta}$, which was reversible in the range $0 \leq \delta \leq x/2$.[171] The authors hypothesized that charge storage was accomplished by oxygen intercalation from the alkaline electrolyte.[171]

Subsequent studies of the $SrRuO_3$ system in alkaline electrolyte gave an alternative explanation for the charge storage mechanism. It was hypothesized that protons migrated along the lattice oxygens via the Grotthuss mechanism, while redox was attributed to changes in the Ru valence, leading to the formation of $SrRuO_2OH$, $SrRuO_3$, and $SrRuO_3OH$.[172,173] The authors found capacitive behavior with a mostly rectangular cyclic voltammogram, yielding a maximum

capacitance of 160 F/g (53 mAh/g) for the A- and B-site doped $La_{0.2}Sr_{0.8}Mn_{0.2}Ru_{0.8}O_3$ at 20 mV/s.[172,173]

Many perovskites possess a wide range between oxygen-deficiencies and oxygen-excess. For example, $SrCoO_{3-\delta}$ can form ordered perovskite phases with different symmetries in a range between $2.29 < 3-\delta < 3$,[174] and $LaMnO_{3+\delta}$ accommodates both sub- and super-stoichiometric oxygen content, with $-0.25 < \delta < 0.25$.[175] This gave rise to a detailed study of the impact of oxygen vacancies in $LaMnO_{3+\delta}$ on the electrochemical charge storage properties in aqueous 1 M KOH.[175] Cyclic voltammograms showed a rectangular shape with a small, reversible peak around -0.4 V vs. Hg/HgO (**Fig. 24B**). The proposed reaction mechanism was the direct intercalation of oxygen anions from the electrolyte, oxidizing the Mn centers of the perovskite:[175]

$$La[Mn^{2+}_{2\delta}; Mn^{3+}_{1-2\delta}]O_{3-\delta} + 2\delta OH^- \leftrightarrow LaMn^{3+}O_3 + 2\delta e^- + \delta H_2O \quad (23)$$

$$LaMn^{3+}O_3 + 2\delta OH^- \leftrightarrow La[Mn^{4+}_{2\delta}; Mn^{3+}_{1-2\delta}]O_{3+\delta} + 2\delta e^- + \delta H_2O \quad (24)$$

The change of oxidation state of the Mn centers was confirmed by ex situ XPS, and accumulation of Mn^{4+} was found toward the surface of the particles during prolonged cycling due to the addition of oxygen anions from the electrolyte.[175] This was proposed to enhance the diffusion rate of oxygen along the surface and grain boundaries, causing the pseudocapacitive oxygen intercalation kinetics.[175] Assuming the accessible oxygen deficiency/excess range $\delta = 0.25$, the theoretical specific capacity of ca. 110 mAh/g can be calculated for the redox couple $LaMnO_{2.75}$ / $LaMnO_{3.25}$, which is below the maximum value of 610 F/g (203 mAh/g) reported in the study. Possible reasons for this discrepancy could be a wider accessible oxygen vacancy range and additional redox reactions beyond oxygen intercalation.

Oxygen intercalation was also hypothesized to be the charge storage mechanism in $SrCo_{0.9}Nb_{0.1}O_{3-\delta}$, with the subsequent oxidation of Co^{2+} to Co^{3+} and Co^{4+},[176] according to the same mechanism as in $LaMnO_3$. A capacitance of 400 F/g (78 mAh/g) was reported at 10 mV/s in aqueous KOH, and according to b-value analysis, the process was found to be kinetically surface controlled up to a scan rate of ca. 5 mV/s.[176] The same group also investigated the charge storage mechanism in reduced $PrBaMn_2O_{6-\delta}$, a layered double perovskite structure, in KOH electrolyte.[177] Using XANES, it was found that O^{2-} intercalation led to partial oxidation of Mn^{2+} to Mn^{4+} in the charged electrode (**Fig. 24C-D**).[177] The authors reported a capacitance of 1035 F/g (173 mAh/g) in aqueous 6 M KOH at a specific current of 1 A/g.[177] The introduction of oxygen vacancies in the structure led to the development of a pseudocapacitive response, with surface-controlled kinetics up to a scan rate of ca. 20 mV/s.[177] DFT calculations predicted that the layered double perovskite structure benefited both the oxygen vacancy concentration and O^{2-} diffusion rate, which could guide further materials design strategies for pseudocapacitive perovskite electrodes.[177] From a fundamental point of view, the mechanism of pseudocapacitive anion intercalation in perovskite oxides is very intriguing and warrants further exploration. Widening the accessible oxygen deficiency/excess range will be crucial to further expand the capacity of the materials.

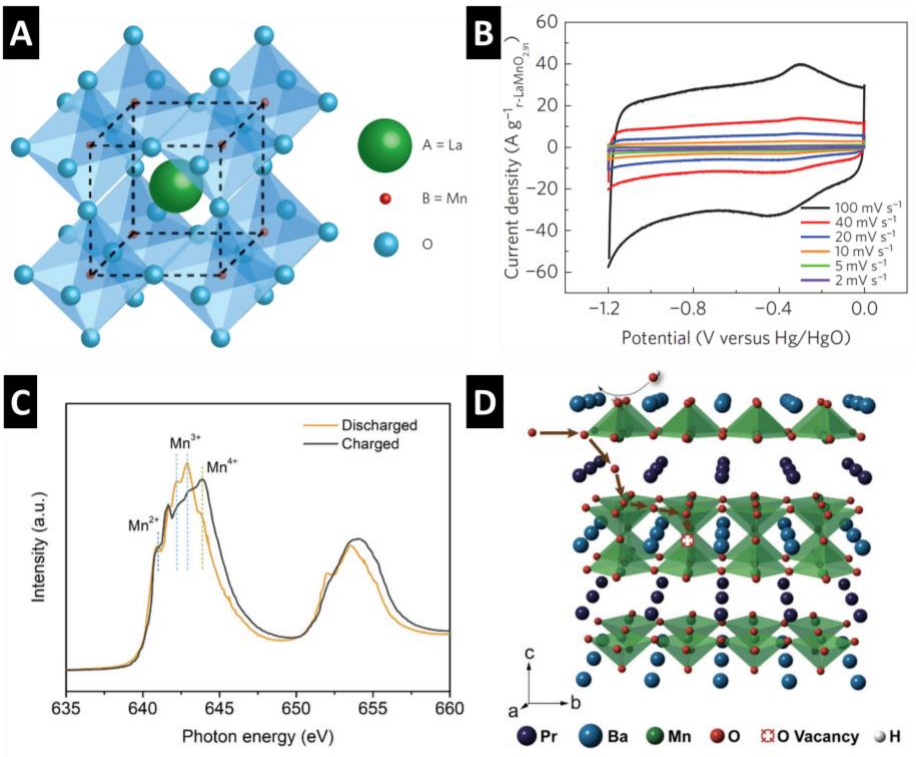

Figure 24: (A) Crystal structure of perovskite $LaMnO_3$, and (B) cyclic voltammograms of oxygen-deficient $LaMnO_{2.91}$ in 1 M KOH electrolyte. Reproduced with permission from Ref. [175]. Copyright 2014 Springer Nature. (C) XANES of charged and discharged $PrBaMn_2O_{6-\delta}$ showing a shift in the Mn oxidation state. (D) Proposed intercalation mechanism of O^{2-} anions in the $PrBaMn_2O_{6-\delta}$ structure: the occupation of oxygen vacancy sites and diffusion along edges of tetrahedra. Reproduced with permission from Ref. [177]. Copyright 2018 John Wiley and Sons.

4.2 Two-Dimensional Transition Metal Carbides/Nitrides/Carbonitrides (MXenes)

In 2011, MXenes were introduced as a new class of two-dimensional transition metal carbides, carbonitrides, or nitrides with the general structural formula $M_{n+1}X_nT_x$ where M is an early transition metal, X is carbon and/or nitrogen, T_x is the surface termination (mostly -OH, -O, or -F), and n is usually an integer between one and three (the first structure with n = 4 was recently reported).[45,178–181] They are most commonly synthesized by etching of MAX phases, a family of ternary carbides and/or nitrides, where layers of A atoms (group 13 or 14 elements) are selectively removed either in hydrofluoric acid or in hydrochloric acid with LiF (**Fig. 25A**).[182,183] A new approach was recently introduced by Li et al. to synthesize MXenes via immersion of the MAX precursor in a Lewis acid molten salt at elevated temperatures.[184] MXenes exhibit a hexagonal close-packed structure: M atoms are stacked in either ABABAB ordering in M_2X, or in ABCABC ordering in M_3X_2 and M_4X_3 phases, while X atoms occupy the octahedral interstitial sites.[179] By far, the most studied MXene phase is $Ti_3C_2T_x$, which has been used for many electrochemical applications such as Li-ion batteries,[185] electrical double-layer capacitors,[186] asymmetric hybrid supercapacitors,[187] capacitive deionization,[188] and electrocatalysis[189].

MXenes exhibit strong covalent bonds between M and X atoms and weaker hydrogen bonding or Van der Waals interactions between the two-dimensional sheets (dependent on the interlayer chemistry).[190] They can be easily delaminated using a variety of methods, such as sonication.[191] The electrochemical properties of MXenes are governed by the insertion behavior of ions between the sheets, which is why it is critical to understand the impact of surface terminations or interlayer molecules like water. The unique structural features of MXenes relevant for EES include (i) abundant interlayer ion diffusion paths, (ii) interlayer ion storage sites,

and (iii) an electronically conductive carbide/nitride core. These make MXenes important candidates for intrinsically pseudocapacitive energy storage materials. Owing to the structurally flexible interlayer, a large variety of ions can potentially be inserted between MXene sheets, and different charge storage capacities and dynamics can be observed depending on the interactions of electrolyte components and MXene interlayer chemistry. An essential question that needs to be answered is the charge storage mechanism of MXenes, which could be of electrostatic or Faradaic nature, or a combination of both (**Fig. 25B**).[192]

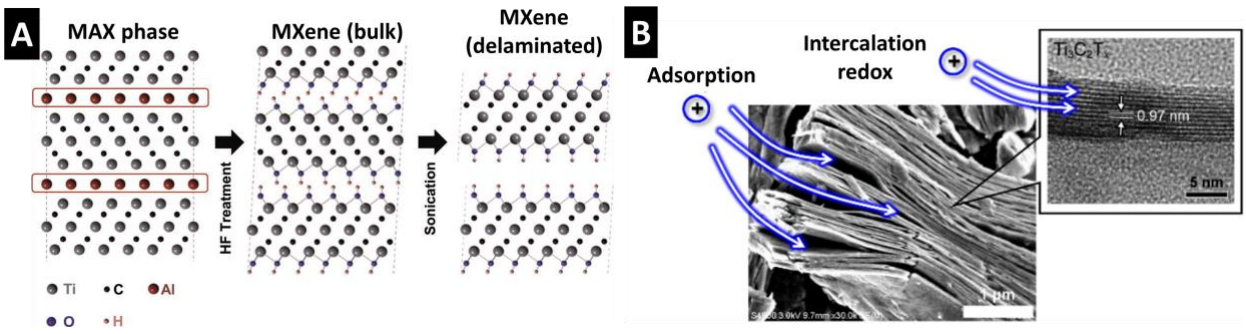

Figure 25: (A) Schematic illustration of MXene synthesis and delamination. Adapted with permission from Ref. [45]. Copyright 2011 John Wiley and Sons. (B) Scanning and transmission electron micrographs of delaminated $Ti_3C_2T_x$ MXene, indicating possible ion adsorption or ion intercalation as charge storage mechanisms. Adapted from Refs. [192]. Copyright 2018 American Chemical Society.

In aqueous electrolytes, MXenes show mostly rectangular, capacitor-like cyclic voltammograms, but different charge storage mechanisms have been observed in neutral, basic, and acidic electrolytes. Upon immersion in neutral and basic electrolytes, without applying a potential, a large number of solvated cations of various charges and sizes can be inserted between the $Ti_3C_2T_x$ MXene layers (such as Li^+, Na^+, K^+, NH_4^+, Mg^{2+}, or Al^{3+}), as shown by Lukatskaya et al. using in situ XRD.[193] Electrochemical cycling led to capacitances around 80 F/g in 1 M K_2SO_4 (ca. 17 mAh/g) at a rate of 2 mV/s.[193] Similarly, Levi et al. showed the uptake of solvated ions in neutral electrolytes using in situ electrochemical quartz-crystal admittance.[68] They further proposed the concept of shallow and deep adsorption sites in multilayered $Ti_3C_2T_x$ MXenes. Shallow adsorption sites were proposed to exist at the edges of multilayered MXene particles, accessible for cation insertion over a wide range of charging rates that led to a capacitive electrochemical response.[68] Cation insertion into deep adsorption sites in the particle interior was diffusion-controlled with low reversibility.[68] Okubo et al. analyzed the charge storage mechanism of Ti_2CT_x MXene in aqueous 1 M Li_2SO_4 by ex situ XAS.[192] This showed a small shift of the Ti oxidation state in the potential range of -0.05 V and -0.45 V vs. Ag/AgCl, in agreement with the electrochemically determined charge of 20 mAh/g (0.05 electrons per Ti).[192] In neutral electrolytes, MXenes show competing EDL and pseudocapacitive charge storage contributions due to the strong interaction between the inserted cations and water solvent molecules under confinement, as supported by recent DFT work and discussed later in this chapter.[71]

In acidic electrolytes, significantly higher capacities have been reported. Ghidiu et al. demonstrated that 5 µm thick, free-standing $Ti_3C_2T_x$ clay electrodes with mixed -F and -O terminations could exhibit up to 245 F/g (37 mAh/g) at 2 mV/s.[182] Dall'Agnese et al. reported a

strong dependency of the observed capacity in 1 M H_2SO_4 on the surface termination of $Ti_3C_2T_x$ MXenes, with oxygen terminations showing 4-fold increased capacity compared to fluorine terminations.[194] The authors hypothesized that redox reactions of protons with oxygen-containing surface terminations cause a pseudocapacitive current, as further indicated by a pair of broad redox peaks at -0.2 V and -0.1 V vs. Ag/AgCl.[194]

This hypothesis was confirmed in studies by Lukatskaya et al.[195] and Hu et al.,[196] who demonstrated that (i) charge storage was accomplished by redox reactions and (ii) protons reacted with oxygen terminations. In situ XANES was used to measure the change of the Ti oxidation state in $Ti_3C_2T_x$ MXene cycled in aqueous 1 M H_2SO_4 (**Fig. 26A**).[195] The average Ti oxidation state decreased from 2.43 (at +0.35 V vs. Ag/AgCl) to 2.33 (at -0.35 V vs. Ag/AgCl).[195] This corresponds to 0.3 electron transfers per $Ti_3C_2T_x$ (40 mAh/g), in agreement with the experimental capacity of ca. 45 mAh/g, and confirmed that charge storage was predominantly caused by pseudocapacitive proton intercalation.[195] The reaction mechanism was revealed by in situ Raman spectroscopy (**Fig. 26B**).[196] In $Ti_3C_2T_x$ MXene, intercalated protons bind to the terminal Ti=O bond to form Ti-OH, resulting in a shift of the Raman mode originally at 726 cm^{-1}.[196] No changes in the Raman spectrum were found for neutral aqueous $MgSO_4$ and $(NH_4)_2SO_4$ electrolytes, suggesting solely double-layer contribution.[196]

In an effort to close the gap of the measured capacity to the theoretical capacity of ca. 170 mAh/g (assuming full protonation of all available oxygen terminations) for $Ti_3C_2T_x$ MXenes, Lukatskaya et al. prepared 90 nm thin films and hydrogel electrodes and expanded the probed potential window to 1 V.[15] Cyclic voltammograms in aqueous 3 M H_2SO_4 showed a pseudocapacitive response, with a rectangular background and a highly reversible pair of redox

peaks that only exhibited a peak separation of about 50 mV at a high rate of 1 V/s with a maximum capacity of 106 mAh/g (**Fig. 26C**).[15] The high rate capability, challenging those of double-layer capacitors, underlines the suitability of the MXene structure to accommodate high rate pseudocapacitive proton intercalation, which is aided by interlayer water providing proton diffusion paths and the carbide core ensuring sufficient electron transport (**Fig. 26D**).[15]

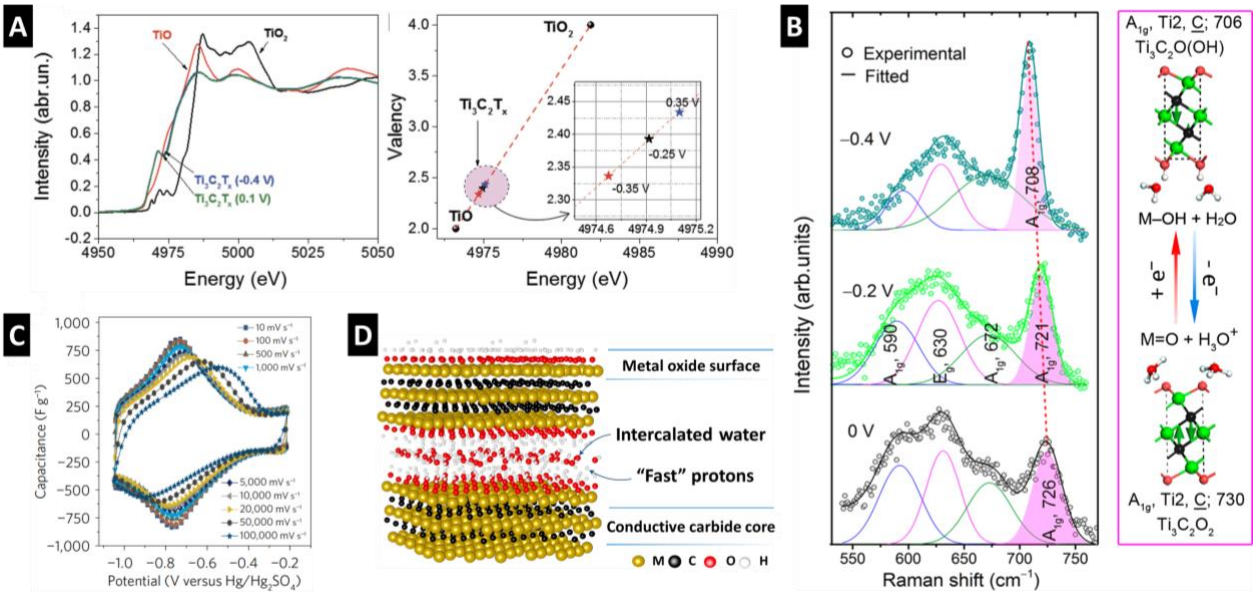

Figure 26: (A) Ti K-edge XANES spectra for $Ti_3C_2T_x$ MXene at different potentials and corresponding average Ti oxidation state determined from the Ti K-edge energy shift. Reproduced with permission from Ref. [195]. Copyright 2015 John Wiley and Sons (B) In situ Raman spectra of $Ti_3C_2T_x$ at 0 V, -0.2 V, and -0.4 V vs. Ag/AgCl in aqueous 1 M H_2SO_4 and proposed reaction mechanism. Reproduced from Ref. [196]. Copyright 2016 American Chemical Society. (C) Cyclic voltammograms of 90 nm-thick $Ti_3C_2T_x$ film in 3 M H_2SO_4 electrolyte at sweep rates between 10 mV/s and 10 V/s. (D) Schematic illustration of the MXene structure, proton transport paths due to intercalated water, and abundant electron supply due to the conductive carbide core. Adapted with permission from Ref. [15]. Copyright 2017 Springer Nature.

Recent theoretical work from Sun et al. analyzed the proton mobility in hydrated $Ti_3C_2O_2$ MXene via first-principles molecular dynamics.[197] They confirmed redox reactions between protons from interlayer water with -O terminations and found frequent in-water proton transport events. With an increasing number of interlayer water layers, the proton mobility increased, but the redox rate decreased. The authors concluded that proton diffusion within the MXene interlayer was not the likely rate-limiting step for proton storage in MXenes, instead it was the transfer of protons from the bulk electrolyte to the interlayer.[197]

Despite significant advances in increasing the specific capacity of MXenes in acidic electrolytes, the small potential window of aqueous electrolytes severely limits the energy density of resulting devices. Furthermore, acidic electrolytes present challenges with self-discharge and the hydrogen evolution reaction. Research on proton intercalation brings forward significant fundamental insights into the structure and electrochemical properties of MXenes and proton transport under nanoconfinement. At the same time, many research efforts are now directed towards the use of organic electrolytes that enable larger operating voltage.

In non-aqueous alkali-ion containing electrolytes, MXenes derived from traditional etching methods generally show distorted rectangular cyclic voltammograms over a wide potential range that can contain small pairs of redox peaks, and the current response is largely attributed to pseudocapacitive intercalation reactions.[198–200] For Li^+ intercalation from organic electrolytes, Xie et al. found that -O terminated MXenes exhibit the highest lithiation capacity and mobility.[201] The measured lithiation capacity of $Ti_3C_2O_2$ MXene up to a potential of 0.51 V vs. Li/Li^+ was 262 mAh/g, corresponding to the formation of $Ti_3C_2O_2Li_2$.[201] In situ XANES showed that the lithiation was accompanied by reduction of Ti.[201] At potentials below 0.5 V vs. Li/Li^+, additional

charge storage did not affect the titanium oxidation state but was hypothesized to be accomplished via the adsorption of an additional layer of Li,[201] or, alternatively, by decomposition of the electrolyte. Wang et al. demonstrated that electrolyte composition has a large impact on the lithiation capacity.[202] The authors found that carbonate-based electrolyte solvents enable complete desolvation of Li^+ before intercalation, which, in turn, increased the number of intercalated Li^+ (0.93 Li^+ per Ti_3C_2), leading to a higher capacity as compared to nitrile- (0.37 Li^+ per Ti_3C_2) or sulfoxide-based (0.46 Li^+ per Ti_3C_2) solvents (**Fig. 27A**).[202] In a propylene carbonate electrolyte, Ti_3C_2 MXene electrodes showed pseudocapacitive Li^+ intercalation with surface-controlled kinetics ($b \approx 1$) for sweep rates between 2 mV/s and 1 V/s in a 2.4 V potential window.[202]

$Ti_3C_2T_x$ MXenes synthesized via the Lewis acid molten salt approach from a Ti_3SiC_2 MAX precursor show predominantly -O terminations, in absence of -OH and -F terminations.[184] Cyclic voltammograms measured in organic 1 M $LiPF_6$ in EC/DMC electrolyte exhibit a rectangular shape between 0.2 – 3.0 V vs. Li/Li^+, attributed to pseudocapacitive lithium intercalation behavior in a large potential window (**Fig. 27B**).[184] During cycling, the interlayer spacing did not expand significantly as shown by in situ XRD measurements (**Fig. 27C**).[184] The lack of interlayer spacing change as a function of potential was attributed to the de/intercalation of desolvated Li. The specific capacity reached up to 205 mAh/g (1.29 Li^+ per Ti_3C_2), which is among the highest capacities of any MXene showing pseudocapacitive intercalation behavior to date.[184] The study highlights the importance of MXene surface terminations on the electrochemical performance and the concept of the Lewis acid molten salt synthesis of MXenes.

Na^+ intercalation in Ti_2CT_x MXene nanosheets was evaluated by Wang et al. in organic 1 M $NaPF_6$ in ethylene carbonate (EC) / diethyl carbonate (DEC) electrolyte.[203] They reported pseudocapacitive sodiation with a mostly rectangular cyclic voltammogram between 3.0 V and 0.1 V vs. Na/Na^+ after the first cycle that also contained a small pair of redox peaks at around 2 V, yielding a specific capacity up to 175 mAh/g.[203] In the first cycle, ex situ XRD showed that the interlayer expands from 0.8 nm to 1.0 nm, and during subsequent cycling, the interlayer distance stays relatively constant around 1.0 nm, indicating that some Na^+ likely remains in the interlayer, functioning as pillars (**Fig. 27D**).[203] Ex situ XPS showed a concomitant reduction of Ti, suggesting that charge storage was accomplished by Faradaic intercalation.[203] At higher rates, however, significant drops in the capacity indicated kinetic limitations. In a follow-up study by Kajiyama et al., ^{23}Na magic-angle spinning NMR and DFT were used to confirm the pillaring effect during the first sodiation cycle of $Ti_3C_2T_x$.[199] The authors observed that both Na^+, as well as some solvent molecules, were inserted into the interlayer space, which led to swelling of the interlayer and aided subsequent (de-)intercalation of desolvated Na^+.[199]

Ion intercalation from non-aqueous electrolytes into MXenes shows unique electrochemical characteristics. The intercalation process appears to span a wide potential range, up to 3V. This is in contrast to many transition metal oxides, where ion insertion occurs within a narrow window, typically 1 - 2 V. This makes the designation of MXenes as anodes or cathodes less straightforward, and influences the selection of counter electrodes in devices.

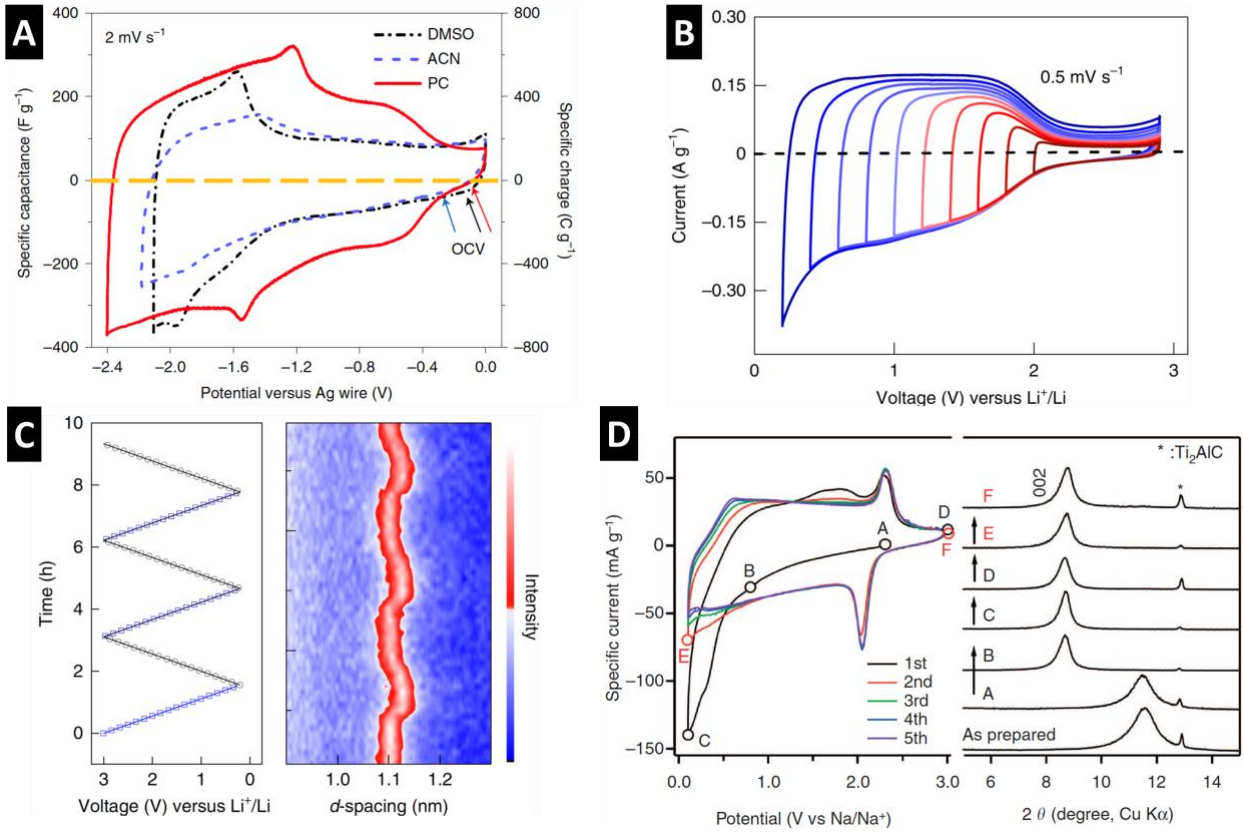

Figure 27: (A) Cyclic voltammograms of macroporous $Ti_3C_2T_x$ electrodes in 1 M LiTFSI in different organic solvents. Reproduced with permission from Ref. [202]. Copyright 2019 Springer Nature. (B) Cyclic voltammograms at 0.5 mV/s of molten salt synthesized $Ti_3C_2T_x$ in 1 M $LiPF_6$ in EC/DMC electrolyte and (C) corresponding interlayer spacing obtained by in situ XRD. Reproduced with permission from Ref. [184]. Copyright 2020 Springer Nature. (D) Cyclic voltammograms of the first five (de-)sodiation cycles of $Ti_3C_2T_x$ in 1 M $NaPF_6$ in EC/DEC electrolyte and corresponding ex situ XRD. Reproduced with permission from Ref. [203].

Charge storage in MXenes is closely related to their electronic structure and electronic density of states (DOS) at the Fermi level, so DFT is a powerful tool to study their pseudocapacitive behavior. For example, Ji et al. determined the pseudocapacitance of Ti_2CT_2 (T = O, F) MXene for sodium-ion storage from the DOS and work function at different Na^+ concentrations on the surface: 292 F/g for O-termination and 252 F/g for F-termination (**Fig. 28A**).[204] Using a similar approach, Wang et al. predicted the pseudocapacitance of $Ti_3C_2T_2$ (T = O, S) MXenes in an acidic electrolyte: 213 F/g and 288 F/g for $Ti_3C_2O_2$ and $Ti_3C_2S_2$, respectively.[205] This suggests that the S termination can enhance the energy storage of $Ti_3C_2T_2$ MXene (**Fig. 28B**). Furthermore, Yang et al. used a combination of XAS and DFT with a variety of Ti-containing MXenes to find a reduced Bader charge of surface Ti-atoms of 2.35 e^- compared to 2.5-2.6 e^- for sub-surface Ti-atoms. This implies that the electronic impact of the surface terminations T_x is fully compensated by the surface metal atom and has little impact on sub-surface metal atoms.[206]

To include the effect of a realistic electrochemical environment, Zhan et al. proposed a model based on ensemble-average free energy and DFT-continuum simulation at a constant potential (**Fig. 28C**), to capture the contribution of EDL formation during the surface redox process on a MXene surface.[207] A voltage-dependent redox/EDL co-charging process was found for $Ti_3C_2T_x$ (T = O, OH) in aqueous H_2SO_4 electrolyte (**Fig. 28D**). The calculated capacitance (~231 F/g) and Ti oxidation state showed good agreement with experimental results. Computational screening of over 30 MXenes was conducted based on this model of pseudocapacitance in aqueous H_2SO_4. The reliability of this model was confirmed by comparing the predicted capacitance of several MXenes with earlier reported experimental data. Nitride-based MXenes were predicted to have higher capacitance than carbide ones. In addition, the hydrogen adsorption energy (ΔG_H) and the shift

in the potential of zero charge (ΔV_{pzc}) were found to be good descriptors to determine the pseudocapacitance of MXene in aqueous H_2SO_4 (**Fig. 28E**): a MXene with larger ΔG_H and lower ΔV_{pzc} was predicted to show promising pseudocapacitive behavior in aqueous H_2SO_4.[208]

MXenes also exhibit pseudocapacitance in neutral aqueous electrolyte. However, the conventional EDL model failed to explain the decreasing capacitance with increasing cation size from Li^+ to Rb^+. Recently, this phenomenon was successfully explained by Sugahara et al. (**Fig. 28F**), using a newly developed hybrid quantum-continuum simulation method based on the reference-interaction-site-model (RISM).[209] The capacitance from Li^+ insertion into MXene (> 100 F/g) was attributed to the negative dielectric constant of water and the strong hydration of Li^+ under nanoconfinement. This finding suggested the importance of careful treatment of the solvent effect when modeling intercalation pseudocapacitance. Relying on the advantage of DFT-RISM, a recent study by Ando et al. studied cation insertion in MXene in the presence of water solvent and proposed a physical interpretation of MXene pseudocapacitance in neutral aqueous electrolytes. It was found that the co-insertion of a full hydration shell can inhibit orbital coupling between the MXene and the inserted cation.[71] For a solvated cation adsorption on a MXene surface, the resulting complete charge separation leads to the formation of an electrical double layer in the MXene interlayer space. In the case of partially desolvated cations, however, it is found that charge redistribution and orbital coupling can significantly enhance the pseudocapacitive contribution in MXene electrodes due to the close contact of MXene-cation.[71]

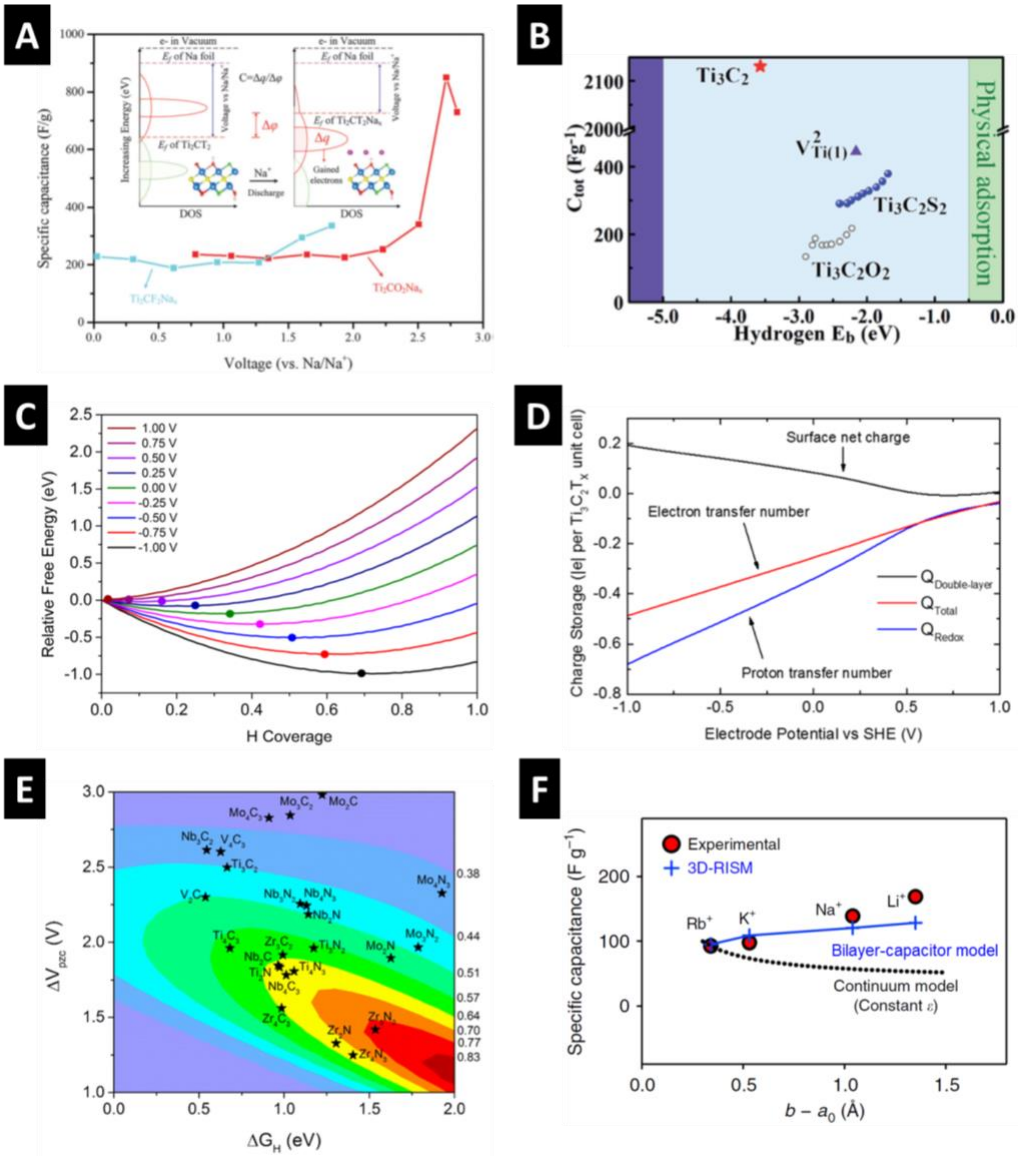

Figure 28: (A) Simulated specific capacitance of Ti_2CO_2 and Ti_2CF_2 nanosheets (insets shows the theoretical scheme). Reprinted from Ref. [204] with permission of The Royal Society of Chemistry; permission conveyed through Copyright Clearance Center, Inc. (B) Total capacitance vs. H binding energy for different systems: circles and blue represent varying H coverages; triangle represents $Ti_3C_2S_2$ with two Ti(1) vacancies and full H coverage. Reprinted from Ref. [205] with permission of The Royal Society of Chemistry; permission conveyed through Copyright Clearance Center, Inc. (C) Gibbs free energy of $Ti_3C_2T_x$ (T = O, OH) in an acidic electrolyte as a function of H coverage at

different electrode potentials, ϕ, relative to SHE. The average minimum on each curve is indicated by a dot. (D) Faradaic charge (blue, due to proton transfer), EDL charge (black, due to surface net charge), and total charge (red, net electron transfer number) stored at different electrode potentials. Reprinted from Ref. [207]. Copyright 2018 American Chemical Society. (E) Charge storage per formula unit (contour line values) vs. the shift in the potential at the point of zero charge (ΔV_{PZC}) and hydrogen adsorption free energy (ΔG_H). Reprinted from Ref. [208]. Copyright 2019 American Chemical Society. (F) Dependence of the capacitance on the ion-MXene distance ($b - a_0$): Comparison of the 3D-RISM model and the continuum model with the experiment. Reprinted with permission from Ref. [209].

Fundamental understanding of charge storage in MXenes will continue as a promising research direction in the near future. MXenes provide a materials chemistry playground for understanding energy storage under confinement. Development of new synthesis routes, as exemplified by the molten salt technique[184], highlight the great opportunity to tune MXene surface terminations which play a significant role in determining the charge storage mechanism. The interactions between solvated or partially solvated cations and the MXene host under confinement will provide deep physical insight into the nature of electrochemical energy storage. From an application standpoint, it would lead to the prediction of promising cation and solvent combinations for maximizing the pseudocapacitive response. For instance, the solvent could be used to modulate cation adsorption onto MXene via the strength of the orbital coupling (MXene-cation distance). In addition, modulation of the interlayer space is another way to enhance the electronic coupling between the intercalated cation and MXene surface.

4.3 Transition Metal Dichalcogenides

Recent studies of nanostructured and exfoliated transition metal dichalcogenides have shown the possibility of extrinsic pseudocapacitance in this class of materials.[210] MoS_2 is one sulfide material of great interest for EES due to its layered structure and the change in electronic properties from the semi-conductive 2H-phase to the metallic 1T phase after electrochemical ion intercalation.[210] Mesoporous MoS_2 displayed pseudocapacitive charge storage behavior during Li^+ intercalation, with a specific capacity of 140 mAh/g for 20 s charge / discharge times (80 % of theoretical capacity).[210] Operando XRD studies revealed that the pseudocapacitive nature of the nanocrystalline MoS_2 was due to the suppression of a phase transition from 1T MoS_2 to triclinic Li_xMoS_2.[211] Mesoporous films are assemblies of nanostructured materials that provide short solid-state diffusion distances as well as electronic conduction through interconnected grains and high porosity for electrolyte accessibility.[82,212,213] Suppression of the phase transition was also observed for Li^+ intercalation into nanostructured TiS_2 using in situ synchrotron XRD.[214] The 2D morphology of the nanostructured TiS_2 led to highly reversible cyclic voltammograms with limited separation between the redox peaks upon fast charging / discharging and largely surface-controlled current contributions.

Many studies on exfoliated MoS_2 flakes show capacitive electrochemical responses, such as rectangular cyclic voltammograms, in various aqueous electrolytes.[215–219] However, the charge storage mechanism in these materials remains a subject of debate. It is often argued that pseudocapacitive intercalation of cations between the MoS_2 sheets is accompanied by redox reactions. However, with 1T phase nanosheets of MoS_2 exhibiting metallic conductivity, an alternative explanation for the large capacitances observed in many studies could be electrical

double-layer formation on the surface and within the MoS_2 interlayer space, a mechanism recently proposed by Costentin, et al.[63] Further studies employing in situ or operando methods to analyze the chemical signature of MoS_2 during cycling are necessary to determine the mechanism of charge storage of exfoliated MoS_2 in aqueous electrolytes.

4.4 Pseudocapacitive Carbon-Based Materials

Carbon-based materials that store electrical charge via the formation of the electrical double-layer are to-date the most commercially relevant materials for electrochemical capacitors. A critical research direction for these materials is to enhance their capacitance in order to increase the energy density of electrochemical capacitors.[220] This can be achieved by introducing redox-active centers such as functional groups,[221] or via chemical doping[222] and addition of aromatics.[223]

Redox-active functional groups can be added to porous carbon scaffolds through various chemical activation methods.[224] Chen et al. used an H_3PO_4 chemical activation method of the biomaterial waste, cicada slough, to produce a porous carbon with a large specific surface area (1945 m^2/g) and high oxygen / phosphorus co-doping ratio of 18 mass%.[224] The co-doping led to the development of broad redox peaks assigned to a pseudocapacitive charge storage mechanism and capacity of 83 mAh/g in both 1 M H_2SO_4 and 6 M KOH aqueous electrolytes. Yang et al. investigated a low-temperature pyrolysis method to achieve high nitrogen contents of 22 %,[225] which led to a capacitance of 776 F/g at 1 A/g.

A separate strategy to enhance the capacity of carbon-based materials is to introduce redox-active aromatic molecules. Aromatic molecules containing conjugated π-electrons can adsorb onto the surface of graphitic carbon through π-π interactions.[223] Le Comte et al. investigated porous carbon with added phenanthrenequinone, an aromatic organic compound containing redox-active ketone moieties.[226] While the adsorbed quinone led to reversible redox peaks, the increased capacity faded within a few hundred cycles, likely due to poor adhesion of the organic molecules. They tested this hypothesis by grafting the quinone to the porous carbon scaffold via covalent bonding. The capacity retention of the grafted materials was much higher.

Other redox-active organic compounds such as catechols[227] and phenyldiamines[228] can also be grafted onto porous carbon scaffolds, highlighting the large composition space possible to increase charge storage in porous carbons.

Zhao et al. used a combined computational and experimental approach to understand the pseudocapacitive mechanism of three types of aromatics adsorbed onto the surface of graphene.[223] As shown in **Fig. 29A**, two different aminophenol (AP) isomers give different electrochemical responses, with 4-AP yielding ~ 30% increase in capacitance compared to the 2-AP. Energy level diagrams (**Fig. 29B**) were calculated to elucidate these electrochemical differences. They showed that 4-AP has a shift in the highest occupied molecular orbital (HOMO) energy level of +0.4 eV compared to 2-AP. The energy of the HOMO reflects the ability for the molecule to oxidize and donate an electron to the graphene surface, and a higher E_{HOMO} reflects a tendency to more easily donate an electron.[223] Interestingly, this correlation between high E_{HOMO} and higher capacitance was confirmed with both naphthalene diamine and dianiline isomers. A higher E_{HOMO} leads to higher pseudocapacitance because it reduced the energy barrier for electron transfer to graphene, promoting the Faradaic reaction of the amino-functional groups. Overall, this experimental and computational approach is necessary to guide the field of pseudocapacitive charge storage in carbon-based materials.

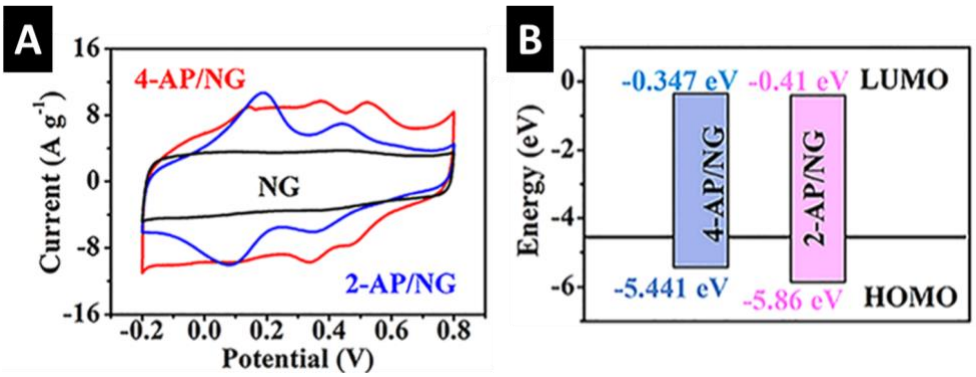

Figure 29: (A) Cyclic voltammograms of nitrogen-doped graphene (NG), 4-aminophenol (4-AP)/NG, and 2-aminophenol (2-AP/NG) electrodes at 10 mV/s. The addition of adsorbed aromatic organics leads to redox peaks and increased capacity. (B) Energy levels of the HOMO / LUMO. Adapted from Ref. [223]. Copyright 2019 American Chemical Society.

4.5 Metal-Organic Frameworks and Related Materials

Metal-organic frameworks (MOFs) are highly porous materials comprised of inorganic metal centers connected via organic linkers.[229] These materials are significant for intrinsically pseudocapacitive charge storage because they are highly tunable, can contain redox-active moieties, and can exhibit good electronic and fast ionic conduction.[230] To introduce pseudocapacitive charge storage into MOFs, recent work has focused on tuning the composition to introduce redox-active centers and improve the electrical conductivity.[231–233]

The use of hexaaminobenzene as the organic linker (**Fig. 30A**) led to a robust, conductive two-dimensional copper-based MOF that could be pressed into pellet electrodes with minimal conductive additive (5 mass%) and exhibited high areal and volumetric capacities.[232] The combination of electronic and ionic conductivity in this material is highlighted by its rate capability, retaining about 70 % of its capacity and a symmetrical voltammetric response after

increasing the scan rate from 1 mV/s to 100 mV/s (**Fig. 30B**). Meanwhile, the open, two-dimensional framework led to stable cycling in the aqueous KOH electrolyte, with ca. 90 % retention after 12,000 cycles at 10 A/g.

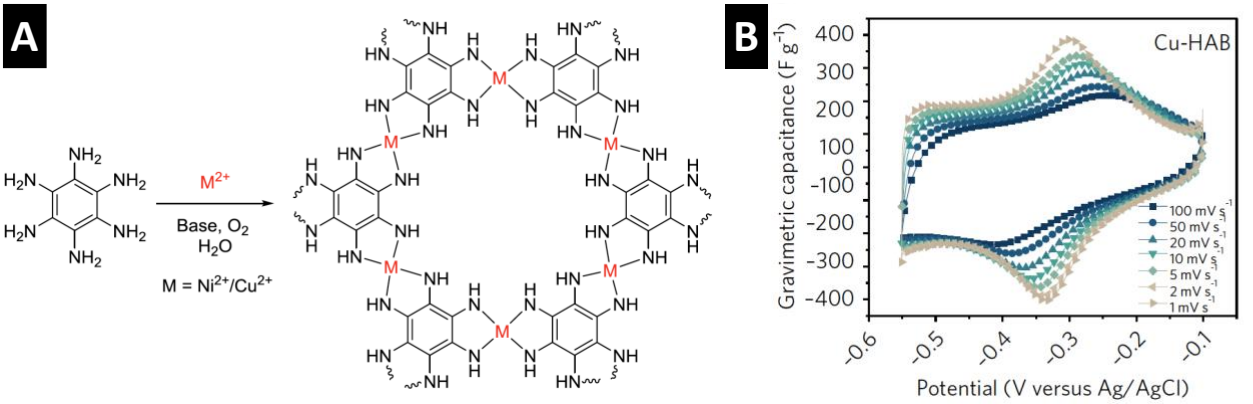

Figure 30: (A) Schematic of the synthesis of metal hexaaminobenzene metal-organic frameworks (M-HAB MOF, where M = Ni^{2+}, Cu^{2+}). (B) Cyclic voltammograms of Cu-HAB MOF in 1 M KOH electrolyte. Reproduced with permission from Ref. [232]. Copyright 2018 Springer Nature.

Prussian blues, with typical formula $A_xPR(CN)_6{\cdot}nH_2O$ (*A* = alkali cation, *P* = transition metal, RCN_6 = hexacyanometallate) are related framework materials with large channels available for ion insertion.[234] Recently, a defective Prussian blue analog showed fast proton insertion with mirror-image CVs, surface-controlled kinetics up to 10 mV/s, and a maximum capacity of 65 mAh/g. Operando XRD revealed a solid solution insertion mechanism with a 2% volume change. These features are indicative of an intercalation pseudocapacitance mechanism. The fast energy storage kinetics were attributed to a Grotthuss proton transport mechanism involving lattice water.[235] The results highlight the great potential for designing fluid-like transport in 3D frameworks.

The advantage of MOFs and related materials is that they are in effect "materials by design," and tuning their composition to introduce redox-active sites offers a method to increase their capacity. MOFs can also serve as synthetic templates to produce highly porous transition metal compounds such as CoS_2,[236] leading to pseudocapacitive charge storage. Overall, MOFs are a new class of materials with open frameworks and compositional freedom to enable pseudocapacitive charge storage.

4.6 Nanostructuring to Achieve Pseudocapacitance

Extrinsic pseudocapacitance describes materials that exhibit pseudocapacitive electrochemical features when in nanoscale form.[25] These are typically those materials that can undergo Faradaic charge storage via ion insertion. A prominent example of this phenomenon is the electrochemical behavior of the LIB cathode material, $LiCoO_2$, when its particle size decreases below 20 nm.[61] While the lithiation reaction occurs with a relatively flat potential at about 3.9 V vs. Li/Li^+ in micron-size $LiCoO_2$, an increasingly linear profile was observed for particle sizes below 17 nm, with pseudocapacitive behavior for 6 nm particles (**Fig. 31A**) and improved rate capability. The emergence of pseudocapacitive electrochemical features upon nanostructuring was hypothesized to be due to the increased contribution of near-surface Li^+ storage sites, which had more variation in site energy than those in the bulk (**Fig. 31B**).[61] Similarly, nanostructuring of other materials such as V_2O_5,[47,237,238] VO_2,[239] TiO_2,[240] or Li_3VO_4[241] led to a transition to pseudocapacitive lithium intercalation behavior. The introduction of defects has also been shown to induce more capacitive electrochemical behavior, as in olivine $LiFePO_4$ powders of several hundreds of nanometers.[242]

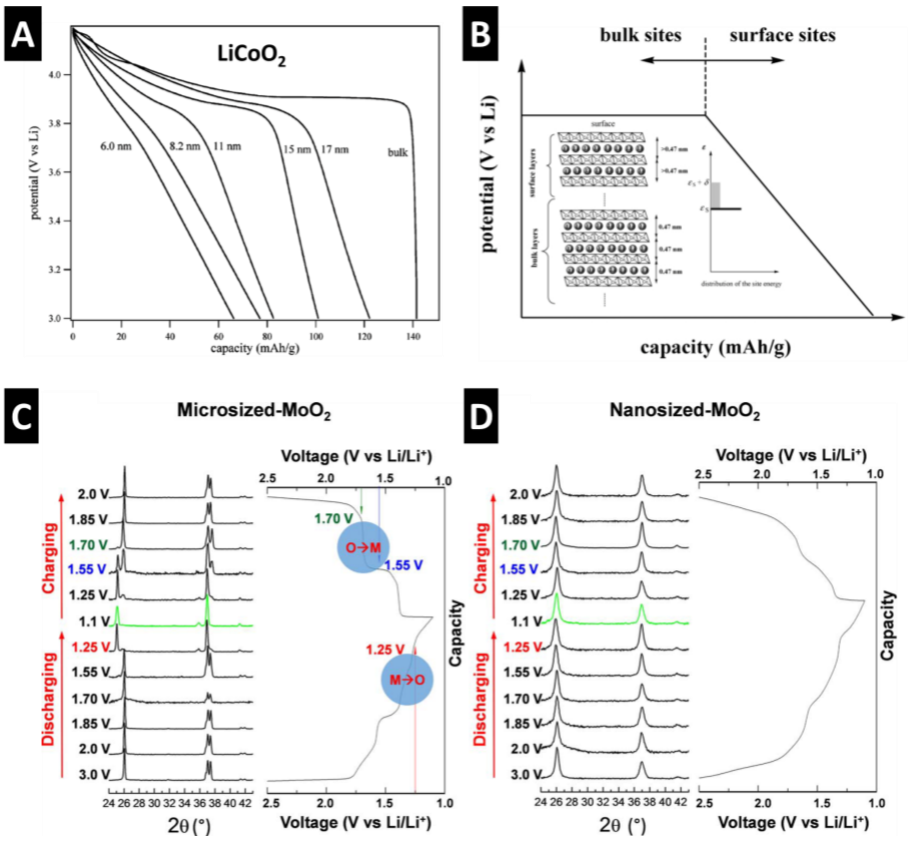

Figure 31: (A) Galvanostatic curves for Li^+ intercalation into $LiCoO_2$ with different particle sizes in a non-aqueous Li^+ electrolyte. (B) Expected galvanostatic profiles for Li^+ intercalation into bulk vs. near-surface sites, where surface disorder leads to the dispersion of site energies and thus a sloping Li^+ intercalation profile. Adapted from Ref. [61]. Copyright 2007 American Chemical Society. Ex situ XRD patterns for Li^+ intercalation into (C) micron-sized MoO_2 and (D) nano-sized MoO_2 at potentials between 3.0 V and 1.1 V vs. Li/Li^+, demonstrating the absence of a lithiation-induced phase transformation in the nanosized MoO_2. Reprinted with permission from Ref. [243]. Copyright 2015 IOP Publishing.

Kim et al. compared electrochemical Li^+ intercalation into micro- and nanosized MoO_2 and showed that nanostructuring could eliminate intercalation-induced phase transformations and thus increase charge storage rate capability.[243] The nanosized MoO_2 displayed a highly reversible voltammetric response, a sloping voltage profile in galvanostatic experiments, and much higher rate capability when compared to the micron-sized MoO_2. Ex situ XRD showed that the reversible monoclinic-to-orthorhombic phase transition observed upon lithiation / delithiation of micron-sized MoO_2 (**Fig. 31C-D**) was suppressed in the nanosized MoO_2.

Nanostructuring of a variety of electrode materials such as TMOs and transition metal dichalcogenides (TMDs) was shown to be a viable strategy to introduce a transition from diffusion-controlled to surface-controlled, pseudocapacitive intercalation. The underlying thermodynamic reason for the change from a constant intercalation potential to a sloping potential in nanostructured materials is that a large part of the reaction sites is in the disordered near-surface region, which results in a dispersion of site energies.[61] Furthermore, the suppression of phase transitions and the reduction of diffusion length significantly reduce the kinetic limitations for charge storage in nanostructured materials. One concern with extrinsic pseudocapacitive materials for commercial devices is whether the nanoscale material properties can be translated to commercially viable thick electrodes.[244] The need to maintain sufficient electronic and ionic transport throughout a thick electrode consisting of nanomaterials requires their incorporation into a carefully designed electrode architecture.[245–248]

4.7 Atomic-Scale Tuning to Achieve Pseudocapacitance

More recently, strategies besides nanostructuring have emerged to either induce or increase the pseudocapacitive response of EES materials. Below we highlight several methods to tune the structure or composition of materials to increase the kinetics of coupled electron-ion transport while maintaining a similar density of redox-active sites.

4.7.1 Increasing Electron Transport

One design strategy to increase the EES kinetics of insulating or semiconducting redox-active transition metal oxides, chalcogenides, and carbides is to increase their electronic conductivity.[249] This can be accomplished by engineering the material's electronic band structure by introducing point defects such as oxygen vacancies,[49,250], transition metal vacancies,[251] and substitutional or interstitial doping.[252–254]

Oxygen vacancy formation in transition metal oxides is a common method to enhance the electrical conductivity through intervalence electron charge transfer.[255] Kim et al. investigated the role of oxygen vacancies in nanostructured MoO_{3-x} during Li^+ intercalation (**Fig. 32A)**.[49] The presence of oxygen vacancies not only increased the pseudocapacitive charge storage contribution, but also the rate capability and cycling stability, leading to lithiation kinetics not limited by solid-state diffusion (**Fig. 32A**). This was attributed to both an increase in the electronic conductivity as well as the suppression of irreversible Li^+ trapping in the widened intralayers of MoO_{3-x}.

A similar approach was used to enhance pseudocapacitive charge storage in CeO_{2-x}.[250] An electrodeposition method led to high oxygen vacancy concentrations (4-15 at%) in thin films (<

100 nm) that enhanced electrical conductivity, leading to high volumetric capacities in pH-neutral aqueous electrolytes (415 mAh/cm^3 at 5 mV/s). Oxygen vacancies led to a decrease in the bandgap from 3.2 eV to 1.9 eV, enhancing the electronic transport in reduced CeO_{2-x}. Using DFT, the researchers illustrated increased charge density around Ce ions in non-stoichiometric $CeO_{1.5}$ compared to CeO_2.

Another method to increase electronic conductivity is via the formation of transition metal vacancies. This was demonstrated by selective etching of aluminum and scandium from a $(Mo_{2/3}Sc_{1/3})_2AlC$ MAX phase to form $Mo_{1.33}C$ MXene. Compared to the equivalent Mo_2C MXene, $Mo_{1.33}C$ exhibits vacancies at every third Mo atom (ordered divacancies, **Fig. 32B**). Using four-point probe resistivity measurements, the authors demonstrated improved electrical conductivities of the $Mo_{1.33}C$ MXene compared to the pristine Mo_2C without metal vacancies, which resulted in improved volumetric capacity in acidic electrolyte.[251] The highly conductive $Mo_{1.33}C$ films exhibited capacities of about 100 mAh/cm^3 in 3-µm thick films at charge/discharge times of 650 ms. These results highlight the future possibilities for various MXene compositions containing metal vacancies for high power, high energy density pseudocapacitive storage.

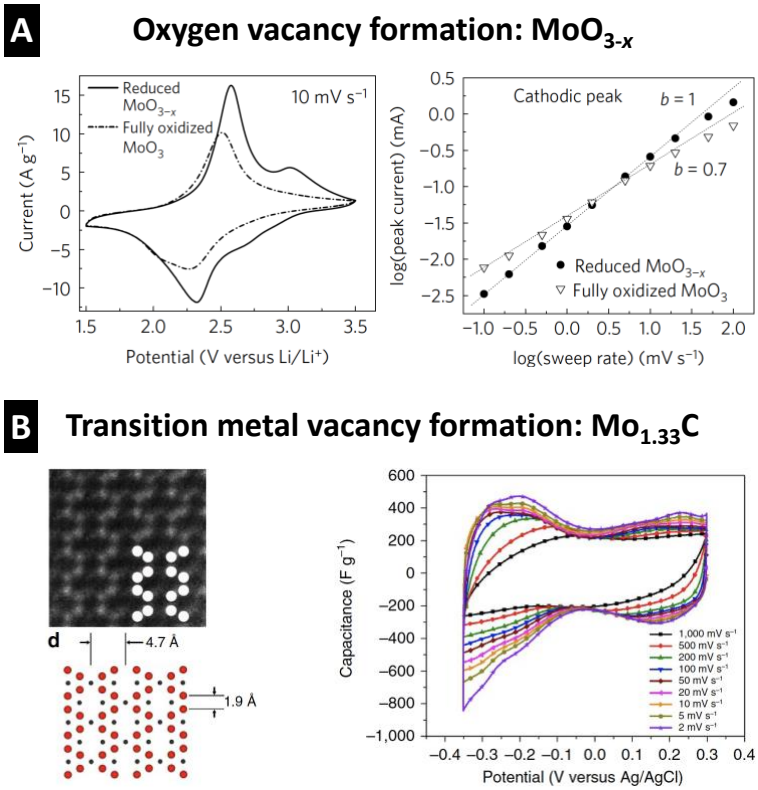

Figure 32: (A) Effects of oxygen vacancies in MoO_{3-x} via cyclic voltammetry (left) and k_1-k_2-analyses (right) in non-aqueous lithium electrolyte. The presence of oxygen vacancies enhances charge storage and increases the contribution of surface-controlled (capacitive) charge storage. Adapted with permission from Ref. [49]. Copyright 2017 Springer Nature. (B) High-angle annular dark-field scanning transmission electron microscopy (HAADF-STEM) image of $Mo_{1.33}C$ MXene flake with ideal atomic structure and cyclic voltammograms of 3 µm thick electrodes in acidic aqueous electrolyte. Adapted with permission from Ref. [251].

Free electron atomic doping is the concept of introducing metallic conductors into semiconducting redox-active materials. For example, the introduction of gold into porous MnO_2 layers enhanced the pseudocapacitive charge storage by 65 % in 1.4 µm thick electrodes, from 380 F/g (95 mAh/g) in the pristine oxide to a value of 626 F/g (157 mAh/g) in the Au-doped film

(ca. 10 at%) with 3 min charge/discharge times.[252] The electronic structure of the Au-doped films was investigated via XPS, which revealed a decrease in the mean valence of the Mn from 3.3 to 2.8 after Au-doping, indicating increased electron density at the Mn metal centers (**Fig. 33**). The design of multifunctional bimetallic materials on the atomic level has been proposed as a means to in situ form electronically conductive percolation networks with one metal while the other undergoes electrochemical redox,[256] and can also serve as a design strategy for new pseudocapacitive materials. It should be noted that in these materials, an alternate explanation for the mechanism of free-electron doping is to enhance EDL charging.

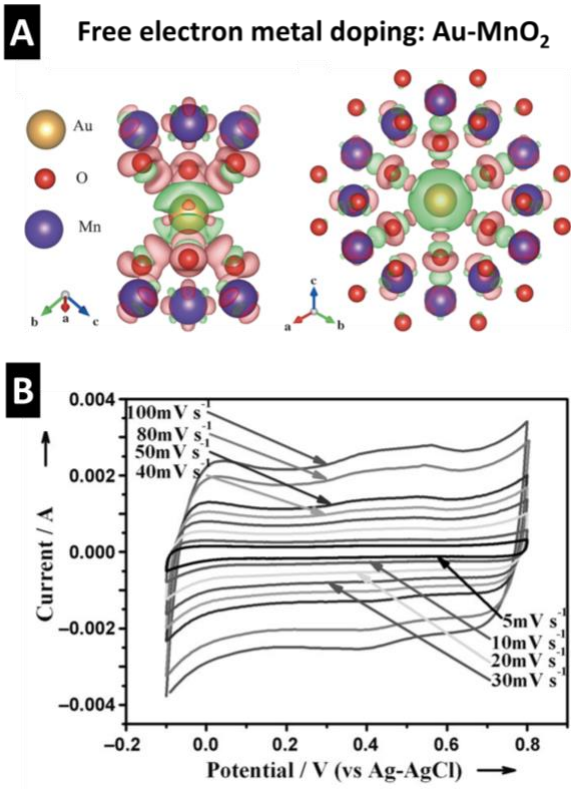

Figure 33: (A) First-principles calculation of the differential charge densities in Au-substituted MnO_2 (left) and Au-interstitial MnO_2 (right), with green depicting a loss and pink a gain of electrons, indicating an increased electron density at Mn metal centers. (B) Cyclic voltammograms of 9.9 at.% Au-doped MnO_2 in an aqueous Li^+ electrolyte. Adapted with permission from Ref. [252]. Copyright 2013 John Wiley and Sons.

4.7.2 Enhancing Ion Transport by Tuning the Interlayer

Two-dimensional and layered materials are some of the most successful materials for electrochemical energy storage due to their ability to reversibly intercalate ions with minimal structural changes, enabling excellent volumetric energy densities with the use of micron-scale particles.[257] It is hypothesized that modifying the interlayer of these materials could result in enhanced interfacial charge transfer and solid-state ion transport,[257,258] both of which are necessary for highly reversible, pseudocapacitive charge storage. Methods to tune the interlayer include nanoconfined fluids,[15,259] conductive polymers,[260–262] and interlayer pillaring via organic intercalants[263,264] and metal cations.[265]

The presence of confined fluids such as structural water in redox-active layered materials has led to high-rate, reversible charge storage. Nanostructured, hydrated transition metal oxides such as those of ruthenium, iridium, and manganese are some of the earliest and most studied pseudocapacitive materials as discussed in Section 3.4. More recently, several studies found that the presence of structural water in crystalline oxides leads to intercalation pseudocapacitance - non-diffusion controlled proton insertion into the interior of bulk-like oxides. For example, structural water in layered, hydrated tungsten oxide ($WO_3 \cdot 2H_2O$) was found to induce a transition from battery-like to pseudocapacitive electrochemical behavior for proton intercalation as compared to anhydrous WO_3.[259] Operando XRD[266] and AFM[267] showed that the pseudocapacitive response emerged due to enhanced structural stability from the presence of highly confined structural water despite the presence of a phase transition (**Fig. 34A-C**). The pseudocapacitive response led to excellent electrochemical reversibility that enabled higher efficiency at fast rates as compared to the anhydrous WO_3.

Perez et al. found that acid leaching of Li_3IrO_4 led to the formation of a protonated iridate, $H_{3+x}IrO_4$, and that the majority of the current in the highly reversible CVs was due to non-diffusion controlled Faradaic processes.[268] In situ XRD showed that protonation led to reversible and continuous lattice spacing changes without a first-order phase transition, indicative of an intercalation pseudocapacitance mechanism. Follow-on work utilizing EQCM and EIS revealed that the Faradaic processes involve the transport of both protons and water molecules.[269] This work highlights that acid leaching of transition-metal containing oxides (similar to selective ion-etching of transition metal carbides to form MXenes) could lead to new high-power materials.

$WO_3 \cdot 2H_2O$ and other hydrated transition metal oxides may also undergo solvent exchange under certain conditions that could lead to the confinement of non-aqueous electrolytes. Understanding the relationship between confined solvent chemistry, electrolyte composition, and electrochemical response is a promising avenue for future research as noted above for MXenes. The move to non-aqueous electrolytes can be beneficial from a device energy density standpoint, although the high conductivity of acidic electrolytes and unique transport of protons could be more beneficial for high power. There can be a tradeoff between power and energy in materials that incorporate confined fluids. For example, the presence of structural water in $WO_3 \cdot 2H_2O$ leads to lower gravimetric and specific capacity at slow rates compared to anhydrous WO_3, presumably because the interlayer water molecules decrease proton intercalation sites and increase volume.

Lee et al.[270] observed a broadened, capacitive voltammetric response and increased capacity in electrodeposited $V_2O_5 \cdot nH_2O$ as compared to annealed orthorhombic V_2O_5 when both were cycled in a 1 M $LiClO_4$ non-aqueous electrolyte. The lower capacity of the anhydrous phase,

even at slow charge/discharge times of about 30 min, was attributed to contraction of the interlayer spacing upon removal of interlayer water, which was hypothesized to limit Li^+ storage sites. Confined water within the interlayer of MXenes is hypothesized to enable their extremely fast proton intercalation.[15] Confinement of hydrazine in the interlayers of $Ti_3C_2T_x$ MXene led to an expanded interlayer from 20.2 Å to 25.4 Å and resulted in an increased capacity as compared to the pristine phase, with <10 s charge/discharge times in aqueous 1 M H_2SO_4 (**Fig. 34D-F**).[264] The confinement of fluids in the interlayer of 2D and layered materials has shown to be a promising emerging strategy for pseudocapacitive charge storage because it can expand interlayer galleries for facile ion diffusion or enable enhanced structural stability.[266]

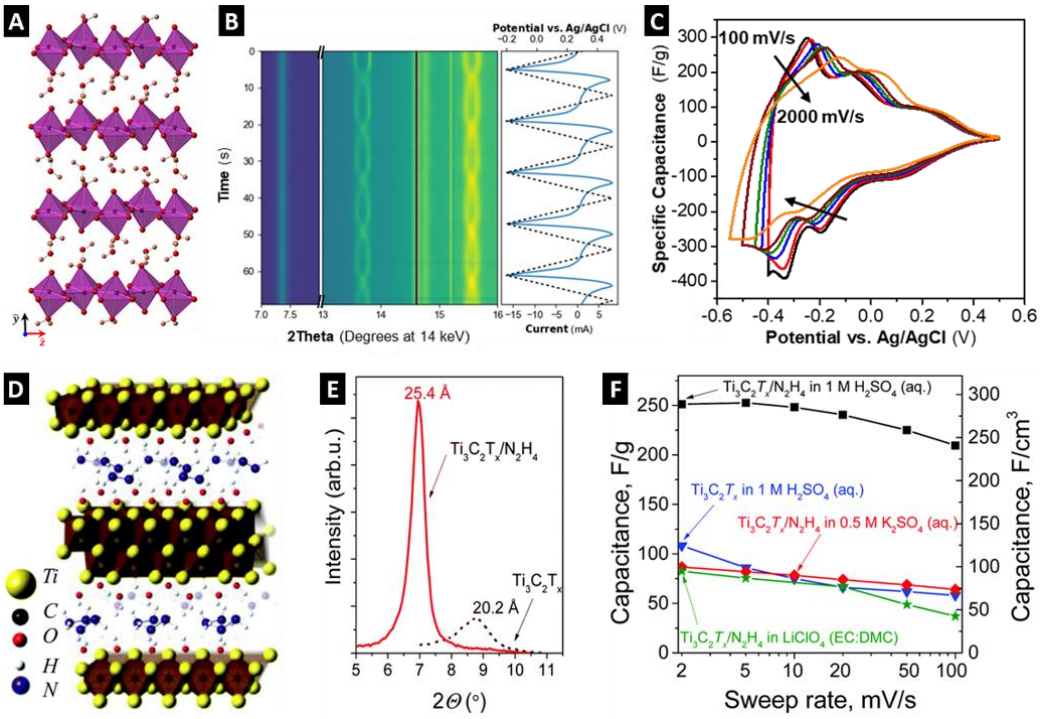

Figure 34: (A) The crystallographic structure of monoclinic $WO_3 \cdot 2H_2O$ consists of 2D layers of corner-sharing $WO_5(OH_2)$ octahedra separated by a layer of structural water weakly bound through hydrogen bonding. (B) Operando synchrotron XRD patterns of a $WO_3 \cdot 2H_2O$ electrode as a function of time at a 100 mV/s sweep rate depicting smooth, continuous phase transformations while the interlayer (010) reflection at ca. 7.5° 2θ remains constant. (C) Cyclic voltammograms of an electrodeposited $WO_3 \cdot 2H_2O$ electrode in acidic aqueous electrolyte from 100 mV/s to 2 V/s. Panels A-C adapted from Ref. [266]. Copyright 2019 American Chemical Society. (D) Structural model of Ti_3C_2OH with intercalated hydrazine (N_2H_4) confined in the interlayer. (E) XRD patterns of pristine and hydrazine-intercalated $Ti_3C_2T_x$ showing increased interlayer spacing after the incorporation of hydrazine. (F) Electrochemical performance of pristine and hydrazine-intercalated $Ti_3C_2T_x$ electrodes in various electrolytes. Panels D-F adapted from Ref. [264] with permission of The Royal Society of Chemistry; permission conveyed through Copyright Clearance Center, Inc.

The introduction of electronically conductive polymers into the interlayers of oxides, sulfides, and MXenes can lead to increased electronic and ionic transport. For example, vanadate nanofibers synthesized with poly(3,4-ethylene dioxythiophene) (PEDOT) in the interlayers had an increased interlayer spacing (from 8.9 Å to 10.2 Å) and electronic conductivity (from 2.2 mS/cm to 41 mS/cm).[260] Both likely contributed to the enhanced capacity (ca. 4x larger than pristine V_2O_5 with 9 s charge/discharge) and highly reversible cyclic voltammograms from 3 - 100 mV/s when cycled in a pH-neutral aqueous electrolyte. This design strategy was also used to increase the kinetics of charge storage in MoS_2 by electropolymerizing polypyrrole (PPy) onto hydrothermally synthesized MoS_2 nanosheets.[261] The PPy not only covered the surface of the nanosheet assemblies but was also found to intercalate within the interlayers of the MoS_2 sheets, causing an interlayer spacing increase from 0.6 nm to 0.9 nm. This composite material showed pseudo-rectangular voltammetric responses in an aqueous 1 M KCl electrolyte at charge / discharge rates as quick as 5 s, with improvements in the capacity (125 mAh/g vs. 28 mAh/g) and rate capability (ca. 70 % retention vs. 35 % with increase in current density from 1 - 10 A/g) compared to the pristine sulfide. A heterostructure formed by the polymerization of PANI on $Ti_3C_2T_x$ MXene layers led to decreased Ohmic losses in thick electrode films (**Fig. 35**).[262] A 90 µm-thick electrode of the composite with 25 mg/cm^2 loading had a gravimetric capacity of ~ 83 mAh/g for 15 min charge/discharge times in aqueous 1 M KCl. These results highlight the advantages of forming heterostructure interfaces between conductive polymers and layered oxides, chalcogenides, and MXenes.

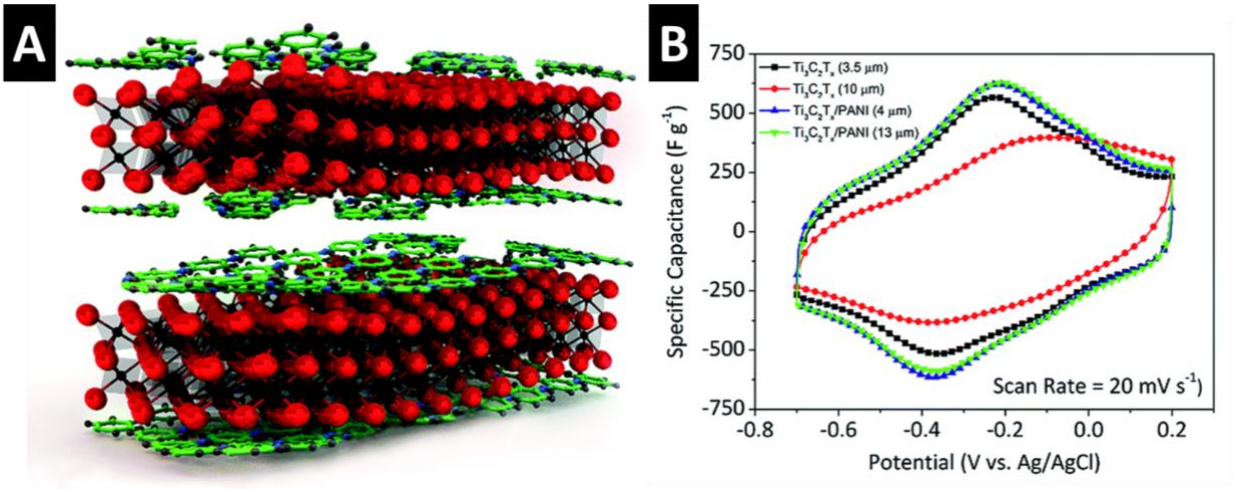

Figure 35: (A) Schematic of the heterostructure formed by the polymerization of aniline on the surface of 2D $Ti_3C_2T_x$ MXene sheets. (B) Cyclic voltammograms of pristine $Ti_3C_2T_x$ and $Ti_3C_2T_x$/PANI electrodes as a function of electrode thickness. As the pristine $Ti_3C_2T_x$ electrode thickness increased, the Ohmic losses lead to the tilting of the voltammogram and capacity fading. The $Ti_3C_2T_x$ / PANI heterostructure electrode limited Ohmic losses and retained more capacity in thick electrodes. Panels adapted from Ref. [262] with permission of The Royal Society of Chemistry; permission conveyed through Copyright Clearance Center, Inc.

Another concept to tune ionic transport in layered materials is to pillar the interlayer with cations or other molecules. It is hypothesized that tuning the interlayer distance with pillars could inhibit lattice breathing during electrochemical cycling and increase cation transport, both of which could lead to better kinetics and cycling stability (**Fig. 36**).[265,271–274]

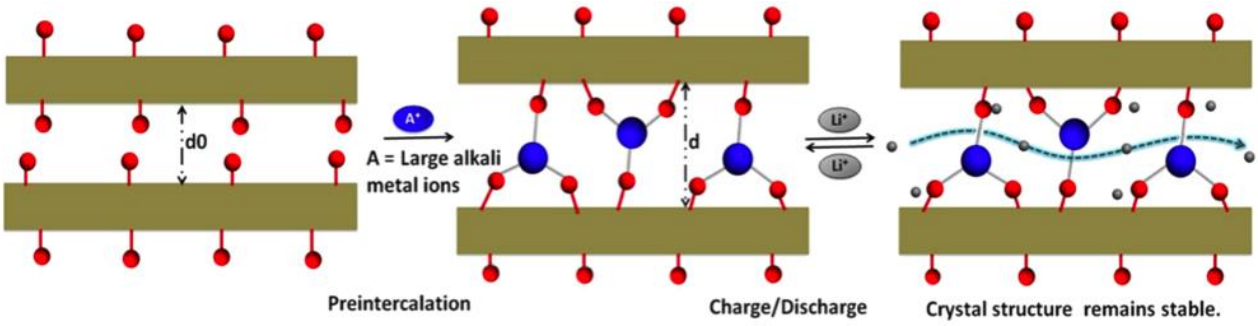

Figure 36: Schematic showing the intercalation of large alkali metal ions into the interlayer of a layered compound, which can stabilize the structure and facilitate ion transport. Figure adapted from Ref. [265]. Copyright 2015 American Chemical Society.

The effect of alkali cation pre-intercalation into birnessite MnO_2 was investigated in both aqueous and non-aqueous electrolytes. In an aqueous Na_2SO_4 electrolyte, Li^+ pre-intercalation was beneficial for subsequent Na^+ intercalation. It was hypothesized that the smaller Li^+ pillars enhanced ionic transport during subsequent (de-)intercalation reactions.[275] A different trend was observed in organic $NaClO_4$ electrolyte, where the pre-intercalation of larger alkali cations resulted in higher capacity.[274]

Pillaring by the use of divalent cations was investigated by pre-intercalating Mg^{2+} within titania nanosheets.[273] The self-assembly process led to an increase in interlayer distance from 0.76 nm to 1.15 nm. The Mg-pillared material exhibited a disordered, turbostratic structure and was

hypothesized to have weakened layer-to-layer interactions which were beneficial for electrochemical ion (de-)intercalation. Compared to the more ordered parent titanate phase, the Mg-pillared materials exhibited higher capacity and cyclability in non-aqueous Na^+ and K^+ electrolytes.

Transition metal cations can be utilized to pillar the interlayer. Fe^{3+} was pre-intercalated into the interlayer of a V_2O_5 xerogel to inhibit interlayer changes during electrochemical cycling .[271] Ex situ XRD found that the presence of Fe^{3+} within the interlayer limited the lattice breathing during charge / discharge in a non-aqueous Na^+ electrolyte, leading to enhanced cyclability as compared to the pristine V_2O_5 xerogel. The energy storage kinetics increased even though the Fe^{3+}-pillared V_2O_5 had a smaller interlayer spacing than the pristine material. A comparison of the EIS measurements of the two materials showed a significant decrease in the charge transfer resistance due to the presence of Fe^{3+} pillars, indicating that the pre-intercalated cations may also lower the activation barriers for charge transfer.

Organic molecules have been used to pillar the interlayer of layered materials, leading to the formation of electrochemically active organic/inorganic hybrid materials. Dong et al. incorporated pyridine to inhibit the electrochemically-induced distortion and subsequent capacity fading of V_2O_5.[276] The neutral base behavior (proton acceptor) of pyridine was hypothesized to lead to hydrogen bonding with the V_2O_5 lattice, effectively stabilizing the interlayer. In situ XRD showed that the layered structure was stabilized by suppressing a phase transformation during electrochemical Na^+ intercalation/deintercalation in a non-aqueous sodium-containing electrolyte. This led to an overall increased cyclability, and similarly to the cation-pillared materials, the pyridine-V_2O_5 material exhibited higher capacity and rate capability,

despite a decreased interlayer spacing as compared to the pristine V_2O_5. This indicates that the chemical environment of the interlayer, and not just the interlayer distance, is a factor in tuning the electrochemical energy storage kinetics of materials.

The concept of tuning the interlayer opens a wide range of intercalants and chemistries to optimize the stability, ion-accessibility, and reactivity for high-rate, reversible pseudocapacitive charge storage. As indicated by the instability of structural water[277] and pre-intercalated cations[273,275] in the presence of chemical or electric potential gradients, it is important to consider the stability of the interlayer modifications during electrochemical cycling. Tuning the interlayer of 2D and layered materials should include a stable intercalant that can withstand thousands of charge / discharge cycles at high rates relevant for pseudocapacitive materials (<10 min). Other advancement opportunities include the potential coupling of experimental and computational studies to determine how interlayer intercalants can modify the chemical, mechanical, and electronic properties of layered materials to induce pseudocapacitive charge storage mechanisms and achieve combined high energy and high-power electrochemical energy storage.

5. Opportunities and Outlook

Increased electrification is pushing for significant application opportunities for EES, and nearly all benefit from improved power. The past decade has seen the blurring of lines between different EES technologies. A new understanding of electrical double-layer phenomena under confinement by high surface area carbon materials indicates that high capacitance involves ion desolvation[278] or non-Coulombic ion ordering.[279] Such mechanisms are not far from what may occur in redox-active 2D and layered materials that confine electrolytes. Carbon materials used in EDLCs also gained redox functionalities. On the other end of the spectrum, rechargeable batteries became dominated by Li-ion intercalation, a unique mechanism since, until recently, the most dominant rechargeable battery (lead-acid) utilized conversion chemistry. The concept of pseudocapacitance, first proposed in the 1960s, connects the fields of intercalation-type batteries with electrochemical capacitors. While much of Li-ion battery research is concerned with bulk solid-state phenomena such as phase transformations and solid-state diffusion, pseudocapacitance places the focus for EES on the mechanisms of charge transfer at an electrochemical interface. In this way, pseudocapacitance connects fundamental electrochemistry and surface science with EES applications. Furthermore, the materials discussed in this review are versatile and can be used in a number of applications that require high power Faradaic storage – from electrochemical capacitors to high power batteries as well as capacitive deionization and neuromorphic computing.

Recent discussions in the field of pseudocapacitance have included criticism of the misapplication of the term that leads to over-reporting of capacitance values[22] as well as criticism of the existence of the concept itself.[63] These criticisms works underscore the need for

fundamental understanding of electrochemical charge transfer from an atomistic perspective, including how it is affected by the EDL. This is increasingly enabled by close collaboration between theory/computation, the development of new materials, and new operando experimental tools with sub-minute sampling intervals. Such techniques are the most relevant for the highly non-equilibrium conditions encountered in pseudocapacitive materials that operate on minute-to-second timescales.

At the application end of the spectrum, one can wonder about the practical utility of a quantitatively decoupling surface from diffusion-controlled current to the end-consumer of a high power energy storage device. Pseudocapacitance focuses on materials that exhibit surface-controlled charge storage on minute-to-second timescales in a variety of electrolytes and, in doing so, proposes unique materials for EES. As an example, Nb_2O_5 was largely underexplored for EES prior to the 2013 report that its intercalation kinetics could be considered pseudocapacitive.[44] Before 2013, the number of papers investigating "Nb_2O_5 intercalation" was relatively flat, often with fewer than 5 papers per year. Since 2013, the number has increased steadily so that in 2019, 40 reports were published on this topic, and several companies are pursuing the commercialization of a niobium oxide-based electrode.

5.1 Mechanistic Understanding of Pseudocapacitance

In an ideal battery, the electrochemical reaction occurs at a well-defined potential with the extent of charge due to a well-defined Gibbs free energy of the reaction, which can be obtained from thermodynamic data. A classic example is a lithium-iodine battery: lithium is oxidized to Li^+ while iodine is reduced to lithium iodide at 3.1 V. As discussed above, a material that exhibits a

pseudocapacitive response has a sloping, or continuously varying, potential with the extent of charge and operates far from equilibrium at sub-minute timescales. In these cases, the nature of the redox reactions contributing to charge storage processes is not obvious from the electrochemical response, nor can it be readily calculated from thermodynamic data for bulk materials. Moreover, as discussed in this review, many pseudocapacitive materials confine fluids such as structural water in hydrous grain boundaries or interlayers. In such materials, the question arises over where to draw the electrochemical interface: at the outer surface of the particle, or within a solvated interlayer? There are many exciting opportunities for future studies on pseudocapacitive materials that utilize computation and theory combined with operando characterization techniques to determine the atomic-scale mechanism. This understanding would be beneficial not just for the field of energy storage, but for the myriad of electrochemical technologies that require understanding of interfacial redox processes.

Developing predictive models for the atomistic simulation of the electrochemical interfaces is at the forefront of theoretical and computational efforts in understanding electric energy-storage mechanisms. Key to this development is the integration of electronic structure and surface chemistry of the electrode, the applied potential across the interface and the double-layer formation, and the explicit solvation environment, in a self-consistent and dynamic manner. Ideally, one would like to know from such a model how the electrode material responds (via changes in oxidation states, lattice parameters, site occupancy, etc.) to the applied potential in a given electrolyte, which can be verified by operando characterization techniques. Once these predictive models are developed, computation would be able to guide materials synthesis and

design so that, for example, the effects of point defects or interlayer pillars could be determined computationally first.

Characterization should be performed at timescales relevant to pseudocapacitive materials. Here, we highlight several operando techniques that have recently shed light on pseudocapacitive mechanisms. Electrochemical quartz crystal microbalance (EQCM) can help determine the nature of the adsorbed or intercalated species that gives rise to pseudocapacitance.[68,280,281] Pseudocapacitive materials have been shown to exhibit structural changes during the charge storage process since charge transfer inevitably requires the accommodation of ions and charge distribution. Raman spectroscopy provides information on local structural changes.[119,164,282] Synchrotron XRD can be performed at timescales relevant for pseudocapacitive processes to provide information on structural dynamics that occur due to adsorption or intercalation processes.[266] Synchrotron XAS can be used to directly identify the redox couple in situations where the electrochemical response does not give rise to clear redox peaks, or multiple redox-active species are present.[283] Atomic force microscopy (AFM) can be used to measure the mechanical deformation associated with pseudocapacitance and enables temporal and spatial resolution.[267] For electrochromic materials, recent electro-optical imaging that utilizes the time-dependent equations used for SPECS can be applied to monitor cation concentration with the change of optical density. Evans et al. used this method to study the extrinsic pseudocapacitance of hexagonal WO_3 nanoparticles.[284] The emphasis is again placed on those techniques that can be performed operando to capture the far-from-equilibrium processes occurring at sub-minute timescales.

5.2 Pseudocapacitive Electrode Architectures

Fundamental studies of pseudocapacitance are typically performed on electrodes that limit mass transfer limitations stemming from thickness effects (such as electrolyte starvation or low particle-to-particle electron transport) or that are designed for a particular type of operando characterization. Once a pseudocapacitive material has been shown to demonstrate attractive high power behavior, the next challenge is to preserve the thin-film response in an electrode architecture that provides meaningful areal or volumetric capacity, which typically require areal loadings of >10 mg/cm^2.[244] Simply increasing the electrode thickness is often not feasible because it is essential to have a continuous electrical and ionic network across the entire electrode thickness for high rates.

There are two main strategies to introduce electrical conductivity to the electrode: (i) The use of a conductive additive, such as carbon black, which is homogeneously mixed with the active material; or (ii) a hybridization approach, where active material and carbon are linked on a nanoscale level. In both cases, the electrode must retain an interconnected and hierarchical porosity to enable efficient electrolyte access. When conductive additives are used, a careful mixing of both phases has to be ensured, which requires both the choice of suitable particle size and amount of conductive additive, as well as a well-adjusted mixing procedure.[285] This is especially important for nanostructured active materials which constitute the vast majority of pseudocapacitive materials. It can be particularly challenging to maintain intimate contact between the nanoscopic active material and conductive additive over many cycles by simple physical mixing of the particles.[286] In these cases, the hybridization of the active material with a conductive carbon network is desirable. There are many synthesis approaches for hybrid

materials, and comprehensive reviews on the topic can be found, for example, in Ref. [245]. In short, one can differentiate between the coating of active materials on carbon substrates, the use of conductive carbon shells surrounding active material, or the co-synthesis of carbon and active material.

Studies aiming to develop three-dimensional, conductive networks or scaffolds that can enable high areal performance at elevated rates are at the focus of applied research today.[232,247] Examples are the use of three-dimensional networks of holey graphene that incorporate Nb_2O_5 as an active material or synthesizing interconnected gyroid structures that combine active material nanoparticles engulfed in a highly regular three-dimensional frame of porous carbon.[287,288]

5.3 Devices that Incorporate Pseudocapacitive Materials

Pseudocapacitive materials are promising for achieving simultaneously high rate, high energy density, and high-efficiency energy storage systems based on ion adsorption and/or intercalation. They can be incorporated as electrodes into rechargeable batteries or hybrid capacitors. However, two aspects of integrating pseudocapacitive materials into devices require further understanding: 1) the choice of electrolyte, which may be different for materials that operate at pseudocapacitive timescales and thus require fast interfacial charge transfer, and 2) the impact of electrode coupling or cross talk. As more pseudocapacitive materials are identified and integrated into devices, these aspects are likely to gain prominence. In a recent example, the choice of electrolyte solvent was shown to be highly important for pseudocapacitive MXenes. Wang et al. reported on the doubled charge storage capacity of Li^+-containing, organic

electrolytes with Ti_3C_2 when propylene carbonate was used as the solvent instead of acetonitrile or dimethyl sulfoxide.[202] The carbonate electrolyte enabled a complete desolvation of the Li^+, leading to high rate pseudocapacitive intercalation reactions. Hence the matching of a suitable solvent, electrolyte salt, and electrode material can drastically increase the pseudocapacitive performance of the studied system. Matching of electrode materials is likely to lead to similar advancements in performance.

The fast and reversible electrochemical charge transfer reactions of pseudocapacitive materials are attractive for fields beyond EES. One of the most prominent is capacitive deionization of water, which is typically accomplished by the potential-driven adsorption of aqueous ions onto carbon electrodes via the formation of the EDL. As in EES, the use of pseudocapacitive materials could lead to higher ion storage capacities while maintaining the fast storage timescales necessary for water purification.[289,290] Pseudocapacitive materials have also been explored in applications beyond energy, such as for actuators, where their rapid ion intercalation kinetics could enable fast actuation.[291,292] Looking forward, the combination of fast ion transport and physical property change in pseudocapacitive materials could also be of interest for neuromorphic computing applications.[293]

Acknowledgments

S.F., R.W., D.E.J. and V.A. acknowledge the support of the Fluid Interface Reactions, Structures, and Transport (FIRST) Center, an Energy Frontier Research Center funded by the U.S. Department of Energy, Office of Science, Office of Basic Energy Sciences for research on capacitive energy storage. J.B.M. and V.A. also acknowledge the support from the National Science Foundation under Grant. No. 1653827 for research on ion transport in solvated metal oxides. V.P. thanks Eduard Arzt (INM) for his continuing support and acknowledges support via the Carbon Metal Oxide Nanohybrid project (CarMON) supported by the Leibniz Association (SAW-2017). Part of this work (C.Z.) was performed under the auspices of the U.S. Department of Energy by Lawrence Livermore National Laboratory under Contract DE-AC52-07NA27344. C.Z. is partially supported by the PLS-Postdoctoral Grant of the Lawrence Livermore National Laboratory.

References

(1.) Smith, P. F.; Takeuchi, K. J.; Marschilok, A. C.; Takeuchi, E. S. Holy Grails in Chemistry: Investigating and Understanding Fast Electron/Cation Coupled Transport within Inorganic Ionic Matrices. *Acc. Chem. Res.* **2017**, 50, 544–548.

(2.) European Commission, Integrated Strategic Energy Technology Plan Action 7 - "Become competitive in the global battery sector to drive e-mobility forward."

(3.) Ministry of Science and Technology of the Peoples's Republic of China http://www.most.gov.cn/kjbgz/201908/t20190807_148190.htm (accessed Mar 4, 2020).

(4.) Bard, A. J.; Inzelt, G.; Scholz, F. *Electochemical Dictionary*; Springer Science & Business Media, **2008**.

(5.) Whittingham, M. S. Electrical Energy Storage and Intercalation Chemistry. *Science* **1976**, 192, 1126–1127.

(6.) Mizushima, K.; Jones, P. C.; Wiseman, P. J.; Goodenough, J. B. LixCoO2 (0<x<-1): A New Cathode Material for Batteries of High Energy Density. *Mater. Res. Bull.* **1980**, 15, 783–789.

(7.) Nishi, Y.; Azuma, H.; Omaru, A. Non Aqueous Electrolyte Cell. U.S. Patent No. 4,959,281. 1990.

(8.) Yamahira, T.; Kato, H.; Anzai, M. Nonaqueous Electrolyte Secondary Battery. U.S. Patent No. 5,053,297. 1991.

(9.) Nitta, N.; Wu, F.; Lee, J. T.; Yushin, G. Li-Ion Battery Materials: Present and Future. *Mater. Today* **2015**, 18, 252–264.

(10.) Simon, P.; Gogotsi, Y. Materials for Electrochemical Capacitors. *Nat. Mater.* **2008**, 7, 845–

854.

(11.) Gür, T. M. Review of Electrical Energy Storage Technologies, Materials and Systems: Challenges and Prospects for Large-Scale Grid Storage. *Energy Environ. Sci.* **2018**, 11, 2696–2767.

(12.) Zhu, M.; Park, J.; Sastry, A. M. Fracture Analysis of the Cathode in Li-Ion Batteries: A Simulation Study. *J. Electrochem. Soc.* **2012**, 159, A492–A498.

(13.) Trasatti, S.; Buzzanca, G. Ruthenium Dioxide: A New Interesting Electrode Material. Solid State Structure and Electrochemical Behaviour. *J. Electroanal. Chem.* **1971**, 29, A1–A5.

(14.) Conway, B. E. *Electrochemical Supercapacitors: Scientific Fundamentals and Technological Applications*; Springer Science & Business Media, **2013**.

(15.) Lukatskaya, M. R.; Kota, S.; Lin, Z.; Zhao, M. Q.; Shpigel, N.; Levi, M. D.; Halim, J.; Taberna, P. L.; Barsoum, M. W.; Simon, P.; Gogotsi, Y. Ultra-High-Rate Pseudocapacitive Energy Storage in Two-Dimensional Transition Metal Carbides. *Nat. Energy* **2017**, 6, 17105.

(16.) Abruña, H. D.; Kiya, Y.; Henderson, J. C. Batteries and Electrochemical Capacitors. *Phys. Today* **2008**, 61, 43–47.

(17.) Grahame, D. C. Properties of the Electrical Double Layer at a Mercury Surface. I. Methods of Measurement and Interpretation of Results. *J. Am. Chem. Soc.* **1941**, 63, 1207–1215.

(18.) Srinivasan, S.; Gileadi, E. The Potential-Sweep Method: A Theoretical Analysis. *Electrochim. Acta* **1966**, 11, 321–335.

(19.) Conway, B. E.; Gileadi, E. Kinetic Theory of Pseudo-Capacitance and Electrode Reactions at Appreciable Surface Coverage. *Trans. Faraday Soc.* **1962**, 58, 2493–2509.

(20.) Scholz, F.; Leiva, E. P. M. Moïse Haïssinsky: The Discoverer of Underpotential Deposition.

ChemElectroChem **2018**, 5, 849–854.

(21.) Herrero, E.; Buller, L. J.; Abruña, H. D. Underpotential Deposition at Single Crystal Surfaces of Au, Pt, Ag and Other Materials. *Chem. Rev.* **2001**, 101, 1897–1930.

(22.) Brousse, T.; Bélanger, D.; Long, J. W. To Be or Not To Be Pseudocapacitive? *J. Electrochem. Soc.* **2015**, 162, A5185–A5189.

(23.) Ardizzone, S.; Fregonara, G.; Trasatti, S. "Inner" and "Outer" Active Surface of RuO2 Electrodes. *Electrochim. Acta* **1990**, 35, 263–267.

(24.) Zheng, J. P.; Cygan, P. J.; Jow, T. R. Hydrous Ruthenium Oxide as an Electrode Material for Electrochemical Capacitors. *J. Electrochem. Soc.* **1995**, 142, 2699–2703.

(25.) Augustyn, V.; Simon, P.; Dunn, B. Pseudocapacitive Oxide Materials for High-Rate Electrochemical Energy Storage. *Energy Environ. Sci.* **2014**, 7, 1597–1614.

(26.) Lee, H. Y.; Goodenough, J. B. Supercapacitor Behavior with KCl Electrolyte. *J. Solid State Chem.* **1999**, 144, 220–223.

(27.) Shirakawa, H.; Louis, E. J.; MacDiarmid, A. G.; Chiang, C. K.; Heeger, A. J. Synthesis of Electrically Conducting Organic Polymers: Halogen Derivatives of Polyacetylene, (CH)X. *J. Chem. Soc. Chem. Commun.* **1977**, No. 16, 578–580.

(28.) Gholamian, M.; Sundaram, J.; Contractor, A. Q. Oxidation of Formic Acid at Polyaniline-Coated and Modified-Polyaniline-Coated Electrodes. *Langmuir* **1987**, 3, 741–744.

(29.) Abdelhamid, M. E.; O'Mullane, A. P.; Snook, G. A. Storing Energy in Plastics: A Review on Conducting Polymers & Their Role in Electrochemical Energy Storage. *RSC Adv.* **2015**, 5, 11611–11626.

(30.) Snook, G. A.; Kao, P.; Best, A. S. Conducting-Polymer-Based Supercapacitor Devices and

Electrodes. *J. Power Sources* **2011**, 196, 1–12.

(31.) Bryan, A. M.; Santino, L. M.; Lu, Y.; Acharya, S.; D'Arcy, J. M. Conducting Polymers for Pseudocapacitive Energy Storage. *Chem. Mater.* **2016**, 28, 5989–5998.

(32.) Rudge, A.; Davey, J.; Raistrick, I.; Gottesfeld, S.; Ferraris, J. P. Conducting Polymers as Active Materials in Electrochemical Capacitors. *J. Power Sources* **1994**, 47, 89–107.

(33.) Sivakkumar, S. R.; Saraswathi, R. Performance Evaluation of Poly(N-Methylaniline) and Polyisothianaphthene in Charge-Storage Devices. *J. Power Sources* **2004**, 137, 322–328.

(34.) Frackowiak, E.; Khomenko, V.; Jurewicz, K.; Lota, K.; Béguin, F. Supercapacitors Based on Conducting Polymers/Nanotubes Composites. *J. Power Sources* **2006**, 153, 413–418.

(35.) Lota, K.; Khomenko, V.; Frackowiak, E. Capacitance Properties of Poly(3,4-Ethylenedioxythiophene)/Carbon Nanotubes Composites. *J. Phys. Chem. Solids* **2004**, 65, 295–301.

(36.) Kovalenko, I.; Bucknall, D. G.; Yushin, G. Detonation Nanodiamond and Onion-like-Carbon-Embedded Polyaniline for Supercapacitors. *Adv. Funct. Mater.* **2010**, 20, 3979–3986.

(37.) Simotwo, S. K.; Delre, C.; Kalra, V. Supercapacitor Electrodes Based on High-Purity Electrospun Polyaniline and Polyaniline-Carbon Nanotube Nanofibers. *ACS Appl. Mater. Interfaces* **2016**, 8, 21261–21269.

(38.) Liu, T.; Finn, L.; Yu, M.; Wang, H.; Zhai, T.; Lu, X.; Tong, Y.; Li, Y. Polyaniline and Polypyrrole Pseudocapacitor Electrodes with Excellent Cycling Stability. *Nano Lett.* **2014**, 14, 2522–2527.

(39.) Wang, Z.; Zhu, M.; Pei, Z.; Xue, Q.; Li, H.; Huang, Y.; Zhi, C. Polymers for Supercapacitors:

Boosting the Development of the Flexible and Wearable Energy Storage. *Mater. Sci. Eng. R Reports* **2020**, 139, 100520.

(40.) Conway, B. E. Transition from “Supercapacitor” to “Battery” Behavior in Electrochemical Energy Storage. *J. Electrochem. Soc.* **1991**, 138, 1539–1548.

(41.) Conway, B. E. Two-Dimensional and Quasi-Two-Dimensional Isotherms for Li Intercalation and Upd Processes at Surfaces. *Electrochim. Acta* **1993**, 38, 1249–1258.

(42.) Levi, M. D.; Aurbach, D. Frumkin Intercalation Isotherm - a Tool for the Description of Lithium Insertion into Host Materials: A Review. *Electrochim. Acta* **1999**, 45, 167–185.

(43.) Zukalová, M.; Kalbáč, M.; Kavan, L.; Exnar, I.; Graetzel, M. Pseudocapacitive Lithium Storage in TiO2(B). *Chem. Mater.* **2005**, 17, 1248–1255.

(44.) Augustyn, V.; Come, J.; Lowe, M. A.; Kim, J. W.; Taberna, P. L.; Tolbert, S. H.; Abruña, H. D.; Simon, P.; Dunn, B. High-Rate Electrochemical Energy Storage through Li+ Intercalation Pseudocapacitance. *Nat. Mater.* **2013**, 12, 518–522.

(45.) Naguib, M.; Kurtoglu, M.; Presser, V.; Lu, J.; Niu, J.; Heon, M.; Hultman, L.; Gogotsi, Y.; Barsoum, M. W. Two-Dimensional Nanocrystals Produced by Exfoliation of Ti3AlC2. *Adv. Mater.* **2011**, 23, 4248–4253.

(46.) Come, J.; Augustyn, V.; Kim, J. W.; Rozier, P.; Taberna, P.-L.; Gogotsi, P.; Long, J. W.; Dunn, B.; Simon, P. Electrochemical Kinetics of Nanostructured Nb2O5 Electrodes. *J. Electrochem. Soc.* **2014**, 161, A718–A725.

(47.) Dong, W.; Rolison, D. R.; Dunn, B. Electrochemical Properties of High Surface Area Vanadium Oxide Aerogels. *Electrochem. Solid-State Lett.* **2000**, 3, 457–459.

(48.) Charles, D. S.; Feygenson, M.; Page, K.; Neuefeind, J.; Xu, W.; Teng, X. Structural Water

Engaged Disordered Vanadium Oxide Nanosheets for High Capacity Aqueous Potassium-Ion Storage. *Nat. Commun.* **2017**, 8, 15520.

(49.) Kim, H. S.; Cook, J. B.; Lin, H.; Ko, J. S.; Tolbert, S. H.; Ozolins, V.; Dunn, B. Oxygen Vacancies Enhance Pseudocapacitive Charge Storage Properties of MoO3-X. *Nat. Mater.* **2017**, 16, 454–462.

(50.) Ding, J.; Hu, W.; Paek, E.; Mitlin, D. Review of Hybrid Ion Capacitors: From Aqueous to Lithium to Sodium. *Chem. Rev.* **2018**, 118, 6457–6498.

(51.) Naoi, K.; Ishimoto, S.; Miyamoto, J. I.; Naoi, W. Second Generation "Nanohybrid Supercapacitor": Evolution of Capacitive Energy Storage Devices. *Energy Environ. Sci.* **2012**, 5, 9363–9373.

(52.) Conway, B. E.; Angerstein-Kozlowska, H. Electrochemical Study of Multiple-State Adsorption in Monolayers. *Acc. Chem. Res.* **1981**, 14, 49–56.

(53.) Hadži-Jordanov, S. Reversibility and Growth Behavior of Surface Oxide Films at Ruthenium Electrodes. *J. Electrochem. Soc.* **1978**, 125, 1471.

(54.) Hadži-Jordanov, S.; Angerstein-Kozlowska, H.; Conway, B. E. Surface Oxidation and H Deposition at Ruthenium Electrodes: Resolution of Component Processes in Potential-Sweep Experiments. *J. Electroanal. Chem.* **1975**, 60, 359–362.

(55.) Gómez, R.; Orts, J. M.; Álvarez-Ruiz, B.; Feliu, J. M. Effect of Temperature on Hydrogen Adsorption on Pt(111), Pt(110), and Pt(100) Electrodes in 0.1 M HClO4. *J. Phys. Chem. B* **2004**, 108, 228–238.

(56.) Angerstein-Kozlowska, H.; Conway, B. E.; Sharp, W. B. A. The Real Condition of Electrochemically Oxidized Platinum Surfaces. Part I. Resolution of Component Processes.

J. Electroanal. Chem. **1973**, 43, 9–36.

(57.) Conway, B. E. The Electrochemical Behavior of Ruthenium Oxide (RuO2) as a Material for Electrochemical Capacitors. In *Electrochem. Supercapacitors*; **1999**; pp 259–297.

(58.) Bard, A. J.; Inzelt, G.; Scholz, F. *Electrochemical Dictionary*; Springer Science & Business Media, **2008**.

(59.) Costentin, C.; Porter, T. R.; Savéant, J. M. How Do Pseudocapacitors Store Energy? Theoretical Analysis and Experimental Illustration. *ACS Appl. Mater. Interfaces* **2017**, 9, 8649–8658.

(60.) Eftekhari, A. Energy Efficiency: A Critically Important but Neglected Factor in Battery Research. *Sustain. Energy Fuels* **2017**, 1, 2053–2060.

(61.) Okubo, M.; Hosono, E.; Kim, J.; Enomoto, M.; Kojima, N.; Kudo, T.; Zhou, H.; Honma, I. Nanosize Effect on High-Rate Li-Ion Intercalation in LiCoO2 Electrode. *J. Am. Chem. Soc.* **2007**, 129, 7444–7452.

(62.) Shin, J. Y.; Samuelis, D.; Maier, J. Sustained Lithium-Storage Performance of Hierarchical, Nanoporous Anatase TiO2 at High Rates: Emphasis on Interfacial Storage Phenomena. *Adv. Funct. Mater.* **2011**, 21, 3464–3472.

(63.) Costentin, C.; Savéant, J. M. Energy Storage: Pseudocapacitance in Prospect. *Chem. Sci.* **2019**, 10, 5656–5666.

(64.) Dmowski, W.; Egami, T.; Swider-Lyons, K. E.; Love, C. T.; Rolison, D. R. Local Atomic Structure and Conduction Mechanism of Nanocrystalline Hydrous RuO2 from X-Ray Scattering. *J. Phys. Chem. B* **2002**, 106, 12677–12683.

(65.) Yoshida, N.; Yamada, Y.; Nishimura, S. I.; Oba, Y.; Ohnuma, M.; Yamada, A. Unveiling the

Origin of Unusual Pseudocapacitance of RuO2·nH2O from Its Hierarchical Nanostructure by Small-Angle x-Ray Scattering. *J. Phys. Chem. C* **2013**, 117, 12003–12009.

(66.) Nam, K. W.; Kim, M. G.; Kim, K. B. In Situ Mn K-Edge X-Ray Absorption Spectroscopy Studies of Electrodeposited Manganese Oxide Films for Electrochemical Capacitors. *J. Phys. Chem. C* **2007**, 111, 749–758.

(67.) García-Cañadas, J.; Mora-Seró, I.; Fabregat-Santiago, F.; Bisquert, J.; Garcia-Belmonte, G. Analysis of Cyclic Voltammograms of Electrochromic A-WO3 Films from Voltage-Dependent Equilibrium Capacitance Measurements. *J. Electroanal. Chem.* **2004**, 565, 329–334.

(68.) Levi, M. D.; Lukatskaya, M. R.; Sigalov, S.; Beidaghi, M.; Shpigel, N.; Daikhin, L.; Aurbach, D.; Barsoum, M. W.; Gogotsi, Y. Solving the Capacitive Paradox of 2D MXene Using Electrochemical Quartz-Crystal Admittance and in Situ Electronic Conductance Measurements. *Adv. Energy Mater.* **2015**, 5, 1400815.

(69.) Bueno, P. R. Nanoscale Origins of Super-Capacitance Phenomena. *J. Power Sources* **2019**, 414, 420–434.

(70.) Bandaru, P. R.; Yamada, H.; Narayanan, R.; Hoefer, M. Charge Transfer and Storage in Nanostructures. *Mater. Sci. Eng. R Reports* **2015**, 96, 1–69.

(71.) Ando, Y.; Okubo, M.; Yamada, A.; Otani, M. Capacitive versus Pseudocapacitive Storage in MXene. *Adv. Funct. Mater.* **2020**, 2000820.

(72.) Gogotsi, Y.; Penner, R. M. Energy Storage in Nanomaterials - Capacitive, Pseudocapacitive, or Battery-Like? *ACS Nano* **2018**, 12, 2081–2083.

(73.) Bard, A. J.; Faulkner, L. R. *Electrochemical Methods: Fundamentals and Applications*; John

Wiley & Sons, **2000**.

(74.) Conway, B. E. Similarities and Differences between Supercapacitors and Batteries for Storing Electrical Energy. In *Electrochem. Supercapacitors Sci. Fundam. Technol. Appl.*; **1999**; pp 11–31.

(75.) Ji, H.; Zhao, X.; Qiao, Z.; Jung, J.; Zhu, Y.; Lu, Y.; Zhang, L. L.; MacDonald, A. H.; Ruoff, R. S. Capacitance of Carbon-Based Electrical Double-Layer Capacitors. *Nat. Commun.* **2014**, 5, 3317.

(76.) Trasatti, S.; Petrii, O. A. Real Surface Area Measurements in Electrochemistry. *J. Electroanal. Chem.* **1992**, 327, 353–376.

(77.) Liu, T. -C.; Pell, W. G.; Conway, B. E.; Roberson, S. L. Behavior of Molybdenum Nitrides as Materials for Electrochemical Capacitors Comparison with Ruthenium Oxide. *J. Electrochem. Soc.* **1998**, 145, 1882–1888.

(78.) Ko, J. S.; Sassin, M. B.; Rolison, D. R.; Long, J. W. Deconvolving Double-Layer, Pseudocapacitance, and Battery-like Charge-Storage Mechanisms in Nanoscale LiMn2O4 at 3D Carbon Architectures. *Electrochim. Acta* **2018**, 275, 225–235.

(79.) Aoki, K.; Tokuda, K.; Matsuda, H. Theory of Linear Sweep Voltammetry with Finite Diffusion Space. Part II. Totally Irreversible and Quasi-Reversible Cases. *J. Electroanal. Chem.* **1984**, 160, 33–45.

(80.) Brezesinski, T.; Wang, J.; Polleux, J.; Dunn, B.; Tolbert, S. H. Templated Nanocrystal-Based Porous TiO2 Films for next-Generation Electrochemical Capacitors. *J. Am. Chem. Soc.* **2009**, 131, 1802–1809.

(81.) Brezesinski, T.; Wang, J.; Senter, R.; Brezesinski, K.; Dunn, B.; Tolbert, S. H. On the

Correlation between Mechanical Flexibility, Nanoscale Structure, and Charge Storage in Periodic Mesoporous CeO2 Thin Films. *ACS Nano* **2010**, 4, 967–977.

(82.) Brezesinski, K.; Wang, J.; Haetge, J.; Reitz, C.; Steinmueller, S. O.; Tolbert, S. H.; Smarsly, B. M.; Dunn, B.; Brezesinski, T. Pseudocapacitive Contributions to Charge Storage in Highly Ordered Mesoporous Group v Transition Metal Oxides with Iso-Oriented Layered Nanocrystalline Domains. *J. Am. Chem. Soc.* **2010**, 132, 6982–6990.

(83.) Shao, H.; Lin, Z.; Xu, K.; Taberna, P. L.; Simon, P. Electrochemical Study of Pseudocapacitive Behavior of Ti3C2Tx MXene Material in Aqueous Electrolytes. *Energy Storage Mater.* **2019**, 18, 456–461.

(84.) Opitz, M.; Yue, J.; Wallauer, J.; Smarsly, B.; Roling, B. Mechanisms of Charge Storage in Nanoparticulate TiO2 and Li4Ti5O12 Anodes: New Insights from Scan Rate-Dependent Cyclic Voltammetry. *Electrochim. Acta* **2015**, 168, 125–132.

(85.) Wang, J.; Polleux, J.; Lim, J.; Dunn, B. Pseudocapacitive Contributions to Electrochemical Energy Storage in TiO 2 (Anatase) Nanoparticles. *J. Phys. Chem. C* **2007**, 111, 14925–14931.

(86.) Dupont, M. F.; Donne, S. W. Charge Storage Mechanisms in Electrochemical Capacitors: Effects of Electrode Properties on Performance. *J. Power Sources* **2016**, 326, 613–623.

(87.) Gibson, A. J.; Donne, S. W. A Step Potential Electrochemical Spectroscopy (SPECS) Investigation of Anodically Electrodeposited Thin Films of Manganese Dioxide. *J. Power Sources* **2017**, 359, 520–528.

(88.) Dupont, M. F.; Donne, S. W. A Step Potential Electrochemical Spectroscopy Analysis of Electrochemical Capacitor Electrode Performance. *Electrochim. Acta* **2015**, 167, 268–277.

(89.) Forghani, M.; Donne, S. W. Method Comparison for Deconvoluting Capacitive and Pseudo-Capacitive Contributions to Electrochemical Capacitor Electrode Behavior. *J. Electrochem. Soc.* **2018**, 165, A664–A673.

(90.) Dupont, M. F.; Donne, S. W. Electrolytic Manganese Dioxide Structural and Morphological Effects on Capacitive Performance. *Electrochim. Acta* **2016**, 191, 479–490.

(91.) Munteshari, O.; Zhou, Y.; Mei, B. A.; Pilon, L. Theoretical Validation of the Step Potential Electrochemical Spectroscopy (SPECS) and Multiple Potential Step Chronoamperometry (MUSCA) Methods for Pseudocapacitive Electrodes. *Electrochim. Acta* **2019**, 321, 134648.

(92.) Vogt, H. Note on a Method to Interrelate Inner and Outer Electrode Areas. *Electrochim. Acta* **1994**, 39, 1981–1983.

(93.) Baronetto, D.; Krstajic, N.; Trasatti, S. Reply to "Note on a Method to Interrelate Inner and Outer Electrode Areas" by H. Vogt. *Electrochim. Acta* **1994**, 39, 2359–2362.

(94.) Brett, C. M. A.; Brett, A. M. O. Impedance Methods. In *Electrochem. Princ. methods, Appl.*; **1993**; pp 224–252.

(95.) Miller, J. M.; Dunn, B. Morphology and Electrochemistry of Ruthenium/Carbon Aerogel Nanostructures. *Langmuir* **1999**, 15, 799–806.

(96.) Sugimoto, W.; Iwata, H.; Yokoshima, K.; Murakami, Y.; Takasu, Y. Proton and Electron Conductivity in Hydrous Ruthenium Oxides Evaluated by Electrochemical Impedance Spectroscopy: The Origin of Large Capacitance. *J. Phys. Chem. B* **2005**, 109, 7330–7338.

(97.) Nilson, R. H.; Brumbach, M. T.; Bunker, B. C. Modeling the Electrochemical Impedance Spectra of Electroactive Pseudocapacitor Materials. *J. Electrochem. Soc.* **2011**, 158, A678–A688.

(98.) Bai, L.; Conway, B. E. AC Impedance of Faradaic Reactions Involving Electrosorbed Intermediates: Examination of Conditions Leading to Pseudoinductive Behavior Represented in Three-Dimensional Impedance Spectroscopy Diagrams. *J. Electrochem. Soc.* **1991**, 138, 2897.

(99.) Bai, L.; Conway, B. E. Three-Dimensional Impedance Spectroscopy Diagrams for Processes Involving Electrosorbed Intermediates, Introducing the Third Electrode-Potential Variable-Examination of Conditions Leading to Pseudo-Inductive Behavior. *Electrochim. Acta* **1993**, 38, 1803–1815.

(100.) Ko, J. S.; Sassin, M. B.; Parker, J. F.; Rolison, D. R.; Long, J. W. Combining Battery-like and Pseudocapacitive Charge Storage in 3D MnOx@carbon Electrode Architectures for Zinc-Ion Cells. *Sustain. Energy Fuels* **2018**, 2, 626–636.

(101.) Ko, J. S.; Lai, C.-H.; Long, J. W.; Rolison, D. R.; Dunn, B.; Nelson Weker, J. Differentiating Double-Layer, Psuedocapacitance, and Battery-like Mechanisms by Analyzing Impedance Measurements in Three Dimensions. *ACS Appl. Mater. Interfaces* **2020**, 12, 14071–14078.

(102.) Taberna, P. L.; Simon, P.; Fauvarque, J. F. Electrochemical Characteristics and Impedance Spectroscopy Studies of Carbon-Carbon Supercapacitors. *J. Electrochem. Soc.* **2003**, 150, A292–A300.

(103.) Cole, K. S.; Cole, R. H. Dispersion and Absorption in Dielectrics: II. Direct Current Characteristics. *J. Chem. Phys.* **1942**, 10, 98–105.

(104.) Long, J. W.; Swider, K. E.; Merzbacher, C. I.; Rolison, D. R. Voltammetric Characterization of Ruthenium Oxide-Based Aerogels and Other RuO2 Solids: The Nature of Capacitance in Nanostructured Materials. *Langmuir* **1999**, 15, 780–784.

(105.) Mo, Y.; Antonio, M. R.; Scherson, D. A. In Situ Ru K-Edge X-Ray Absorption Fine Structure Studies of Electroprecipitated Ruthenium Dioxide Films with Relevance to Supercapacitor Applications. *J. Phys. Chem. B* **2000**, 104, 9777–9779.

(106.) Stefan, I. C.; Mo, Y.; Antonio, M. R.; Scherson, D. A. In Situ Ru LII and LIII Edge X-Ray Absorption near Edge Structure of Electrodeposited Ruthenium Dioxide Films. *J. Phys. Chem. B* **2002**, 106, 12373–12375.

(107.) Ozolinš, V.; Zhou, F.; Asta, M. Ruthenia-Based Electrochemical Supercapacitors: Insights from First-Principles Calculations. *Acc. Chem. Res.* **2013**, 46, 1084–1093.

(108.) Chen, Y.; Taylor, P. L.; Scherson, D. Electrochemical and In Situ Optical Studies of Supported Iridium Oxide Films in Aqueous Solutions. *J. Electrochem. Soc.* **2009**, 156, F14–F21.

(109.) Rondinini, S.; Minguzzi, A.; Achilli, E.; Locatelli, C.; Agostini, G.; Pascarelli, S.; Spinolo, G.; Vertova, A.; Ghigna, P. The Dynamics of Pseudocapacitive Phenomena Studied by Energy Dispersive X-Ray Absorption Spectroscopy on Hydrous Iridium Oxide Electrodes in Alkaline Media. *Electrochim. Acta* **2016**, 212, 247–253.

(110.) Mo, Y.; Stefan, I. C.; Cai, W. Bin; Dong, J.; Carey, P.; Scherson, D. A. In Situ Iridium LIII-Edge X-Ray Absorption and Surface Enhanced Raman Spectroscopy of Electrodeposited Iridium Oxide Films in Aqueous Electrolytes. *J. Phys. Chem. B* **2002**, 106, 3681–3686.

(111.) Ghodbane, O.; Pascal, J. L.; Favier, F. Microstructural Effects on Charge-Storage Properties in MnO2-Based Electrochemical Supercapacitors. *ACS Appl. Mater. Interfaces* **2009**, 1, 1130–1139.

(112.) Xiong, P.; Ma, R.; Sakai, N.; Bai, X.; Li, S.; Sasaki, T. Redox Active Cation

Intercalation/Deintercalation in Two-Dimensional Layered MnO2 Nanostructures for High-Rate Electrochemical Energy Storage. *ACS Appl. Mater. Interfaces* **2017**, 9, 6282–6291.

(113.) Brousse, T.; Toupin, M.; Dugas, R.; Athouël, L.; Crosnier, O.; Bélanger, D. Crystalline MnO2 as Possible Alternatives to Amorphous Compounds in Electrochemical Supercapacitors. *J. Electrochem. Soc.* **2006**, 153, A2171.

(114.) Athouel, L.; Arcidiacono, P.; Ramirez-Castro, C.; Crosnier, O.; Guay, D.; Belanger, D.; Brousse, T. Outer and Inner Surface Contribution of Manganese Dioxides Energy Storage Characterization by Cavity Microelectrode Technique. *ECS Trans.* **2014**, 58, 53–59.

(115.) Toupin, M.; Brousse, T.; Bélanger, D. Influence of Microstucture on the Charge Storage Properties of Chemically Synthesized Manganese Dioxide. *Chem. Mater.* **2002**, 14, 3946–3952.

(116.) Toupin, M.; Brousse, T.; Bélanger, D. Charge Storage Mechanism of MnO2 Electrode Used in Aqueous Electrochemical Capacitor. *Chem. Mater.* **2004**, 16, 3184–3190.

(117.) Pang, S.-C.; Anderson, M. A.; Chapman, T. W. Novel Electrode Materials for Thin-Film Ultracapacitors: Comparison of Electrochemical Properties of Sol-Gel-Derived and Electrodeposited Manganese Dioxide. *J. Electrochem. Soc.* **2000**, 147, 444–450.

(118.) Yeager, M.; Du, W.; Si, R.; Su, D.; Marinković, N.; Teng, X. Highly Efficient K0.15MnO2 Birnessite Nanosheets for Stable Pseudocapacitive Cathodes. *J. Phys. Chem. C* **2012**, 116, 20173–20181.

(119.) Chen, D.; Ding, D.; Li, X.; Waller, G. H.; Xiong, X.; El-Sayed, M. A.; Liu, M. Probing the Charge Storage Mechanism of a Pseudocapacitive MnO2 Electrode Using in Operando

Raman Spectroscopy. *Chem. Mater.* **2015**, 27, 6608–6619.

(120.) Hsu, Y. K.; Chen, Y. C.; Lin, Y. G.; Chen, L. C.; Chen, K. H. Reversible Phase Transformation of MnO2 Nanosheets in an Electrochemical Capacitor Investigated by in Situ Raman Spectroscopy. *Chem. Commun.* **2011**, 47, 1252–1254.

(121.) Yang, L.; Cheng, S.; Wang, J.; Ji, X.; Jiang, Y.; Yao, M.; Wu, P.; Wang, M.; Zhou, J.; Liu, M. Investigation into the Origin of High Stability of δ-MnO2 Pseudo-Capacitive Electrode Using Operando Raman Spectroscopy. *Nano Energy* **2016**, 30, 293–302.

(122.) Yang, L.; Cheng, S.; Ji, X.; Jiang, Y.; Zhou, J.; Liu, M. Investigations into the Origin of Pseudocapacitive Behavior of Mn3O4 Electrodes Using in Operando Raman Spectroscopy. *J. Mater. Chem. A* **2015**, 3, 7338–7344.

(123.) Ghodbane, O.; Ataherian, F.; Wu, N. L.; Favier, F. In Situ Crystallographic Investigations of Charge Storage Mechanisms in MnO2-Based Electrochemical Capacitors. *J. Power Sources* **2012**, 206, 454–462.

(124.) Zhan, C.; Lian, C.; Zhang, Y.; Thompson, M. W.; Xie, Y.; Wu, J.; Kent, P. R. C.; Cummings, P. T.; Jiang, D. E.; Wesolowski, D. J. Computational Insights into Materials and Interfaces for Capacitive Energy Storage. *Adv. Sci.* **2017**, 4, 1700059.

(125.) Ibragimova, R.; Puska, M. J.; Komsa, H. P. PH-Dependent Distribution of Functional Groups on Titanium-Based MXenes. *ACS Nano* **2019**, 13, 9171–9181.

(126.) Ulissi, Z. W.; Singh, A. R.; Tsai, C.; Nørskov, J. K. Automated Discovery and Construction of Surface Phase Diagrams Using Machine Learning. *J. Phys. Chem. Lett.* **2016**, 7, 3931–3935.

(127.) Letchworth-Weaver, K.; Arias, T. A. Joint Density Functional Theory of the Electrode-Electrolyte Interface: Application to Fixed Electrode Potentials, Interfacial Capacitances,

and Potentials of Zero Charge. *Phys. Rev. B - Condens. Matter Mater. Phys.* **2012**, 86, 075140.

(128.) Nishihara, S.; Otani, M. Hybrid Solvation Models for Bulk, Interface, and Membrane: Reference Interaction Site Methods Coupled with Density Functional Theory. *Phys. Rev. B* **2017**, 96, 115429.

(129.) Girard, H. L.; Wang, H.; D'Entremont, A.; Pilon, L. Physical Interpretation of Cyclic Voltammetry for Hybrid Pseudocapacitors. *J. Phys. Chem. C* **2015**, 119, 11349–11361.

(130.) Girard, H. L.; Dunn, B.; Pilon, L. Simulations and Interpretation of Three-Electrode Cyclic Voltammograms of Pseudocapacitive Electrodes. *Electrochim. Acta* **2016**, 211, 420–429.

(131.) Girard, H. L.; Wang, H.; D'Entremont, A. L.; Pilon, L. Enhancing Faradaic Charge Storage Contribution in Hybrid Pseudocapacitors. *Electrochim. Acta* **2015**, 182, 639–651.

(132.) Kang, J.; Wei, S. H.; Zhu, K.; Kim, Y. H. First-Principles Theory of Electrochemical Capacitance of Nanostructured Materials: Dipole-Assisted Subsurface Intercalation of Lithium in Pseudocapacitive TiO2 Anatase Nanosheets. *J. Phys. Chem. C* **2011**, 115, 4909–4915.

(133.) Tompsett, D. A.; Parker, S. C.; Bruce, P. G.; Islam, M. S. Nanostructuring of β-MnO2: The Important Role of Surface to Bulk Ion Migration. *Chem. Mater.* **2013**, 25, 536–541.

(134.) Watanabe, E.; Rossmeisl, J.; Björketun, M. E.; Ushiyama, H.; Yamashita, K. Atomic-Scale Analysis of the RuO2/Water Interface under Electrochemical Conditions. *J. Phys. Chem. C* **2016**, 120, 8096–8103.

(135.) Watanabe, E.; Ushiyama, H.; Yamashita, K.; Morikawa, Y.; Asakura, D.; Okubo, M.; Yamada, A. Charge Storage Mechanism of RuO2/Water Interfaces. *J. Phys. Chem. C* **2017**,

121, 18975–18981.

(136.) Zakaryan, H. A.; Kvashnin, A. G.; Oganov, A. R. Stable Reconstruction of the (110) Surface and Its Role in Pseudocapacitance of Rutile-like RuO2. *Sci. Rep.* **2017**, 7, 10357.

(137.) Zhan, C.; Jiang, D. E. Understanding the Pseudocapacitance of RuO2 from Joint Density Functional Theory. *J. Phys. Condens. Matter* **2016**, 28, 464004.

(138.) Keilbart, N.; Okada, Y.; Feehan, A.; Higai, S.; Dabo, I. Quantum-Continuum Simulation of the Electrochemical Response of Pseudocapacitor Electrodes under Realistic Conditions. *Phys. Rev. B* **2017**, 95, 115423.

(139.) Keilbart, N.; Okada, Y.; Dabo, I. Probing the Pseudocapacitance and Energy-Storage Performance of RuO2 Facets from First Principles. *Phys. Rev. Mater.* **2019**, 3, 085405.

(140.) Lindström, H.; Södergren, S.; Solbrand, A.; Rensmo, H.; Hjelm, J.; Hagfeldt, A.; Lindquist, S. E. Li+ Ion Insertion in TiO2 (Anatase). 2. Voltammetry on Nanoporous Films. *J. Phys. Chem. B* **1997**, 101, 7717–7722.

(141.) Marchand, R.; Brohan, L.; Tournoux, M. TiO2(B) a New Form of Titanium Dioxide and the Potassium Octatitanate K2Ti8O17. *Mater. Res. Bull.* **1980**, 15, 1129–1133.

(142.) Tournoux, M.; Marchand, R.; Brohan, L. Layered K2Ti4O9 and the Open Metastable TiO2(B) Structure. *Prog. Solid State Chem.* **1986**, 17, 33–52.

(143.) Feist, T. P.; Davies, P. K. The Soft Chemical Synthesis of TiO2(B) from Layered Titanates. *J. Solid State Chem.* **1992**, 101, 275–295.

(144.) Dalton, A. S.; Belak, A. A.; Van Der Ven, A. Thermodynamics of Lithium in TiO2(B) from First Principles. *Chem. Mater.* **2012**, 24, 1568–1574.

(145.) Armstrong, A. R.; Armstrong, G.; Canales, J.; Bruce, P. G. TiO2(B) Nanowires as Negative

Electrodes for Rechargeable Lithium Batteries. *J. Power Sources* **2005**, 146, 501–506.

(146.) Armstrong, G.; Armstrong, A. R.; Canales, J.; Bruce, P. G. TiO2(B) Nanotubes as Negative Electrodes for Rechargeable Lithium Batteries. *Electrochem. Solid-State Lett.* **2006**, 9, A139–A143.

(147.) Brutti, S.; Gentili, V.; Menard, H.; Scrosati, B.; Bruce, P. G. TiO2-(B) Nanotubes as Anodes for Lithium Batteries: Origin and Mitigation of Irreversible Capacity. *Adv. Energy Mater.* **2012**, 2, 322–327.

(148.) Dylla, A. G.; Henkelman, G.; Stevenson, K. J. Lithium Insertion in Nanostructured TiO2(B) Architectures. *Acc. Chem. Res.* **2013**, 46, 1104–1112.

(149.) Brohan, L.; Marchand, R. Properties Physiques Des Bronzes MxTiO2(B). *Solid State Ionics* **1983**, 9–10, 419–424.

(150.) Arrouvel, C.; Parker, S. C.; Saiful Islam, M. Lithium Insertion and Transport in the TiO2(B) Anode Material: A Computational Study. *Chem. Mater.* **2009**, 21, 4778–4783.

(151.) Koudriachova, M. V. Role of the Surface in Li Insertion into Nanowires of TiO2-B. *Surf. Interface Anal.* **2010**, 42, 1330–1332.

(152.) Okumura, T.; Fukutsuka, T.; Yanagihara, A.; Orikasa, Y.; Arai, H.; Ogumi, Z.; Uchimoto, Y. Electronic and Local Structural Changes with Lithium-Ion Insertion in TiO2-B: X-Ray Absorption Spectroscopy Study. *J. Mater. Chem.* **2011**, 21, 15369–15377.

(153.) Dylla, A. G.; Xiao, P.; Henkelman, G.; Stevenson, K. J. Morphological Dependence of Lithium Insertion in Nanocrystalline TiO2(B) Nanoparticles and Nanosheets. *J. Phys. Chem. Lett.* **2012**, 3, 2015–2019.

(154.) Hua, X.; Liu, Z.; Fischer, M. G.; Borkiewicz, O.; Chupas, P. J.; Chapman, K. W.; Steiner, U.;

Bruce, P. G.; Grey, C. P. Lithiation Thermodynamics and Kinetics of the TiO2(B) Nanoparticles. *J. Am. Chem. Soc.* **2017**, 139, 13330–13341.

(155.) Reichman, B.; Bard, A. J. The Application of Nb2O5 as a Cathode in Nonaqueous Lithium Cells. *J. Electrochem. Soc.* **1981**, 128, 344–346.

(156.) Kumagai, N.; Tanno, K.; Nakajima, T.; Watanabe, N. Structural Changes of Nb2O5 and V2O5 as Rechargeable Cathodes for Lithium Battery. *Electrochim. Acta* **1983**, 28, 17–22.

(157.) Kumagai, N.; Ishiyama, I.; Tanno, K. Electrochemical and Structural Characteristics of Niobium(V) Oxide in a Rechargeable Lithium Battery. *J. Power Sources* **1987**, 20, 193–198.

(158.) Ohzuku, T.; Sawai, K.; Hirai, T. Electrochemistry of L-Niobium Pentoxide a Lithium/Non-Aqueous Cell. *J. Power Sources* **1987**, 19, 287–299.

(159.) Kodama, R.; Terada, Y.; Nakai, I.; Komaba, S.; Kumagai, N. Electrochemical and In Situ XAFS-XRD Investigation of Nb2O5 for Rechargeable Lithium Batteries. *J. Electrochem. Soc.* **2006**, 153, A583–A588.

(160.) Kim, J. W.; Augustyn, V.; Dunn, B. The Effect of Crystallinity on the Rapid Pseudocapacitive Response of Nb2O5. *Adv. Energy Mater.* **2012**, 2, 141–148.

(161.) Griffith, K. J.; Forse, A. C.; Griffin, J. M.; Grey, C. P. High-Rate Intercalation without Nanostructuring in Metastable Nb2O5 Bronze Phases. *J. Am. Chem. Soc.* **2016**, 138, 8888–8899.

(162.) Liu, C.-P.; Zhou, F.; Ozolins, V. First Principles Study for Lithium Intercalation and Diffusion Behavior in Orthorhombic Nb2O5 Electrochemical Supercapacitor. In *Bull. Am. Phys. Soc.*; **2012**.

(163.) Lubimtsev, A. A.; Kent, P. R. C.; Sumpter, B. G.; Ganesh, P. Understanding the Origin of

High-Rate Intercalation Pseudocapacitance in Nb2O5 Crystals. *J. Mater. Chem. A* **2013**, 1, 14951–14956.

(164.) Chen, D.; Wang, J. H.; Chou, T. F.; Zhao, B.; El-Sayed, M. A.; Liu, M. Unraveling the Nature of Anomalously Fast Energy Storage in T-Nb2O5. *J. Am. Chem. Soc.* **2017**, 139, 7071–7081.

(165.) Tolosa, A.; Krüner, B.; Fleischmann, S.; Jäckel, N.; Zeiger, M.; Aslan, M.; Grobelsek, I.; Presser, V. Niobium Carbide Nanofibers as a Versatile Precursor for High Power Supercapacitor and High Energy Battery Electrodes. *J. Mater. Chem. A* **2016**, 4, 16003–16016.

(166.) Tolosa, A.; Fleischmann, S.; Grobelsek, I.; Quade, A.; Lim, E.; Presser, V. Binder-Free Hybrid Titanium–Niobium Oxide/Carbon Nanofiber Mats for Lithium-Ion Battery Electrodes. *ChemSusChem* **2018**, 11, 159–170.

(167.) Lai, C. H.; Ashby, D.; Moz, M.; Gogotsi, Y.; Pilon, L.; Dunn, B. Designing Pseudocapacitance for Nb2O5/Carbide-Derived Carbon Electrodes and Hybrid Devices. *Langmuir* **2017**, 33, 9407–9415.

(168.) Zhang, S.; Liu, G.; Qiao, W.; Wang, J.; Ling, L. Oxygen Vacancies Enhance the Lithium Ion Intercalation Pseudocapacitive Properties of Orthorhombic Niobium Pentoxide. *J. Colloid Interface Sci.* **2020**, 562, 193–203.

(169.) Bockris, J. O. M.; Otagawa, T. Mechanism of Oxygen Evolution on Perovskites. *J. Phys. Chem.* **1983**, 87, 2960–2971.

(170.) Ishihara, T. *Perovskite Oxide for Solid Oxide Fuel Cells*; Springer Science & Business Media, **2002**.

(171.) Kudo, T. Electrochemical Behavior of the Perovskite-Type Nd1−xSrxCoO3 in an Aqueous

Alkaline Solution. *J. Electrochem. Soc.* **1975**, 122, 159.

(172.) Wilde, P. M.; Guther, T. J.; Oesten, R.; Garche, J. Strontium Ruthenate Perovskite as the Active Material for Supercapacitors. *J. Electroanal. Chem.* **1999**, 461, 154–160.

(173.) Wohlfahrt-Mehrens, M.; Schenk, J.; Wilde, P. M.; Abdelmula, E.; Axmann, P.; Garche, J. New Materials for Supercapacitors. *J. Power Sources* **2002**, 105, 182–188.

(174.) Karvonen, L.; Valkeapää, M.; Liu, R. S.; Chen, J. M.; Yamauchi, H.; Karppinen, M. O-K and Co-L XANES Study on Oxygen Intercalation in Parasite SrCoO3-δ. *Chem. Mater.* **2010**, 22, 70–76.

(175.) Mefford, J. T.; Hardin, W. G.; Dai, S.; Johnston, K. P.; Stevenson, K. J. Anion Charge Storage through Oxygen Intercalation in LaMnO3 Perovskite Pseudocapacitor Electrodes. *Nat. Mater.* **2014**, 13, 726–732.

(176.) Zhu, L.; Liu, Y.; Su, C.; Zhou, W.; Liu, M.; Shao, Z. Perovskite SrCo0.9Nb0.1O3−δ as an Anion-Intercalated Electrode Material for Supercapacitors with Ultrahigh Volumetric Energy Density. *Angew. Chemie - Int. Ed.* **2016**, 55, 9576–9579.

(177.) Liu, Y.; Wang, Z.; Veder, J. P. M.; Xu, Z.; Zhong, Y.; Zhou, W.; Tade, M. O.; Wang, S.; Shao, Z. Highly Defective Layered Double Perovskite Oxide for Efficient Energy Storage via Reversible Pseudocapacitive Oxygen-Anion Intercalation. *Adv. Energy Mater.* **2018**, 8, 1702604.

(178.) Naguib, M.; Mashtalir, O.; Carle, J.; Presser, V.; Lu, J.; Hultman, L.; Gogotsi, Y.; Barsoum, M. W. Two-Dimensional Transition Metal Carbides. *ACS Nano* **2012**, 6, 1322–1331.

(179.) Anasori, B.; Lukatskaya, M. R.; Gogotsi, Y. 2D Metal Carbides and Nitrides (MXenes) for Energy Storage. *Nat. Rev. Mater.* **2017**, 2, 16098.

(180.) Ng, V. M. H.; Huang, H.; Zhou, K.; Lee, P. S.; Que, W.; Xu, J. Z.; Kong, L. B.; Hong Ng, V. M.; Huang, H.; Zhou, K.; Lee, P. S.; Que, W.; Xu, J. Z.; Kong, L. B. Recent Progress in Layered Transition Metal Carbides and/or Nitrides (MXenes) and Their Composites: Synthesis and Applications. *J. Mater. Chem. A* **2017**, 5, 3039–3068.

(181.) Deysher, G.; Shuck, C. E.; Hantanasirisakul, K.; Frey, N. C.; Foucher, A. C.; Maleski, K.; Sarycheva, A.; Shenoy, V. B.; Stach, E. A.; Anasori, B.; Gogotsi, Y. Synthesis of Mo4VAlC4 MAX Phase and Two-Dimensional Mo4VC4 MXene with Five Atomic Layers of Transition Metals. *ACS Nano* **2020**, 14, 204–217.

(182.) Ghidiu, M.; Lukatskaya, M. R.; Zhao, M. Q.; Gogotsi, Y.; Barsoum, M. W. Conductive Two-Dimensional Titanium Carbide "clay" with High Volumetric Capacitance. *Nature* **2015**, 516, 78–81.

(183.) Naguib, M.; Mochalin, V. N.; Barsoum, M. W.; Gogotsi, Y. 25th Anniversary Article: MXenes: A New Family of Two-Dimensional Materials. *Adv. Mater.* **2014**, 26, 992–1005.

(184.) Li, Y.; Shao, H.; Lin, Z.; Lu, J.; Liu, L.; Duployer, B.; Persson, P. O. Å.; Eklund, P.; Hultman, L.; Li, M.; Chen, K.; Zha, X. H.; Du, S.; Rozier, P.; Chai, Z.; Raymundo-Piñero, E.; Taberna, P. L.; Simon, P.; Huang, Q. A General Lewis Acidic Etching Route for Preparing MXenes with Enhanced Electrochemical Performance in Non-Aqueous Electrolyte. *Nat. Mater.* **2020**, DOI: 10.1038/s41563-020-0657-0.

(185.) Naguib, M.; Come, J.; Dyatkin, B.; Presser, V.; Taberna, P. L.; Simon, P.; Barsoum, M. W.; Gogotsi, Y. MXene: A Promising Transition Metal Carbide Anode for Lithium-Ion Batteries. *Electrochem. commun.* **2012**, 16, 61–64.

(186.) Lin, Z.; Barbara, D.; Taberna, P. L.; Van Aken, K. L.; Anasori, B.; Gogotsi, Y.; Simon, P.

Capacitance of Ti3C2Tx MXene in Ionic Liquid Electrolyte. *J. Power Sources* **2016**, 326, 575–579.

(187.) Jiang, Q.; Kurra, N.; Alhabeb, M.; Gogotsi, Y.; Alshareef, H. N. All Pseudocapacitive MXene-RuO2 Asymmetric Supercapacitors. *Adv. Energy Mater.* **2018**, 8, 1703043.

(188.) Srimuk, P.; Kaasik, F.; Krüner, B.; Tolosa, A.; Fleischmann, S.; Jäckel, N.; Tekeli, M. C.; Aslan, M.; Suss, M. E.; Presser, V. MXene as a Novel Intercalation-Type Pseudocapacitive Cathode and Anode for Capacitive Deionization. *J. Mater. Chem. A* **2016**, 4, 18265–18271.

(189.) Gao, G.; O'Mullane, A. P.; Du, A. 2D MXenes: A New Family of Promising Catalysts for the Hydrogen Evolution Reaction. *ACS Catal.* **2017**, 7, 494–500.

(190.) Wang, H. W.; Naguib, M.; Page, K.; Wesolowski, D. J.; Gogotsi, Y. Resolving the Structure of Ti3C2Tx MXenes through Multilevel Structural Modeling of the Atomic Pair Distribution Function. *Chem. Mater.* **2016**, 28, 349–359.

(191.) Alhabeb, M.; Maleski, K.; Anasori, B.; Lelyukh, P.; Clark, L.; Sin, S.; Gogotsi, Y. Guidelines for Synthesis and Processing of Two-Dimensional Titanium Carbide (Ti3C2Tx MXene). *Chem. Mater.* **2017**, 29, 7633–7644.

(192.) Okubo, M.; Sugahara, A.; Kajiyama, S.; Yamada, A. MXene as a Charge Storage Host. *Acc. Chem. Res.* **2018**, 51, 591–599.

(193.) Lukatskaya, M. R.; Mashtalir, O.; Ren, C. E.; Dall'Agnese, Y.; Rozier, P.; Taberna, P. L.; Naguib, M.; Simon, P.; Barsoum, M. W.; Gogotsi, Y. Cation Intercalation and High Volumetric Capacitance of Two-Dimensional Titanium Carbide. *Science* **2013**, 341, 1502–1505.

(194.) Dall'Agnese, Y.; Lukatskaya, M. R.; Cook, K. M.; Taberna, P. L.; Gogotsi, Y.; Simon, P. High

Capacitance of Surface-Modified 2D Titanium Carbide in Acidic Electrolyte. *Electrochem. commun.* **2014**, 48, 118–122.

(195.) Lukatskaya, M. R.; Bak, S. M.; Yu, X.; Yang, X. Q.; Barsoum, M. W.; Gogotsi, Y. Probing the Mechanism of High Capacitance in 2D Titanium Carbide Using in Situ X-Ray Absorption Spectroscopy. *Adv. Energy Mater.* **2015**, 5, 1500589.

(196.) Hu, M.; Li, Z.; Hu, T.; Zhu, S.; Zhang, C.; Wang, X. High-Capacitance Mechanism for Ti3C2Tx MXene by in Situ Electrochemical Raman Spectroscopy Investigation. *ACS Nano* **2016**, 10, 11344–11350.

(197.) Sun, Y.; Zhan, C.; Kent, P. R. C.; Naguib, M.; Gogotsi, Y.; Jiang, D. E. Proton Redox and Transport in MXene-Confined Water. *ACS Appl. Mater. Interfaces* **2020**, 12, 763–770.

(198.) Kajiyama, S.; Szabova, L.; Iinuma, H.; Sugahara, A.; Gotoh, K.; Sodeyama, K.; Tateyama, Y.; Okubo, M.; Yamada, A. Enhanced Li-Ion Accessibility in MXene Titanium Carbide by Steric Chloride Termination. *Adv. Energy Mater.* **2017**, 7, 1601873.

(199.) Kajiyama, S.; Szabova, L.; Sodeyama, K.; Iinuma, H.; Morita, R.; Gotoh, K.; Tateyama, Y.; Okubo, M.; Yamada, A. Sodium-Ion Intercalation Mechanism in MXene Nanosheets. *ACS Nano* **2016**, 10, 3334–3341.

(200.) Dall'Agnese, Y.; Taberna, P. L.; Gogotsi, Y.; Simon, P. Two-Dimensional Vanadium Carbide (MXene) as Positive Electrode for Sodium-Ion Capacitors. *J. Phys. Chem. Lett.* **2015**, 6, 2305–2309.

(201.) Xie, Y.; Naguib, M.; Mochalin, V. N.; Barsoum, M. W.; Gogotsi, Y.; Yu, X.; Nam, K. W.; Yang, X. Q.; Kolesnikov, A. I.; Kent, P. R. C. Role of Surface Structure on Li-Ion Energy Storage Capacity of Two-Dimensional Transition-Metal Carbides. *J. Am. Chem. Soc.* **2014**, 136,

6385–6394.

(202.) Wang, X.; Mathis, T. S.; Li, K.; Lin, Z.; Vlcek, L.; Torita, T.; Osti, N. C.; Hatter, C.; Urbankowski, P.; Sarycheva, A.; Tyagi, M.; Mamontov, E.; Simon, P.; Gogotsi, Y. Influences from Solvents on Charge Storage in Titanium Carbide MXenes. *Nat. Energy* **2019**, 4, 241–248.

(203.) Wang, X.; Kajiyama, S.; Iinuma, H.; Hosono, E.; Oro, S.; Moriguchi, I.; Okubo, M.; Yamada, A. Pseudocapacitance of MXene Nanosheets for High-Power Sodium-Ion Hybrid Capacitors. *Nat. Commun.* **2015**, 6, 6544.

(204.) Ji, X.; Xu, K.; Chen, C.; Zhang, B.; Ruan, Y.; Liu, J.; Miao, L.; Jiang, J. Probing the Electrochemical Capacitance of MXene Nanosheets for High-Performance Pseudocapacitors. *Phys. Chem. Chem. Phys.* **2016**, 18, 4460–4467.

(205.) Wang, L.; Wang, J.; Zhang, Z.; Wang, L.; Wang, W.; Liu, J.; Hong, Z.; Cho, K.; Wang, W. Origin of Theoretical Pseudocapacitance of Two-Dimensional Supercapacitor Electrodes Ti3C2T2 (T = Bare, O, S). *J. Mater. Chem. A* **2019**, 7, 16231–16238.

(206.) Yang, Y.; Hantanasirisakul, K.; Frey, N. C.; Anasori, B.; Green, R. J. Distinguishing Electronic Contributions of Surface and Sub-Surface Transition Metal Atoms in Ti-Based Distinguishing Electronic Contributions of Surface and Sub-Surface Transition Metal Atoms in Ti-Based MXenes. *2D Mater.* **2020**, 7, 025015.

(207.) Zhan, C.; Naguib, M.; Lukatskaya, M.; Kent, P. R. C.; Gogotsi, Y.; Jiang, D. E. Understanding the MXene Pseudocapacitance. *J. Phys. Chem. Lett.* **2018**, 9, 1223–1228.

(208.) Zhan, C.; Sun, W.; Kent, P. R. C.; Naguib, M.; Gogotsi, Y.; Jiang, D. E. Computational Screening of MXene Electrodes for Pseudocapacitive Energy Storage. *J. Phys. Chem. C*

2019, 123, 315–321.

(209.) Sugahara, A.; Ando, Y.; Kajiyama, S.; Yazawa, K.; Gotoh, K.; Otani, M.; Okubo, M.; Yamada, A. Negative Dielectric Constant of Water Confined in Nanosheets. *Nat. Commun.* **2019**, 10, 850.

(210.) Cook, J. B.; Kim, H. S.; Yan, Y.; Ko, J. S.; Robbennolt, S.; Dunn, B.; Tolbert, S. H. Mesoporous MoS2 as a Transition Metal Dichalcogenide Exhibiting Pseudocapacitive Li and Na-Ion Charge Storage. *Adv. Energy Mater.* **2016**, 6, 1501937.

(211.) Cook, J. B.; Lin, T. C.; Kim, H. S.; Siordia, A.; Dunn, B. S.; Tolbert, S. H. Suppression of Electrochemically Driven Phase Transitions in Nanostructured MoS2 Pseudocapacitors Probed Using Operando X-Ray Diffraction. *ACS Nano* **2019**, 13, 1223–1231.

(212.) Ihsan, M.; Meng, Q.; Li, L.; Li, D.; Wang, H.; Seng, K. H.; Chen, Z.; Kennedy, S. J.; Guo, Z.; Liu, H. K. V2O5/Mesoporous Carbon Composite as a Cathode Material for Lithium-Ion Batteries. *Electrochim. Acta* **2015**, 173, 172–177.

(213.) Lan, K.; Wei, Q.; Wang, R.; Xia, Y.; Tan, S.; Wang, Y.; Elzatahry, A.; Feng, P.; Mai, L.; Zhao, D. Two-Dimensional Mesoporous Heterostructure Delivering Superior Pseudocapacitive Sodium Storage via Bottom-Up Monomicelle Assembly. *J. Am. Chem. Soc.* **2019**, 141, 16755–16762.

(214.) Muller, G. A.; Cook, J. B.; Kim, H. S.; Tolbert, S. H.; Dunn, B. High Performance Pseudocapacitor Based on 2D Layered Metal Chalcogenide Nanocrystals. *Nano Lett.* **2015**, 15, 1911–1917.

(215.) Acerce, M.; Voiry, D.; Chhowalla, M. Metallic 1T Phase MoS2 Nanosheets as Supercapacitor Electrode Materials. *Nat. Nanotechnol.* **2015**, 10, 313–318.

(216.) Bissett, M. A.; Kinloch, I. A.; Dryfe, R. A. W. Characterization of MoS2-Graphene Composites for High-Performance Coin Cell Supercapacitors. *ACS Appl. Mater. Interfaces* **2015**, 7, 17388–17398.

(217.) Bissett, M. A.; Worrall, S. D.; Kinloch, I. A.; Dryfe, R. A. W. Comparison of Two-Dimensional Transition Metal Dichalcogenides for Electrochemical Supercapacitors. *Electrochim. Acta* **2016**, 201, 30–37.

(218.) Savjani, N.; Lewis, E. A.; Bissett, M. A.; Brent, J. R.; Dryfe, R. A. W.; Haigh, S. J.; O'Brien, P. Synthesis of Lateral Size-Controlled Monolayer 1H-MoS2@Oleylamine as Supercapacitor Electrodes. *Chem. Mater.* **2016**, 28, 657–664.

(219.) Yang, Y.; Fei, H.; Ruan, G.; Xiang, C.; Tour, J. M. Edge-Oriented MoS2 Nanoporous Films as Flexible Electrodes for Hydrogen Evolution Reactions and Supercapacitor Devices. *Adv. Mater.* **2014**, 26, 8163–8168.

(220.) Liu, C.; Yu, Z.; Neff, D.; Zhamu, A.; Jang, B. Z. Graphene-Based Supercapacitor with an Ultrahigh Energy Density. *Nano Lett.* **2010**, 10, 4863–4868.

(221.) He, Y.; Zhang, Y.; Li, X.; Lv, Z.; Wang, X.; Liu, Z.; Huang, X. Capacitive Mechanism of Oxygen Functional Groups on Carbon Surface in Supercapacitors. *Electrochim. Acta* **2018**, 282, 618–625.

(222.) Zhang, L. L.; Zhao, X.; Ji, H.; Stoller, M. D.; Lai, L.; Murali, S.; McDonnell, S.; Cleveger, B.; Wallace, R. M.; Ruoff, R. S. Nitrogen Doping of Graphene and Its Effect on Quantum Capacitance, and a New Insight on the Enhanced Capacitance of N-Doped Carbon. *Energy Environ. Sci.* **2012**, 5, 9618–9625.

(223.) Zhao, Y.; Wang, X.; Wang, N.; Li, M.; Li, Q.; Liu, J. Unraveling Factors Leading to High

Pseudocapacitance of Redox-Active Small Aromatics on Graphene. *J. Phys. Chem. C* **2019**, 123, 994–1002.

(224.) Chen, B.; Wu, W.; Li, C.; Wang, Y.; Zhang, Y.; Fu, L.; Zhu, Y.; Zhang, L.; Wu, Y. Oxygen/Phosphorus Co-Doped Porous Carbon from Cicada Slough as High-Performance Electrode Material for Supercapacitors. *Sci. Rep.* **2019**, 9, 5431.

(225.) Yang, D.; Song, Y.; Ye, Y. J.; Zhang, M.; Sun, X.; Liu, X. X. Boosting the Pseudocapacitance of Nitrogen-Rich Carbon Nanorod Arrays for Electrochemical Capacitors. *J. Mater. Chem. A* **2019**, 7, 12086–12094.

(226.) Le Comte, A.; Chhin, D.; Gagnon, A.; Retoux, R.; Brousse, T.; Bélanger, D. Spontaneous Grafting of 9,10-Phenanthrenequinone on Porous Carbon as an Active Electrode Material in an Electrochemical Capacitor in an Alkaline Electrolyte. *J. Mater. Chem. A* **2015**, 3, 6146–6156.

(227.) Pognon, G.; Cougnon, C.; Mayilukila, D.; Bélanger, D. Catechol-Modified Activated Carbon Prepared by the Diazonium Chemistry for Application as Active Electrode Material in Electrochemical Capacitor. *ACS Appl. Mater. Interfaces* **2012**, 4, 3788–3796.

(228.) He, Y.; Yang, X.; An, N.; Wang, X.; Yang, Y.; Hu, Z. Covalently Functionalized Heterostructured Carbon by Redox-Active p-Phenylenediamine Molecules for High-Performance Symmetric Supercapacitors. *New J. Chem.* **2019**, 43, 1688–1698.

(229.) James, S. L. Metal-Organic Frameworks. *Chem. Soc. Rev.* **2003**, 32, 276–288.

(230.) Stassen, I.; Burtch, N.; Talin, A.; Falcaro, P.; Allendorf, M.; Ameloot, R. An Updated Roadmap for the Integration of Metal-Organic Frameworks with Electronic Devices and Chemical Sensors. *Chem. Soc. Rev.* **2017**, 46, 3185–3241.

(231.) Liu, J.; Zhou, Y.; Xie, Z.; Li, Y.; Liu, Y.; Sun, J.; Ma, Y.; Terasaki, O.; Chen, L. Conjugated Copper–Catecholate Framework Electrodes for Efficient Energy Storage. *Angew. Chemie - Int. Ed.* **2020**, 59, 1081–1086.

(232.) Feng, D.; Lei, T.; Lukatskaya, M. R.; Park, J.; Huang, Z.; Lee, M.; Shaw, L.; Chen, S.; Yakovenko, A. A.; Kulkarni, A.; Xiao, J.; Fredrickson, K.; Tok, J. B.; Zou, X.; Cui, Y.; Bao, Z. Robust and Conductive Two-Dimensional Metal-Organic Frameworks with Exceptionally High Volumetric and Areal Capacitance. *Nat. Energy* **2018**, 3, 30–36.

(233.) Sheberla, D.; Bachman, J. C.; Elias, J. S.; Sun, C. J.; Shao-Horn, Y.; Dincă, M. Conductive MOF Electrodes for Stable Supercapacitors with High Areal Capacitance. *Nat. Mater.* **2017**, 16, 220–224.

(234.) Pasta, M.; Wessells, C. D.; Liu, N.; Nelson, J.; Mcdowell, M. T.; Huggins, R. A.; Toney, M. F.; Cui, Y. Full Open-Framework Batteries for Stationary Energy Storage. *Nat. Commun.* **2014**, 5, 3007.

(235.) Wu, X.; Hong, J. J.; Shin, W.; Ma, L.; Liu, T.; Bi, X.; Yuan, Y.; Qi, Y.; Surta, T. W.; Huang, W.; Neuefeind, J.; Wu, T.; Greaney, P. A.; Lu, J.; Ji, X. Diffusion-Free Grotthuss Topochemistry for High-Rate and Long-Life Proton Batteries. *Nat. Energy* **2019**, 4, 123–130.

(236.) Jia, H.; Wang, Z.; Zheng, X.; Cai, Y.; Lin, J.; Liang, H.; Qi, J.; Cao, J.; Feng, J.; Fei, W. Controlled Synthesis of MOF-Derived Quadruple-Shelled CoS2 Hollow Dodecahedrons as Enhanced Electrodes for Supercapacitors. *Electrochim. Acta* **2019**, 312, 54–61.

(237.) Fleischmann, S.; Jäckel, N.; Zeiger, M.; Krüner, B.; Grobelsek, I.; Formanek, P.; Choudhury, S.; Weingarth, D.; Presser, V. Enhanced Electrochemical Energy Storage by Nanoscopic Decoration of Endohedral and Exohedral Carbon with Vanadium Oxide via Atomic Layer

Deposition. *Chem. Mater.* **2016**, 28, 2802–2813.

(238.) Fleischmann, S.; Leistenschneider, D.; Lemkova, V.; Krüner, B.; Zeiger, M.; Borchardt, L.; Presser, V. Tailored Mesoporous Carbon/Vanadium Pentoxide Hybrid Electrodes for High Power Pseudocapacitive Lithium and Sodium Intercalation. *Chem. Mater.* **2017**, 29, 8653–8662.

(239.) Fleischmann, S.; Zeiger, M.; Jäckel, N.; Krüner, B.; Lemkova, V.; Widmaier, M.; Presser, V. Tuning Pseudocapacitive and Battery-like Lithium Intercalation in Vanadium Dioxide/Carbon Onion Hybrids for Asymmetric Supercapacitor Anodes. *J. Mater. Chem. A* **2017**, 5, 13039–13051.

(240.) Naoi, K.; Kurita, T.; Abe, M.; Furuhashi, T.; Abe, Y.; Okazaki, K.; Miyamoto, J.; Iwama, E.; Aoyagi, S.; Naoi, W.; Simon, P. Ultrafast Nanocrystalline-TiO2(B)/Carbon Nanotube Hyperdispersion Prepared via Combined Ultracentrifugation and Hydrothermal Treatments for Hybrid Supercapacitors. *Adv. Mater.* **2016**, 28, 6751–6757.

(241.) Iwama, E.; Kawabata, N.; Nishio, N.; Kisu, K.; Miyamoto, J.; Naoi, W.; Rozier, P.; Simon, P.; Naoi, K. Enhanced Electrochemical Performance of Ultracentrifugation-Derived Nc-Li3VO4/MWCNT Composites for Hybrid Supercapacitors. *ACS Nano* **2016**, 10, 5398–5404.

(242.) Amisse, R.; Sougrati, M. T.; Stievano, L.; Davoisne, C.; Dražič, G.; Budič, B.; Dominko, R.; Masquelier, C. Singular Structural and Electrochemical Properties in Highly Defective LiFePO4 Powders. *Chem. Mater.* **2015**, 27, 4261–4273.

(243.) Kim, H.-S.; Cook, J. B.; Tolbert, S. H.; Dunn, B. The Development of Pseudocapacitive Properties in Nanosized-MoO2. *J. Electrochem. Soc.* **2015**, 162, A5083–A5090.

(244.) Gogotsi, Y.; Simon, P. True Performance Metrics in Electrochemical Energy Storage.

Science **2011**, 334, 917–918.

(245.) Fleischmann, S.; Tolosa, A.; Presser, V. Design of Carbon/Metal Oxide Hybrids for Electrochemical Energy Storage. *Chem. - A Eur. J.* **2018**, 24, 12143–12153.

(246.) Sun, H.; Mei, L.; Liang, J.; Zhao, Z.; Lee, C.; Fei, H.; Ding, M.; Lau, J.; Li, M.; Wang, C.; Xu, X.; Hao, G.; Papandrea, B.; Shakir, I.; Dunn, B.; Huang, Y.; Duan, X. Three-Dimensional Holey-Graphene/Niobia Composite Architectures for Ultrahigh-Rate Energy Storage. *Science* **2017**, 356, 599–604.

(247.) Sun, H.; Zhu, J.; Baumann, D.; Peng, L.; Xu, Y.; Shakir, I.; Huang, Y.; Duan, X. Hierarchical 3D Electrodes for Electrochemical Energy Storage. *Nat. Rev. Mater.* **2019**, 4, 45–60.

(248.) Cook, J. B.; Kim, H. S.; Lin, T. C.; Lai, C. H.; Dunn, B.; Tolbert, S. H. Pseudocapacitive Charge Storage in Thick Composite MoS2 Nanocrystal-Based Electrodes. *Adv. Energy Mater.* **2017**, 7, 1601283.

(249.) Wang, Y.; Li, H.; He, P.; Hosono, E.; Zhou, H. Nano Active Materials for Lithium-Ion Batteries. *Nanoscale* **2010**, 2, 1294–1305.

(250.) Mofarah, S. S.; Adabifiroozjaei, E.; Yao, Y.; Koshy, P.; Lim, S.; Webster, R.; Liu, X.; Khayyam Nekouei, R.; Cazorla, C.; Liu, Z.; Wang, Y.; Lambropoulos, N.; Sorrell, C. C. Proton-Assisted Creation of Controllable Volumetric Oxygen Vacancies in Ultrathin CeO2−x for Pseudocapacitive Energy Storage Applications. *Nat. Commun.* **2019**, 10, 2594.

(251.) Tao, Q.; Dahlqvist, M.; Lu, J.; Kota, S.; Meshkian, R.; Halim, J.; Palisaitis, J.; Hultman, L.; Barsoum, M. W.; Persson, P. O. Å.; Rosen, J. Two-Dimensional Mo1.33C MXene with Divacancy Ordering Prepared from Parent 3D Laminate with in-Plane Chemical Ordering. *Nat. Commun.* **2017**, 8, 14949.

(252.) Kang, J.; Hirata, A.; Kang, L.; Zhang, X.; Hou, Y.; Chen, L.; Li, C.; Fujita, T.; Akagi, K.; Chen, M. Enhanced Supercapacitor Performance of MnO2 by Atomic Doping. *Angew. Chemie - Int. Ed.* **2013**, 52, 1664–1667.

(253.) Yan, L.; Niu, L.; Shen, C.; Zhang, Z.; Lin, J.; Shen, F.; Gong, Y.; Li, C.; Liu, X.; Xu, S. Modulating the Electronic Structure and Pseudocapacitance of δ-MnO 2 through Transitional Metal M (M = Fe, Co and Ni) Doping. *Electrochim. Acta* **2019**, 306, 529–540.

(254.) Chervin, C. N.; Ko, J. S.; Miller, B. W.; Dudek, L.; Mansour, A. N.; Donakowski, M. D.; Brintlinger, T.; Gogotsi, P.; Chattopadhyay, S.; Shibata, T.; Parker, J. F.; Hahn, B. P.; Rolison, D. R.; Long, J. W. Defective by Design: Vanadium-Substituted Iron Oxide Nanoarchitectures as Cation-Insertion Hosts for Electrochemical Charge Storage. *J. Mater. Chem. A* **2015**, 3, 12059–12068.

(255.) Dieterle, M.; Weinberg, G.; Mestl, G. Raman Spectroscopy of Molybdenum Oxides - Part I. Structural Characterization of Oxygen Defects in MoO3-x by DR UV/VIS, Raman Spectroscopy and X-Ray Diffraction. *Phys. Chem. Chem. Phys.* **2002**, 4, 812–821.

(256.) Durham, J. L.; Poyraz, A. S.; Takeuchi, E. S.; Marschilok, A. C.; Takeuchi, K. J. Impact of Multifunctional Bimetallic Materials on Lithium Battery Electrochemistry. *Acc. Chem. Res.* **2016**, 49, 1864–1872.

(257.) Augustyn, V.; Gogotsi, Y. 2D Materials with Nanoconfined Fluids for Electrochemical Energy Storage. *Joule* **2017**, 1, 443–452.

(258.) Augustyn, V. Tuning the Interlayer of Transition Metal Oxides for Electrochemical Energy Storage. *J. Mater. Res.* **2017**, 32, 2–15.

(259.) Mitchell, J. B.; Lo, W. C.; Genc, A.; Lebeau, J.; Augustyn, V. Transition from Battery to

Pseudocapacitor Behavior via Structural Water in Tungsten Oxide. *Chem. Mater.* **2017**, 29, 3928–3937.

(260.) Lee, S. H.; Park, C.; Park, J. W.; Kim, S. J.; Im, S. S.; Ahn, H. Synthesis of Conducting Polymer-Intercalated Vanadate Nanofiber Composites Using a Sonochemical Method for High Performance Pseudocapacitor Applications. *J. Power Sources* **2019**, 414, 460–469.

(261.) Tian, Y.; Song, X.; Liu, J.; Zhao, L.; Zhang, P.; Gao, L. Generation of Monolayer MoS2 with 1T Phase by Spatial-Confinement-Induced Ultrathin PPy Anchoring for High-Performance Supercapacitor. *Adv. Mater. Interfaces* **2019**, 6, 1900162.

(262.) VahidMohammadi, A.; Moncada, J.; Chen, H.; Kayali, E.; Orangi, J.; Carrero, C. A.; Beidaghi, M. Thick and Freestanding MXene/PANI Pseudocapacitive Electrodes with Ultrahigh Specific Capacitance. *J. Mater. Chem. A* **2018**, 6, 22123–22133.

(263.) Fleischmann, S.; Spencer, M. A.; Augustyn, V. Electrochemical Reactivity under Confinement Enabled by Molecularly Pillared 2D and Layered Materials. *Chem. Mater.* **2020**, 32, 3325–3334.

(264.) Mashtalir, O.; Lukatskaya, M. R.; Kolesnikov, A. I.; Raymundo-Piñero, E.; Naguib, M.; Barsoum, M. W.; Gogotsi, Y. The Effect of Hydrazine Intercalation on the Structure and Capacitance of 2D Titanium Carbide (MXene). *Nanoscale* **2016**, 8, 9128–9133.

(265.) Zhao, Y.; Han, C.; Yang, J.; Su, J.; Xu, X.; Li, S.; Xu, L.; Fang, R.; Jiang, H.; Zou, X.; Song, B.; Mai, L.; Zhang, Q. Stable Alkali Metal Ion Intercalation Compounds as Optimized Metal Oxide Nanowire Cathodes for Lithium Batteries. *Nano Lett.* **2015**, 15, 2180–2185.

(266.) Mitchell, J. B.; Geise, N. R.; Paterson, A. R.; Osti, N. C.; Sun, Y.; Fleischmann, S.; Zhang, R.; Madsen, L. A.; Toney, M. F.; Jiang, D. E.; Kolesnikov, A. I.; Mamontov, E.; Augustyn, V.

Confined Interlayer Water Promotes Structural Stability for High-Rate Electrochemical Proton Intercalation in Tungsten Oxide Hydrates. *ACS Energy Lett.* **2019**, 4, 2805–2812.

(267.) Wang, R.; Mitchell, J. B.; Gao, Q.; Tsai, W. Y.; Boyd, S.; Pharr, M.; Balke, N.; Augustyn, V. Operando Atomic Force Microscopy Reveals Mechanics of Structural Water Driven Battery-to-Pseudocapacitor Transition. *ACS Nano* **2018**, 12, 6032–6039.

(268.) Perez, A. J.; Beer, R.; Lin, Z.; Salager, E.; Taberna, P. L.; Abakumov, A. M.; Simon, P.; Tarascon, J. M. Proton Ion Exchange Reaction in Li3IrO4: A Way to New H3+xIrO4 Phases Electrochemically Active in Both Aqueous and Nonaqueous Electrolytes. *Adv. Energy Mater.* **2018**, 8, 1702855.

(269.) Lemaire, P.; Sel, O.; Alves Dalla Corte, D.; Iadecola, A.; Perrot, H.; Tarascon, J. M. Elucidating the Origin of the Electrochemical Capacity in a Proton-Based Battery HxIrO4 via Advanced Electrogravimetry. *ACS Appl. Mater. Interfaces* **2020**, 12, 4510–4519.

(270.) Lee, J.; Badie, S.; Srimuk, P.; Ridder, A.; Shim, H.; Choudhury, S.; Nah, Y. C.; Presser, V. Electrodeposition of Hydrated Vanadium Pentoxide on Nanoporous Carbon Cloth for Hybrid Energy Storage. *Sustain. Energy Fuels* **2018**, 2, 577–588.

(271.) Wei, Q.; Jiang, Z.; Tan, S.; Li, Q.; Huang, L.; Yan, M.; Zhou, L.; An, Q.; Mai, L. Lattice Breathing Inhibited Layered Vanadium Oxide Ultrathin Nanobelts for Enhanced Sodium Storage. *ACS Appl. Mater. Interfaces* **2015**, 7, 18211–18217.

(272.) Zhou, Y. N.; Ma, J.; Hu, E.; Yu, X.; Gu, L.; Nam, K. W.; Chen, L.; Wang, Z.; Yang, X. Q. Tuning Charge-Discharge Induced Unit Cell Breathing in Layer-Structured Cathode Materials for Lithium-Ion Batteries. *Nat. Commun.* **2014**, 5, 5381.

(273.) Yang, J.; Xiao, X.; Gong, W.; Zhao, L.; Li, G.; Jiang, K.; Ma, R.; Rummeli, M. H.; Li, F.; Sasaki,

T.; Geng, F. Size-Independent Fast Ion Intercalation in Two-Dimensional Titania Nanosheets for Alkali-Metal-Ion Batteries. *Angew. Chemie - Int. Ed.* **2019**, 58, 8740–8745.

(274.) Lu, K.; Hu, Z.; Xiang, Z.; Ma, J.; Song, B.; Zhang, J.; Ma, H. Cation Intercalation in Manganese Oxide Nanosheets: Effects on Lithium and Sodium Storage. *Angew. Chemie - Int. Ed.* **2016**, 55, 10448–10452.

(275.) Ma, N.; Kosasang, S.; Krittayavathananon, A.; Phattharasupakun, N.; Sethuraman, S.; Sawangphruk, M. Effect of Intercalated Alkali Ions in Layered Manganese Oxide Nanosheets as Neutral Electrochemical Capacitors. *Chem. Commun.* **2019**, 55, 1213–1216.

(276.) Dong, J.; Jiang, Y.; Wei, Q.; Tan, S.; Xu, Y.; Zhang, G.; Liao, X.; Yang, W.; Li, Q.; An, Q.; Mai, L. Strongly Coupled Pyridine-V2O5·nH2O Nanowires with Intercalation Pseudocapacitance and Stabilized Layer for High Energy Sodium Ion Capacitors. *Small* **2019**, 15, 1900379.

(277.) Wang, R.; Chung, C. C.; Liu, Y.; Jones, J. L.; Augustyn, V. Electrochemical Intercalation of Mg2+ into Anhydrous and Hydrated Crystalline Tungsten Oxides. *Langmuir* **2017**, 33, 9314–9323.

(278.) Chmiola, J.; Largeot, C.; Taberna, P.-L. L.; Simon, P.; Gogotsi, Y. Desolvation of Ions in Subnanometer Pores and Its Effect on Capacitance and Double-Layer Theory. *Angew. Chemie - Int. Ed.* **2008**, 47, 3392–3395.

(279.) Futamura, R.; Iiyama, T.; Takasaki, Y.; Gogotsi, Y.; Biggs, M. J.; Salanne, M.; Ségalini, J.; Simon, P.; Kaneko, K. Partial Breaking of the Coulombic Ordering of Ionic Liquids Confined in Carbon Nanopores. *Nat. Mater.* **2017**, 16, 1225–1232.

(280.) Santos, M. C.; Terezo, A. J.; Fernandes, V. C.; Pereira, E. C.; Bulhões, L. O. S. An EQCM Investigation of Charging RuO2 Thin Films Prepared by the Polymeric Precursor Method. *J. Solid State Electrochem.* **2005**, 9, 91–95.

(281.) Arias, C. R.; Debiemme-Chouvy, C.; Gabrielli, C.; Laberty-Robert, C.; Pailleret, A.; Perrot, H.; Sel, O. New Insights into Pseudocapacitive Charge-Storage Mechanisms in Li-Birnessite Type MnO2 Monitored by Fast Quartz Crystal Microbalance Methods. *J. Phys. Chem. C* **2014**, 118, 26551–26559.

(282.) Zhang, Q.; Levi, M. D.; Dou, Q.; Lu, Y.; Chai, Y.; Lei, S.; Ji, H.; Liu, B.; Bu, X.; Ma, P.; Yan, X. The Charge Storage Mechanisms of 2D Cation-Intercalated Manganese Oxide in Different Electrolytes. *Adv. Energy Mater.* **2019**, 9, 1802707.

(283.) Goubard-Bretesché, N.; Crosnier, O.; Douard, C.; Iadecola, A.; Retoux, R.; Payen, C.; Doublet, M.; Kisu, K.; Iwama, E.; Naoi, K.; Favier, F.; Brousse, T. Unveiling Pseudocapacitive Charge Storage Behavior in FeWO4 Electrode Material by Operando X-Ray Absorption Spectroscopy. *ChemRxiv* **2019**, DOI: 10.26434/chemrxiv.11340026.v1.

(284.) Evans, R. C.; Nilsson, Z.; Balch, B.; Wang, L.; Neilson, J. R.; Weinberger, C. R.; Sambur, J. B. Quantifying Capacitive-Like and Battery-Like Charge Storage Contributions Using Single-Nanoparticle Electro-Optical Imaging. *ChemElectroChem* **2020**, 7, 753–760.

(285.) Widmaier, M.; Jäckel, N.; Zeiger, M.; Abuzarli, M.; Engel, C.; Bommer, L.; Presser, V. Influence of Carbon Distribution on the Electrochemical Performance and Stability of Lithium Titanate Based Energy Storage Devices. *Electrochim. Acta* **2017**, 247, 1006–1018.

(286.) Chen, Z.; Augustyn, V.; Wen, J.; Zhang, Y.; Shen, M.; Dunn, B.; Lu, Y. High-Performance Supercapacitors Based on Intertwined CNT/V2O5 Nanowire Nanocomposites. *Adv. Mater.*

2011, 23, 791–795.

(287.) Dörr, T. S.; Fleischmann, S.; Zeiger, M.; Grobelsek, I.; de Oliveira, P. W.; Presser, V. Ordered Mesoporous Titania/Carbon Hybrid Monoliths for Lithium-Ion Battery Anodes with High Areal and Volumetric Capacity. *Chem. - A Eur. J.* **2018**, 24, 6358–6363.

(288.) Fleischmann, S.; Dörr, T. S.; Frank, A.; Hieke, S. W.; Doblas-Jimenez, D.; Scheu, C.; de Oliveira, P. W.; Kraus, T.; Presser, V. Gyroidal Niobium Sulfide/Carbon Hybrid Monoliths for Electrochemical Energy Storage. *Batter. Supercaps* **2019**, 2, 668–672.

(289.) Suss, M. E.; Presser, V. Water Desalination with Energy Storage Electrode Materials. *Joule* **2018**, 2, 10–15.

(290.) Srimuk, P.; Su, X.; Yoon, J.; Aurbach, D.; Presser, V. Charge-Transfer Materials for Electrochemical Water Desalination, Ion Separation and the Recovery of Elements. *Nat. Rev. Mater.* **2020**, DOI: 10.1038/s41578-020-0193-1.

(291.) Liu, L.; Su, L.; Lu, Y.; Zhang, Q.; Zhang, L.; Lei, S.; Shi, S.; Levi, M. D.; Yan, X. The Origin of Electrochemical Actuation of MnO2/Ni Bilayer Film Derived by Redox Pseudocapacitive Process. *Adv. Funct. Mater.* **2019**, 29, 1806778.

(292.) Pang, D.; Alhabeb, M.; Mu, X.; Dall'Agnese, Y.; Gogotsi, Y.; Gao, Y. Electrochemical Actuators Based on Two-Dimensional Ti3C2Tx (MXene). *Nano Lett.* **2019**, 19, 7443–7448.

(293.) Zhu, X.; Li, D.; Liang, X.; Lu, W. D. Ionic Modulation and Ionic Coupling Effects in MoS2 Devices for Neuromorphic Computing. *Nat. Mater.* **2019**, 18, 141–148.

Author Biographies

Simon Fleischmann is a Postdoctoral Research Scholar in the Department of Materials Science and Engineering at North Carolina State University, working in the laboratory of Prof. Veronica Augustyn. His current research is focused on understanding the impact of confined interlayer molecules in 2D materials on the electrochemical mechanisms for energy storage and conversion. In 2018, he received his Ph.D. in Materials Science from Saarland University, Germany, under the supervision of Prof. Volker Presser, focusing on ALD synthesis of carbon / metal oxide hybrid materials for electrochemical energy storage applications.

James B. Mitchell is a Ph.D. candidate in the Department of Materials Science and Engineering at North Carolina State University. He received a B.S. in Chemistry at The University of North Carolina at Charlotte where his research focused on enhancing ion-accessible surface areas in electrochemical capacitors. His dissertation research, under direction of Prof. Veronica Augustyn, focuses on understanding the materials design strategies that lead to high power densities in Faradaic transition metal oxides using a model materials system, the tungsten oxide hydrates. He is also a Department of Energy Office of Science Graduate Student Research Fellow.

Ruocun (John) Wang is a fifth-year Ph.D. student in the Materials Science and Engineering program at North Carolina State University, working with Prof. Veronica Augustyn. He received his B.Sc. degree in materials science and engineering from Purdue University in 2015. His current research interests include the design, synthesis, and characterization of transition metal oxide hydrates and the mechanics of electrochemical intercalation from *operando* experiments.

Cheng Zhan is a postdoctoral researcher in the Quantum Simulation Group at Lawrence Livermore National Laboratory. He obtained his BSc degree from the University of Science and Technology of China (USTC) in 2013 and PhD degree from the University of California, Riverside (UCR) in 2018. His research focuses on understanding the electrochemical interface, energy storage, ion transport, and separation from computational chemistry. He received the UCR Dissertation Year Fellowship in 2017 and the Chinese Government Award for Outstanding Student Studying Abroad in 2018.

De-en Jiang is a tenured Associate Professor in the Department of Chemistry, University of California, Riverside (UCR) and a cooperating faculty member in the Materials Science & Engineering Program and Department of Chemical & Environmental Engineering at UCR. His research focuses on applying state-of-the-art computational methods to important chemical systems and energy-relevant problems. He received the U.S. Department of Energy Early Career Award in 2009 and the Presidential Early Career Awards for Scientists and Engineers (PECASE) in 2010. He was named a Kavli Fellow by the National Academy of Sciences in 2012.

Volker Presser is a tenured Full Professor (W3) at Saarland University working at the INM – Leibniz Institute for New Materials in Saarbrücken, Germany. As Chair of Energy Materials, his team explores electrochemical materials and processes for energy storage, water remediation, energy harvesting, and ion separation. His work has received serval awards and recognitions, such as the Bayer Early Career Award (2013), the Heinz Maier Leibnitz Prize (Germany Research Foundation, 2013), and the Award for Research Cooperation and High Excellence in Science (Minerva Foundation, 2017). He became a Fellow of the Royal Society of Chemistry in 2020.

Veronica Augustyn is an Assistant Professor of Materials Science and Engineering and a University Faculty Scholar at North Carolina State University. Her research focuses on the behavior of materials at electrochemical interfaces, including capacitive energy storage mechanisms, effects of confinement on electrochemical reactivity, synthesis of layered materials with confined solvents, and electrode architectures. Her group's research has been honored with a 2019 U.S. Department of Energy Early Career Award, a 2019 Sloan Research Fellowship in Chemistry, and a 2017 NSF CAREER Award. She is also a Scialog Fellow in Advanced Energy Storage from the Research Corporation for Science Advancement.

Table of Contents Graphic